Scour around Complex Shape Bridge Piers in a River

Hayder Qais Majeed

Submitted in accordance with the requirements for the degree of

Doctor of Philosophy

The University of Leeds

School of Civil Engineering

November 2017

Intellectual Property and Publication Statements

The candidate confirms that the work submitted is his own, except where work which has formed part of jointly-authored publications has been included. The contribution of the candidate and the other authors work has been explicitly indicated herein. The candidate confirms that appropriate credit has been given within the thesis where reference has been made to the work of others.

The work presented in Chapter 4 of this thesis has appeared in the following publication:

H. Majeed, N. Wright and A. Sleigh. Large Eddy Simulations and Analyses for Bridge Scour Development. Proceedings of the 36th IAHR World Congress, 2015.

I was responsible for the model simulation and data analyses. The candidate wrote the manuscript with guidance from the co-authors.

Acknowledgements

First and foremost, I would like to thank my supervisors Prof Nigel Wright, Dr Andrew Sleigh and Dr Duncan Borman. Their continual support and overall input has not gone unnoticed and without them this endeavour would not have been possible.

I also wish to express my greatest thanks to the ministry of Higher Education and Scientific Research in Iraq, Iraqi Cultural Attaché in London and the University of Baghdad for the funding that made this all possible.

I wish to say a huge thank you to my family. I owe possibly the biggest thank you to my parents, for my dad who always encourage me and ask me about my study, and for my Mum who always pray to me, and my wonderful wife that always supports me. I also want to give a big kiss to my lovely kids (Yousif, Tanya, Qais and Ali).

I would like to thank my family, who were always supporting me and sending love from Iraq. Specially my brothers, my sisters for their unconditional love and warm words and feelings.

Finally ,there are so many friends that I would like to thank. I will not forget the conversations and encouragement that I received from all of them, and the ideas and significant moments we shared during all this time. They will always be in my heart.

Abstract

The research undertaken develops a numerical modelling approach to investigate the interaction between the turbulent coherent structures and the sediment transport that occur around bridge piers. The study is directly relevant to understanding of erosion mechanisms around both circular and non-circular bridge piers constructed in a river bend.

In this research the Large Eddy Simulation (LES) approach is adopted, alongside a dynamic meshing technique to enable the simulation of scouring around the bridge pier. This methodology allows an approach that numerically describes a complex three dimensional (3D) scour behaviour around bridge piers through coupling the changes in topography with the local detailed hydrodynamics. By using of a commercial 'Computational Fluid Dynamics' (CFD) code and User-Defined Function (UDF) written in C^{++}, the bed shear stress can be computed from the LES predictions model at each time step and stored in order to calculate scour. The dynamic mesh updating technique is implemented to move the bed and assures a practical and accurate scour simulation by individually updating the domain's riverbed at each time step.

Simulation, in accordance with the experimental configuration of Dargahi (1989) for the turbulent channel flow past a circular cylinder, mounted in a flatbed, has been undertaken using the LES approach. The predicted results are compared with those obtained from URANS models (i.e., k-ε standard and k-ω SST), and with the experimental data, in order to verify the reliability and feasibility of the LES.

The coupling between LES and the dynamic mesh technique has been undertaken to study the coherent structures around a circular bridge pier in the initial stage of scour evolution. The approach produces a good prediction of the qualitative and quantitative characteristics observed by Dargahi (1990). Furthermore by studying the transient behaviour for the horseshoe vortex system upstream of the cylinder, during the scour process evolution using LES shows that the main vortex has the bimodal oscillation phenomenon, which increases the ability of these vortices to remove the sediment around the cylinder.

The current investigation consider the most relevant range of angles of attack $(\alpha = 0^{\circ} \text{to } 60^{\circ})$ in design of the oblong pier that is one of the most common shapes of the piers. Predicted results demonstrates a very significant effect of the angle of attack on the complexity of the flow, and thus on the scour pattern and the maximum scour depth around the bridge pier. Finally a modified equation is proposed to compute the angle of attack correction factor in case of oblong bridge piers. This equation adopts previous work to take into account the results from LES predictions that have been shown to more reliably predict the complex flow behaviour important in determining scour rates. The hypothesis suggested in this study was based on LES, for calculating the angle of attack correction factor for oblong bridge with aspect ratio $L/b = 3.0$. It's more accurate than the previous equation, which is depended on the URANS model, but to make this hypothesis more general and applicable in the engineering application its need to be tested against a range of L/b.

Table of Contents

List of Figures

List of Tables

Chapter 1

Introduction

1.1 Background

Bridge scour has been identified as one of the main causes of bridge failure worldwide. The loss of soil around a bridge pier may leave the bridge with inadequate support and consequently a complete failure of the bridge may occur. Statistical data published by the Structures Division of the New York State Department of Transportation (DOT) and computed using the National Bridge Failure Database show that, of the 1,502 recorded bridge failures for the period from 1966 to 2005, 58% of failures were due to scour (Hunt, 2009). This means in the USA alone, on average, there have been 22 bridge failures every year as a result of scour.

These numbers give worrying indications about the potential loss of life, the direct costs involved in repairing and replacing the structures and the indirect costs resulting from disruption to the transportation network. According to the California DOT (2011) “Bridge Square Foot Cost" summary, the average cost of a bridge in 2011 was $1,867per m^2 of bridge deck (Briaud et al., 2013).

Clearly, bridge scour is a significant problem for bridge safety and has received global attention. For decades, research has been conducted to

advance the design, countermeasures, evaluation and inspection of bridge scour. The importance and complexity of this topic and problem is the motivation of the undertaken research.

1.2 Bridge scour basics

Bridge scour can be defined as the process of the removal of sediment particles (sand and rocks) from around bridge piers or abutments. Scour usually happens when the shear stress produced by the approaching flow exceeds the limiting value that the soil particles can withstand.

1.2.1 Types of bridge scour

The types of scour that can occur at the bridge crossings typically include long term degradation, contraction scour, and local scour. These terms are defined below; at a particular bridge crossing section, any or all of the different types of scour can occur simultaneously and interactively, as illustrated in Figure 1.1. Long-term degradation is the lowering of the stream-bed caused by erosion along the channel profile. Degradation includes the scouring of the stream-bed resulting from the sediment supply deposited from upstream being less than what is eroded and transferred away (Richardson and Davis, 2001). Contraction scour involves the removal of sediment from the bed and banks across all or most of the river width. This component of scour happens when the water accelerates as it flows through an opening that is narrower than the river width upstream from the bridge.

Local scour is the erosion of the sediments which are found near the bridge pier or abutments due to the formation of turbulence structures (i.e., the horseshoe vortex which forms in front of the pier and extend in both lateral directions, and the wake vortices that is located downstream of the bridge pier). These turbulent structures have significant impact on the bed shear stress, and subsequently the erosion of sediment around the bridge pier (Richardson and Davis, 2001).

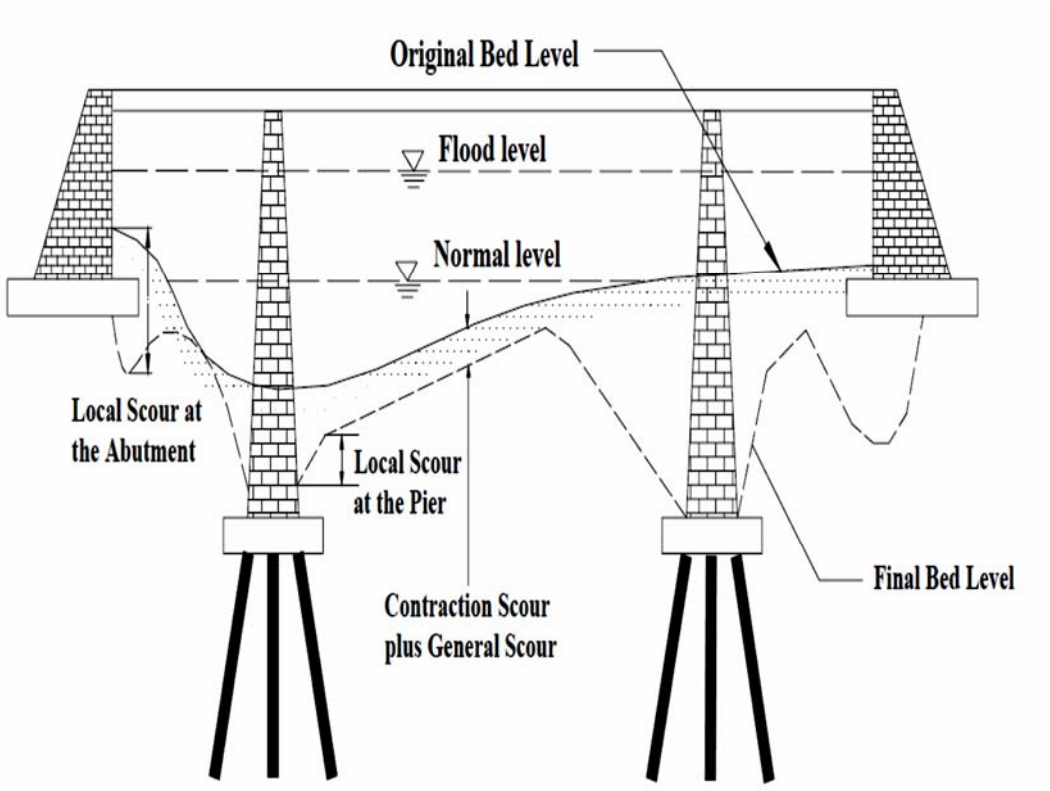

Figure 1.1: Different types of scour in a typical bridge cross section (Wang, 2004).

1.2.2 Typical turbulent structures around a bridge pier

A representation of the flow pattern around a circular cylindrical bridge pier is shown in Figure 1.2 (Graf and Istiarto, 2002). Flow approaches the upstream side of the pier and forms into down-flow (i.e. travelling vertically downwards) at the front face of the pier in the vertical plane, with a horseshoe vortex system

created around the base. This horseshoe vortex system is the flow feature that is the major cause of the local scour around a pier. A bow wave appears close to the free surface upstream of the pier, and wake vortices are present downstream of the pier that extend throughout the flow depth.

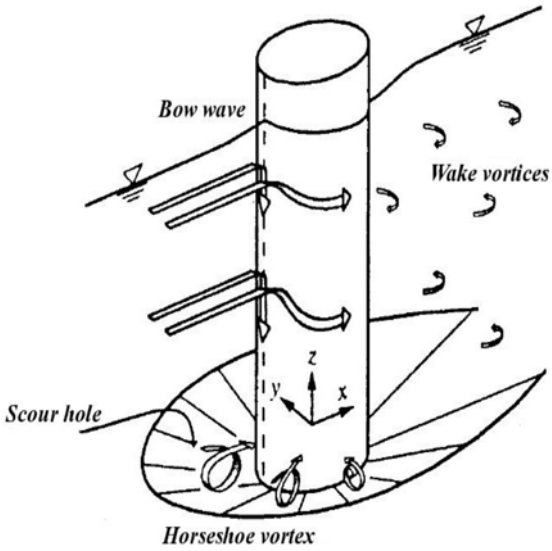

Figure 1.2: Schematic of flow structures and local scour hole around a cylindrical pier (Graf and Istiarto, 2002).

1.2.3 Erosion and transport of bed-load sediment

1.2.3.1 Forces acting on the sediment particle

The most basic approach for considering the initiation of sediment motion depends on the balance between the forces exerted on the sediment particle as shown in Figure 1.3. The sediment particles are subjected to the drag force due to fluid flow, lift force due to the vertical groundwater flow, and the submerged particle weight. When the moments due to the driving forces are larger than the moments resulting from the gravity force, the particle will move around the pivot point of contact (Van Rijn, 2016).

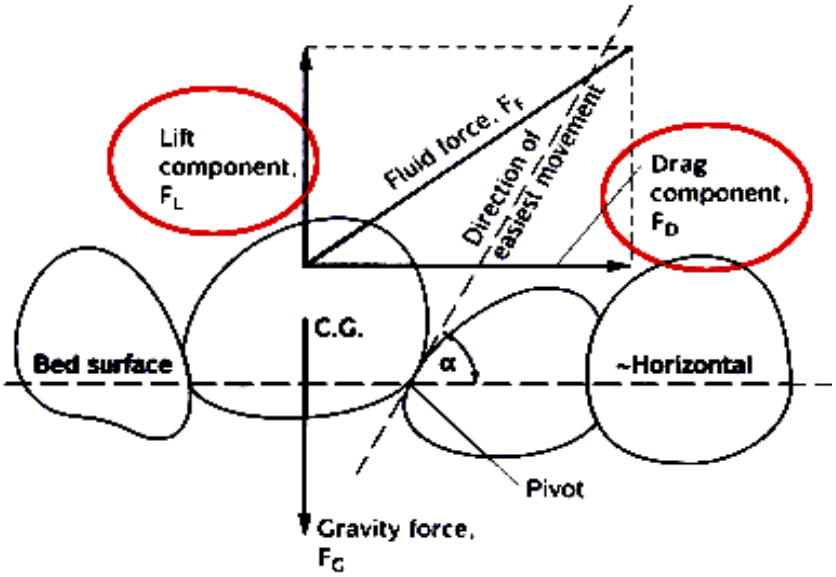

Figure 1.3: A schematic illustration of the forces exerted on a sediment particle in flow (Geol.umd.edu, 2017.).

1.2.3.2 Initiation of erosion

There are a number of widely used bed load sediment-transport models available. Many of these models are based on the concept that sediment transport can be related to the non-dimensional bed-shear stress or the critical Shields parameter such as: Meyer-Peter and Müller (1948), Engelund and Fredsøe (1976), Parker (1990), Wilcock and Crowe (2003). The critical Shields parameter at the incipient of motion:

$$\theta_{cr} = \frac{\tau_{b.cr}}{(\rho_s - \rho) g d_{50}} \qquad 1.1$$

The concept of this equation is based on the pioneering experimental work of Shields (1936), which showed that θ_{cr} varies with the boundary Reynolds number ($R_e^* = u_* d_{50}/\vartheta$) of the particles through a curve which is referred to as the 'Shields curve' as shown in Figure 1.4.

Where $\tau_{b.cr}$ is critical bed shear stress; ρ_s is sediment particle density; ρ is fluid density; g is gravity; and d_{50} is median grain size, ϑ is kinematic viscosity; and u_* is friction velocity.

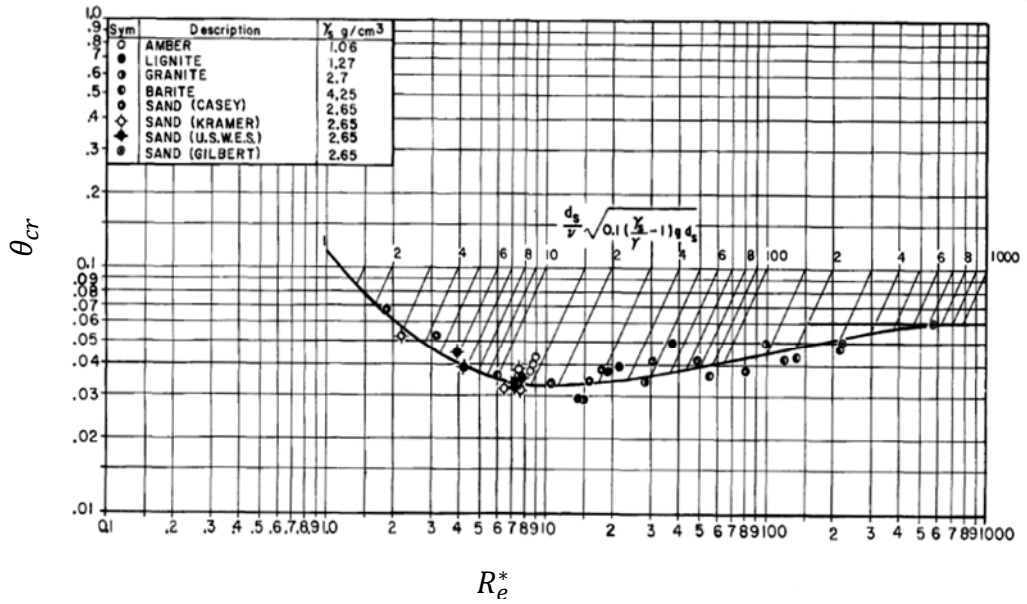

Figure 1.4: Shields' curve as function of boundary Reynold number (Shields, 1936).

1.2.3.3 Sediment transport modes

As mentioned, many computational sediment transport models have been developed. In general, these models can be categorised into three different types: bed load, suspend load and dissolved load – the location of these within the flow body is shown in Figure 1.5.

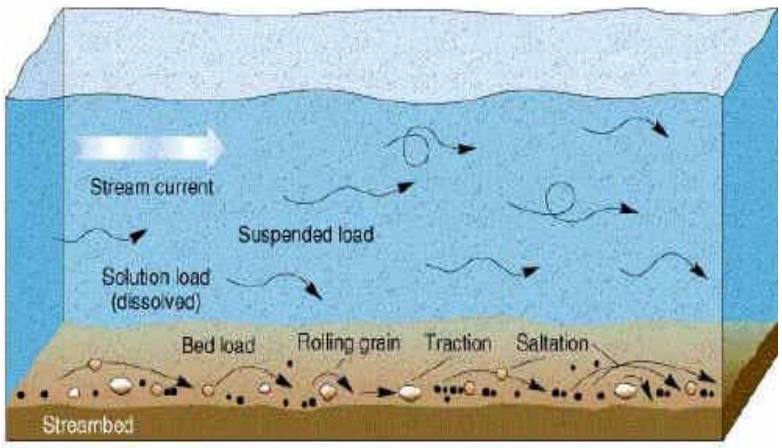

Figure 1.5: Three types of sediment transported in the stream (Geography.unt.edu, 2017).

Bed load is the sediment movement close the riverbed; the movement of such sediment usually includes rolling, traction and saltation. Bed loads move by the shear stress acting at the boundary.

Suspended load is the part of the sediment that is carried by the fluid flow, and it moves when the excess shear stress is large enough. The sediment may be suspended due to the upward flow direction of turbulence created at the bed of the river.

Dissolved load is a material that is chemically carried in the water. In general, it is not sediment, but it may constitute a significant part of materials transported with stream (Hickin, 1995).

To determine the local scour around a bridge pier, the bed load and suspended load is required to be calculated. In the region close to the pier many turbulent structures are known to develop which will significantly interact with the sediment particles. The complex turbulent structures make the prediction of bed level change very challenging.

In literatures, many formulas for equilibrium bed-load transport can be found. Most of them relates to bed load transport rate to bed shear stress. The well-referenced formula of Van Rijn (1986) is used to calculate bed-load flux in this study. It allows particle saltation under the influence of hydrodynamic and gravity forces. Its' development is based on extensive experiments conducted with sediment of 200–2000μm particle diameters, a flow depth larger than 0.1m and Froude numbers less than 0.9, which fit the conditions considered in this study.

1.2.4 Scour hole development

A scour hole is area where removal of riverbed material which surrounds the bridge foundation structures has taken place. The scour depth provides a good indication to the seriousness of the scour. There are many examples of scour causing bridge collapse; one of these is Schoharie Creek Bridge which, in 1987 collapsed without warning due to severe scour in a flood. Figure 1.6 shows an aerial view of the bridge a few hours after collapse (Swenson and Ingraffea, 1991).

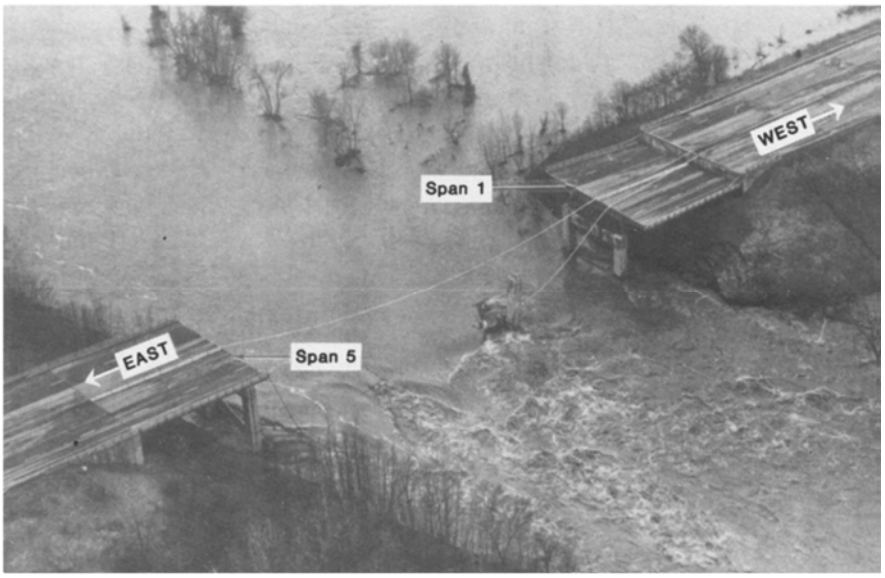

Figure 1.6: Aerial view of Schoharie Creek Bridge after failure (Swenson and Ingraffea, 1991).

There are many factors affecting the scour depth around bridge piers and abutments such as: velocity and depth of the approaching flow; shape of the pier; angle of attack of the approaching flow to a pier or abutment; bed material properties. Within a scour hole the shear stresses on the sediment starts to reduce as the hole gets deeper and larger until at equilibrium condition when the shear stress is lower than the critical shear stress of the particles further scour stops.

Various scour prediction equations have been proposed based on laboratory experiments (Laursen and Toch, 1956, Shen et al., 1969, Breusers et al., 1977, Briaud et al., 1999, Melville and Chiew, 1999, Sheppard et al., 2004, Debnath and Chaudhuri, 2012). These equations predict the maximum scour depth by considering the structure, sediment and flow conditions. They can be written in a dimensionless form as shown in Equation 1.2.

$$\frac{d_s}{b} = f(k_s, k_{\alpha,} \frac{y_1}{b}, \frac{V_1}{\sqrt{g y_1}}, \frac{\rho V_1 b}{\mu}, \frac{V_1}{V_c}, \frac{b}{d_{50}}, \sigma_g) \quad 1.2$$

Where d_s is the equilibrium scour depth; b is the width of the bridge pier; k_s, $k_{\alpha,}$ is the shape factor and alignment factor respectively; y_1 and V_1 are approach depth and velocity respectively; V_c is the critical velocity for initiation of sediment motion in the approach flow; σ_g is the geometric standard deviation of sediment size distribution; μ and ρ are the dynamic viscosity and density of the fluid. In this study the effect of pier shape factor k_s, and the alignment factor $k_{\alpha,}$ will be taken into consideration in computing the scour depth around bridge piers.

1.3 Research gap

Despite the progression of research in the field of scour and turbulent flow around bridge piers, the vast majority of the studies examine a flow field around a circular bridge pier, such as in the experimental studies: Melville and Raudkivi (1977), Dargahi (1989), Dargahi (1990), Ahmed and Rajaratnam (1998), Sarker (1998), Graf and Istiarto (2002), Akilli et al. (2004), Roulund et al. (2005), Ettema et al. (2006), Unger and Hager (2007), Das et al. (2013), Keshavarzi et al. (2014), Aksoy et al. (2017). In addition, there are many numerical investigations that deals with scour around circular cylinders using

mean flow approaches such as Richardson and Panchang (1998), Olsen and Kjellesvig (1998), Ali and Karim (2002), Salaheldin et al. (2004), Roulund et al. (2005), Adhikary et al. (2009), Huang et al. (2009), Zhao et al. (2010), Baranya et al. (2014), and eddy resolving techniques: Choi and Yang (2002), Paik et al. (2004), Kirkil et al. (2005), Wei and Huhe (2006), Kirkil et al. (2008), Palau-Salvador et al. (2008), Kirkil et al. (2009), Pasiok and Stilger-Szydło (2010), Escauriaza and Sotiropoulos (2011), Apsildis (2012), Shao et al. (2013), Kim et al. (2014). Therefore, knowledge of the mechanism of bridge pier scour for complex shapes conducted in a straight river or located on a river bend is still poor. This is because there are likely to be complex interactions between structures, flow and sediment when conditions change from the simple circular cylinder with normal flow. It is important to consider non-circular cylindrical piers, as they are common and also bridges are rarely constructed in straight stretches of river resulting in more complex flow than that observed in the case of straight channels.

Computational fluid dynamics (CFD) methods are utilised increasingly as a tools for tackling hydraulic and environmental engineering problems (Rodi et al., 2013). Due to computational limitations in the past, the Reynolds-averaged Navier-Stokes (RANS) models were predominantly used to account for the mean flow quantities only, with all the scales of the turbulence being modelled. With computer power continuing to expand enormously, it is permitting researchers to tackle more complex problems. This has uncovered the impediment of RANS models, particularly in cases where large scale turbulent structures are dominant within the flow. The expansion in computer power has likewise prompted the advancement of more powerful but computationally more

intensive simulation methods for turbulent flows, moving far from absolutely statistical treatment to eddy resolving techniques. These can more readily assess the material science of the complex turbulent movement and permit additional study to comprehend the mechanisms involved. Direct Numerical Simulation (DNS) is still not a realistic option for practical application at high Reynolds number (R_e) flows, so the improvement has focused essentially on Large Eddy Simulations (LES) in which, as the name suggests, just the large scale turbulent structures are resolved while the impact of the small scale is modelled. In the past two decades, computational research has moved from RANS to LES strategies for simulations that require a very detailed turbulent flow structures to be resolved.

The aim of this study, is to use CFD with the incorporation of eddy resolving techniques (using LES), to accurately simulate and identify the detail of the flow structures that cause scour: in particular the horseshoe and wake vortices over the entire three-dimensional flow field around bridge piers during the initial stage of the scour process. Results will be compared with other Reynolds-averaged Navier–Stokes (RANS) methods, and also with experimental data obtained from two dimensional (2D) Particle Image Velocimetry (PIV) and other similar experimental techniques. This thesis details the time evolving scour processes around circular and non-circular pier shape subjected to flow in a range of directions.

1.4 Objectives and outline of the thesis

Further investigation is necessary to reduce the uncertainty in quantification of the scour process around bridge piers in a river. The aim of this study is to accurately simulate flow and scour around bridge piers in order to improve their

design against scour. The understanding of bridge scour developed in this research will include more of the fundamental physics rather than empirical formulae which are often formed on regression relations of laboratory and/or field scour data. Therefore, there is lots of empiricism transferred in these equations through adjustment or correction factors. These empirical formulae do not clarify the physics of the scour phenomenon nor the exact way through which every factor is affecting the scour mechanism (Hafez, 2016).

The work undertaken here will provide bridge designers with more reliable knowledge on which they may base their bridge piers designs and associated scour protection measures.

The following specific objectives must be achieved in order to attain the stated aim:

1. Study the turbulent flow structure around a circular cylindrical bridge pier mounted on fixed flat bed in a straight flow channel (angle of attack is equal to zero). An eddy resolving technique such as LES will be employed in the simulation to provide details of the turbulent structure of the flow. This simulation will involve verification and validation of LES models for turbulent flow and will be compared to published work on flow around a circular cylinder.
2. Simulate the time dependent scour of circular cylinder bridge pier located on movable bed. It will be performed using the LES technique. It will simulate the effect of down-flow, horseshoe and wake vortices on the bed shear stress with respect to increasing the scour depth. The methodology used to calculate the scour depth around the pier involves

moving an initial flatbed downward in increments proportional to the excess shear stress above critical, at a point on the bed.

3. Study the shape of the scour hole and bed shear stress with respect to scour depth around non-circular pier shape subjected to flow in a range of directions.

The following sections give an outline of the thesis, and summarises the undertaken research study:

Chapter 2, literature review is given on prior works with the relationship between the flow and sediment transport around bridge piers. States of art on the Computational Fluid Dynamics (CFD) models implemented to capture the complex unsteady flow past surface mounted obstacles are also reviewed. The methodologies that are used to simulate the scour mechanism and the sediment transport models are also evaluated.

Chapter 3, presents the results of the flow simulation past a vertical cylinder mounted on a rectangular channel reproducing the experimental configuration of Dargahi (1989). The 3D vorticity dynamics and turbulence statistics at the symmetry plane are studied.

Chapter 4, dynamic mesh modelling technique for sediment transport is developed to perform the scouring process around bridge piers for a single phase simulation.

Chapter 5, outlines parametric studies of scour process around oblong bridge pier shapes subjected to turbulent flow with different angles of attack.

Chapter 6, summarises and draws conclusions of the research and its applications, and describes future research possibilities that will emerge from the research study.

Chapter 2

Literature Review on Modelling of Bridge Scour

2.1 Introduction

Failure in bridges due to scour at their piers is a common occurrence. Therefore, the scouring process and sediment erosion around the piers is considered an important issue in hydraulic engineering. In this chapter, firstly, a review is given on previous experimental studies that consider the influence of pier parameters, such as the pier shape and the alignment of the pier to the flow direction. Secondly, the CFD models employed to capture the complex turbulent structures that interacts with the surface (riverbed) mounted obstacles is given. These CFD simulations are categorised depending on the modelling approach for the Navier-Stokes equations (such as steady Reynolds-Averaged Navier-Stokes (RANS), Unsteady Reynolds-Averaged Navier-Stokes (URANS), Detached Eddy Simulation (DES) and Large Eddy Simulation (LES)). Lastly, the mechanisms that control the scour dynamics and the sediment erosion models, utilised to simulate erosion in engineering problems is undertaken. A summary of the findings is presented at the end of this chapter.

2.2 Experimental studies of flows around bridge piers

Several experimental studies on scour around bridge piers are available in the literatures. These experimental studies have been carried out using variety of measuring techniques. Most of these, considered the case of circular

cylinders to simulate the shape of the pier such as Melville and Raudkivi (1977), Dargahi (1989), Dargahi (1990), Ahmed and Rajaratnam (1998), Sarker (1998), Graf and Istiarto (2002), Akilli et al. (2004), Roulund et al. (2005), Ettema et al. (2006), Unger and Hager (2007), Das et al. (2013), Keshavarzi et al. (2014), Aksoy et al. (2017). Some of these studies neglected the effect of the large-scale coherent structures present in the region surrounding the pier, which has led to partial understanding of the flow structures causing scour. Other studies have shown that the scour evolution and the maximum scour depth at equilibrium can be affected by the amount of vorticity in the horseshoe vortex region and in the wake region of the cylinder.

2.2.1 Coherent structures and the horseshoe vortex system

The most important experimental study by Melville and Raudkivi (1977), investigated the effect of the coherent structures and horseshoe vortex system around the bridge pier on the scour depth and pattern. They examined the scour region of a circular pier under clear water scour conditions. They summarised the results of the investigation of flow patterns, turbulence intensity distributions and boundary shear stress distribution effected in the scour hole. Furthermore, Dargahi (1989) experiment for fixed beds and Dargahi (1990) experiment for mobile beds are considered the most important in this field. They investigated the flow field around a vertical circular cylinder mounted on flat and mobile beds by using the Hydrogen Bubble Flow technique for various ranges of R_e (from 6.5×10^3 to 6.5×10^4). They found that the horseshoe vortices upstream of the cylinder had a significant effect on the main flow characteristic, and the number of vortices related with R_e, and also that for each constant R_e there are different flow patterns. These two experiments are considered the

only ones available for scour around bridge piers field that relates to the horseshoe vortex system and the scour process.

More recent experimental studies have been undertaken to investigate circular cylindrical piers in channel flows: Graf and Istiarto (2002); who presented the effect of 3D flow around a cylinder bridge pier on equilibrium scour hole by using an Acoustic-Doppler Velocity Profiler (ADVP). This technique was used to measure the three instantaneous components of the velocity in the vertical symmetry plane of the flow upstream and downstream of the cylinder. They found that a vortex-system formed at the upstream of the pier and an additional wake-vortex system of strong turbulence was created downstream of the pier. Also, Roulund et al. (2005) investigated the effect of boundary layer thickness, the R_e and the bed roughness on the horseshoe vortex around a vertical circular pier under constant flow. The experimental study was conducted by using two components of Laser-Doppler Anemometry (LDA) flow measurements. They concluded that the horseshoe vortex and the bed shear stress were significantly affected by the boundary layer thickness and R_e.

Ettema et al. (2006) examined the local scour at vertical cylinders with different diameters mounted on a sand bed using Large Scale Particle Image Velocimetry (LSPIV) measurements. These measurements were made to determine the strength and extent of the vortices downstream of the cylinder. They provided a relationship between equilibrium scour depth, cylinder diameter, and the intensity and frequency of large-scale turbulence shed from each cylinder; they also concluded that the normalised scour depth with cylinder diameter increased when the cylinder diameter decreased.

Unger and Hager (2007) used Particle Image Velocimetry (PIV) to explore the internal flow characteristics around circular bridge piers and the horseshoe inside the scour hole upstream of the cylinder. The PIV measurement was applied both in the horizontal and vertical planes, allowing for a quasi-spatial visualisation of the velocity field. They provided experimental data which may be considered suitable as a basis for comparison with advanced numerical simulation.

Das et al. (2013) investigated the circulation of the horseshoe vortex system of sixteen circular piers. In clear water scour conditions, the parameters are changed according to the inflow depth, pier R_e, and Froude numbers (F_r) which is a dimensionless number defined as the ratio of inertial and gravitational forces ($F_r = U/\sqrt{gL}$, where U is the water velocity and L is the hydraulic depth). They used Acoustic Doppler Velocimetry (ADV) to measure the turbulent flow. They concluded that the flow is always horizontally above the scour dip, but it is downward close to the pier. The magnitude of circulation was the same at the plane of symmetry. In addition, they found that the circulation was decreased with increase in the flow depth, and increased with the increase of the F_r and pier R_e.

Keshavarzi et al. (2014) investigated the structure of turbulent flow around a single circular bridge pier and its effects on the scouring process. They applied a 3D octant analysis by using micro-ADV to measure the velocity flow at 102 points near the bed of an open channel. They concluded that the mechanism of sediment movement around the cylindrical bridge pier is mainly

affected by the external sweep and internal ejection of the flow around the bridge pier.

Circular piers can be considered desirable in experimental modelling over different shapes for a number of reasons (Paice and Hey, 1993):

- The independency of the circular pier to the direction of the incoming flow; therefore, the scour depths stay constant for the same hydraulic conditions.
- Just a single setting out point is required for the circular piers.
- Circular piers are easy to build and readily available.

When considering other shapes of pier, typically they are analysed in comparison to the circular cylinder. The shape difference has been accounted for by applying appropriate correction factors. Thus, correction shape factor ,k_s, can be defined by the ratio of the maximum scour depth for non-circular pier to the maximum scour depth to the circular shape considering the same width (Richardson and Davis, 2001).

2.2.2 Pier shape effect

The effect of pier shape has been studied by many researchers. Tison (1940) showed that the depth of the scour hole at the bridge pier can be affected by the curvature of the flow around the pier. Chabert and Engeldinger (1956) experimentally tested the scour around six pier shapes (shown in Figure 2.1). Their results indicate that a round nosed pier and double pier with web have the same scour depth for similar approach flow conditions. Whereas, the maximum scour depth for lenticular piers was between 0.33-0.86 at circular pier

for the same corresponding flow velocities (with greater scour depths ratios for greater corresponding flow velocities). An ogival pier reached a scour depth that varied between 0.5-1.0 at circular pier for the same corresponding flow velocities (with greater scour depths ratios for greater corresponding flow velocities).

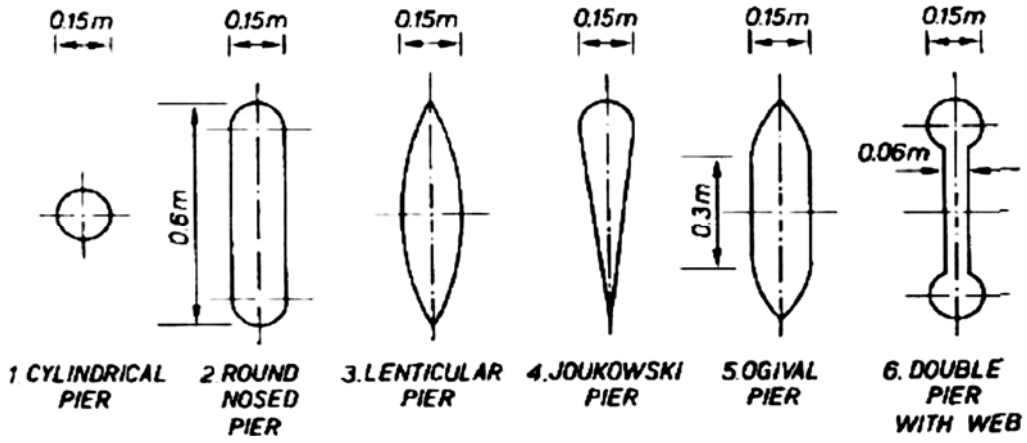

Figure 2.1: Six pier shapes tested against scour depth by Chabert and Engeldinger (1956).

Shen et al. (1969) classified pier shapes into blunt-nosed piers and sharp-nosed piers. In the blunt-nosed pier case, a strong horseshoe vortex system exists and thus the maximum scour depth happens at the pier nose. In sharp-nosed pier case the horseshoe vortex system is very weak, and the maximum scour depth happens near to the downstream side of the pier.

Breusers et al. (1977) concluded that the advantage from the reduction in the scour depth for streamlines shapes (i.e., rounded nose shape) compared with the scour depth in the case of circular pier disappears when the angle of attack of the approaching flow is larger than 10° to 15°. In such cases it is recommended that the correction shape factor k_s should not be less than 1.0.

Debnath and Chaudhuri (2012) predicted the maximum scour depth around non-circular bridge piers (square, rectangular and round-nosed) under a clay-sand mixed cohesive sediment bed. They found that the correction shape factor with respect to the circular bridge pier was not constant in a cohesive sediment bed and varied over a range (i.e., the values of the pier shape factor were found to vary between 0.5–1.0, 1.0–1.8, and 1.0–1.7 for the round-nosed pier, rectangular pier and the square pier respectively).

Fael et al. (2016) studied the pier cross section effect for different pier shapes (rectangular square nosed, rectangular rounded nosed, oblong and pile group) with respect to the circular bridge pier. The value of k_s at equilibrium are shown in Figure 2.2. This figure includes ±10% error around $k_s = 1.2$ (continuous lines) and $k_s = 1.0$ (dashed lines). They concluded that the oblong and round nosed cross section piers behave as circular pier and k_s is identified equal to 1.0 with 10% error band. For rectangular and pile group piers the $k_s = 1.2$ with 10% error band.

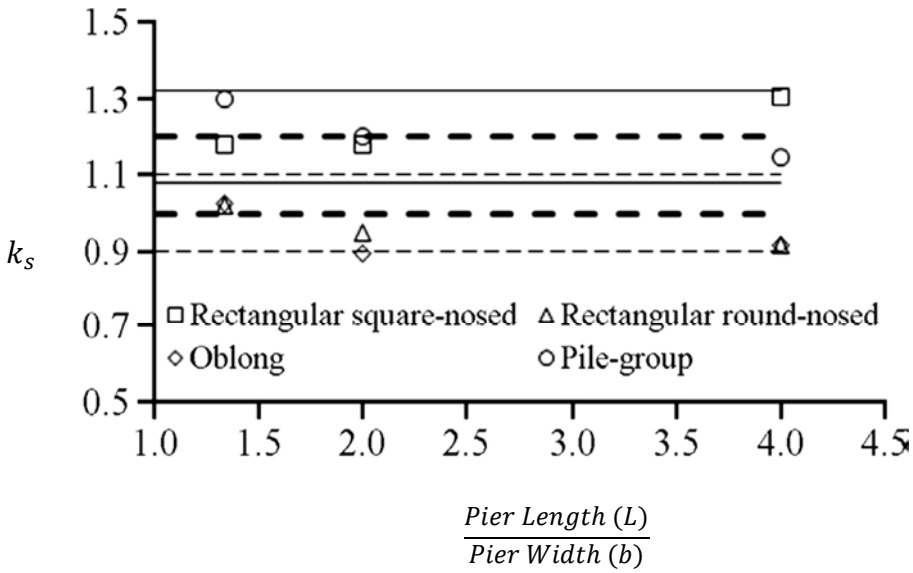

Figure 2.2: Shape factor at the equilibrium, k_s. (Fael et al., 2016).

2.2.3 Pier alignment to the flow direction

For the case when the bridge pier is located in river bend, the approaching flow direction and the long direction of the bridge pier will not concur, and the angle between the two is called the angle of attack (α). In this case, the projected width is greater than the actual width and as such a greater scour depth could occur. The length of the pier divided by the pier width as a function of the angle to the flow direction forms the effective pier width (Figure 2.3).

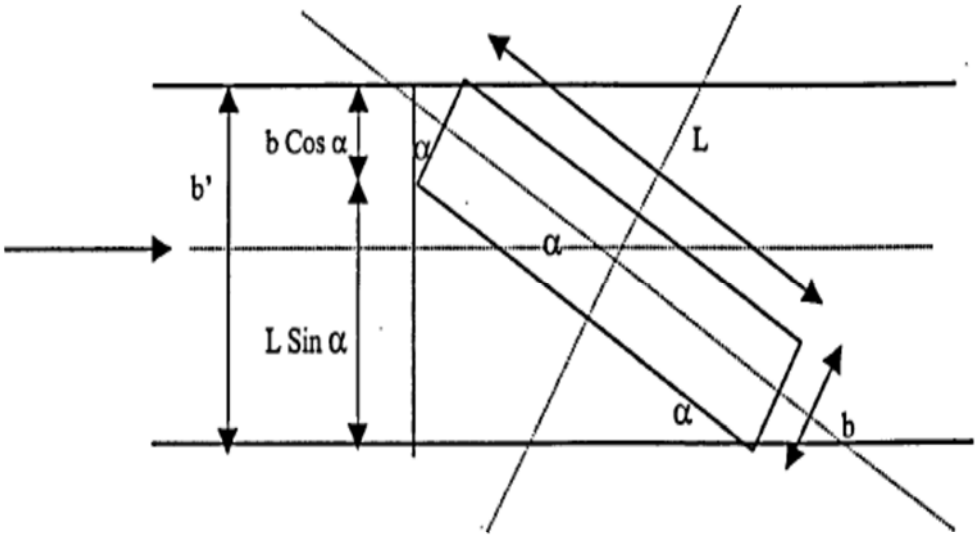

Figure 2.3: Effective pier width (*b'*) as a function of the pier length (*L*), pier width (*b*) and angle of attack (Bennetts, 2002).

The angle of attack correction factor (K_α), which is defined by the ratio of the maximum scour depth for any α to the maximum scour depth when $\alpha = 0^\circ$, is dependent on the pier length to width ratio. The influence of the angle of attack on the maximum scour depth has been studied by a few researchers due to flow complexity around the pier, the most well-known being Laursen and Toch (1956), who proposed a family of curves to estimate the K_α, for rectangular piers at a different angles of attack $(0^\circ \leq \alpha \leq 90^\circ)$ and different aspect ratios $(2 \leq \frac{L}{b} \leq 16)$, as shown in Figure 2.4.

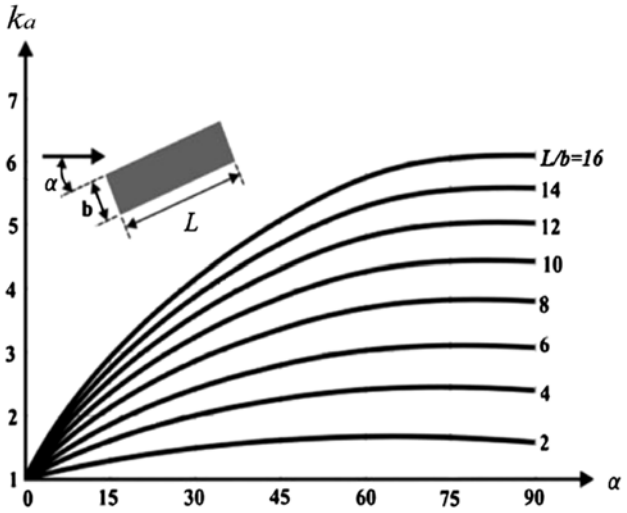

Figure 2.4: Local scour depth variation with different angles of attack (Laursen and Toch, 1956).

Richardson and Davis (2001) suggested the following expression that fits the angle of attack correction factor, K_α, obtained by Laursen and Toch (1956):

$$K_\alpha = \left(\frac{L}{b} sin\,\alpha + cos\,\alpha\right)^{0.65} \quad 2.1$$

where α is the angle of attack, *b* the pier width and L is pier length. According to Richardson and Davis (2001), K_α should only be used if the angle of attack, α, is higher than 5° and $2 \leq \frac{L}{b} \leq 16$. Melville et al. (1989) observed that the use of the Laursen and Toch (1956) chart could be less than that which may occur in the field. Melville et al. (1989) proposed that the use of the curves was dependent upon the discharge and flow depth.

Mostafa et al. (1993) noticed that the maximum scour depth, as predicted by the Laursen and Toch (1956) curves, could result in the under estimation of local scour depth at non-circular piers. They detailed that, in spite of the fact that Laursen and Toch (1956) curves are broadly utilised within the literature, their experimental basis has never been clarified sufficiently and it is unclear whether other affecting variables might be available; for example, flow depth

and sediment effects. Mostafa et al. (1993) proposed alternative methods for determining the angle of attack correction factor:

$$K_\alpha = \left(\frac{L}{b} sin\,\alpha + cos\,\alpha\right)^{0.8} \quad 2.2$$

$$K_\alpha = \left((\frac{L}{b}-1) sin\,\alpha + 1\right)^{0.9} \quad 2.3$$

Equations 2.2 and 2.3 are for rectangular piers and oblong piers respectively. All the experiments conducted by Mostafa et al. (1993) were undertaken in the clear water region.

Based on experiments by Choi et al. (1995), three equations that are dependent upon the F_r were derived. These equations are used to predict the angle of attack correction factor around non-circular piers:

$$\left.\begin{array}{ll} \text{If } F_r < 0.55 & K_\alpha = \left((\frac{L}{b}-1) sin\,\alpha + 1\right)^{1.24} \\ \text{If } 0.55 < F_r < 0.7 & K_\alpha = \left((\frac{L}{b}-1) sin\,\alpha + 1\right)^{0.97} \\ \text{If } F_r > 0.7 & K_\alpha = \left((\frac{L}{b}-1) sin\,\alpha + 1\right)^{0.6} \end{array}\right\} \quad 2.4$$

Choi et al. (1995) reported, the accepted angle of attack correction factors graph (Figure 2.3), suggested by Laursen and Toch (1956), could be written as an equation where the limitation $2 \leq L/b \leq 16$, for a semi-circular pier is applied:

$$K_\alpha = 0.9\left((\frac{L}{b}-1) sin\,\alpha + cos\,\alpha\right)^{0.68} \quad 2.5$$

When F_r< 0.5, Equation 2.5 predicts a scour depth similar to that of Laursen and Toch (1956) and similar to Mostafa et al. (1993) for F_r in the range 0.5 - 0.7. However, the angle of attack correction factors predicted by Equation 2.5

for F_r excess of 0.7 were larger than those determined by other previous researchers.

Fael et al. (2016) experimentally investigated the effect of the uniform single bridge pier, horizontal cross section and the angle of attack on the equilibrium scour depth. They studied five different pier shapes (circular, rectangular, rectangular with rounded nose, oblong, and zero spacing pile group) subjected to different angles of attacks (0°, 30°, 45°, 60° and 90°). They reported that Laursen and Toch (1956) equation was a precise predictor of K_{α} for $L/b = 4.0$, while it tends to over-estimate $K_{\alpha}$for $L/b = [1.33, 2.0]$. For the latter cases, the following linear equations are suggested based on the present experimental results:

$$K_{\alpha} = 1 + \frac{4\alpha}{1000} \quad for \frac{L}{b} = 1.33$$
$$K_{\alpha} = 1 + \frac{8\alpha}{1000} \quad for \frac{L}{b} = 2.0 \qquad 2.6$$

Overall, experimental methods have weaknesses in the scour depth investigations, such as small-scale laboratory models are used. In addition, the experimental approaches were not always easy to conduct and control for a complete parametric study.

In the next section, a review on the previous studies that were undertaken to investigate the scour around bridge piers based on the numerical methods is given. Its purpose is to investigate the most appropriate turbulent model to use in the study having influence of pier parameters (i.e., the pier shape, and the pier alignment to the flow direction) on the maximum scour depth. This turbulent model will be adopted for the rest of the undertaken research.

2.3 Numerical simulations of flows around bridge piers

In recent years new technologies has made it possible to develop more accurate simulation of complex flow around obstacles, due to the rapid development in computing power and CFD modelling techniques.

Simulating the complex flow around surface (bed) mounted obstacles using the DNS still comes at an unaffordable computational cost due to the strict restrictions on the grid spacing and the time step that are required to fully resolve all scales in the Navier-Stokes equations. Thus, most of the numerical investigations utilise different levels of approximation to predict the flow scales that cannot be resolved with practically sized computational grids. Here, the previous studies that have been investigated the turbulent flow around bridge piers can be classified into three parts. Firstly, the eddy resolving technique used to study the turbulent flow around bridge piers mounted on a flat or fixed bed. Secondly, CFD simulation flow around bridge piers with erodible bed. Finally, review for the numerical studies of the bridge piers subjected to flow with a range of angles of attack.

2.3.1 Flow around a bridge pier mounted on a fixed bed

The eddy resolving techniques used in studying the flow around bridge pier consist of DES and LES models. The DES approach is a hybrid URANS/LES technique that attempts to take advantage of the useful features of URANS and LES. The hybrid URANS/LES methodology depends on resolving the flow which is near to wall structures using a URANS model and resolves the coherent large scale turbulent flows in the rest of the domain. The Spalart-Allmaras (S-A) model considered the base of the DES model. Recently

developed modifications lead to the Delayed DES (DDES) used to reduce certain potentially significant deficiencies for practical applications.

Paik et al. (2007) predicted the flow around wing shaped cylinders fixed on a flat bed at R_e =1.15x10^5 configuration studied experimentally Devenport and Simpson (1990) using DES with Spalart-Allmaras model as shown in Figure 2.5. They concluded that the DES can captures most experimental trends with good qualitative and quantitative accuracy. The only discrepancy between the DES simulation and the experiment is the predicted location of the mean horseshoe vortex core, which occurs somewhat upstream of the measured location. They proposed that using DES based on Spalart-Allmaras model could be caused this discrepancy.

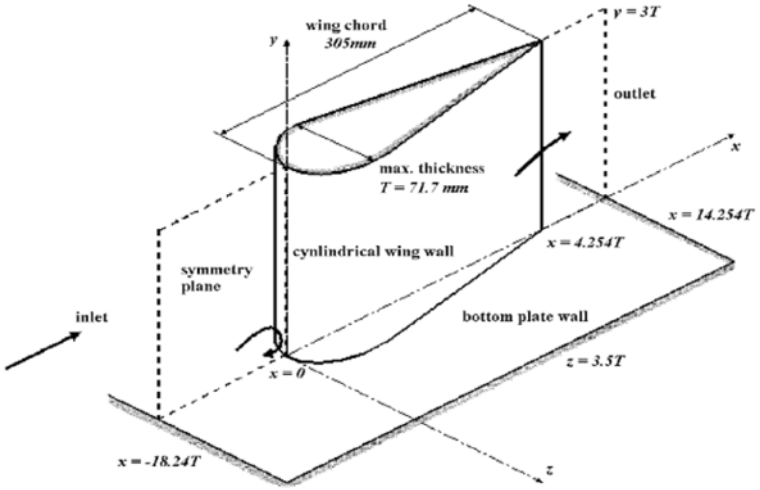

Figure 2.5: Schematic view of the wing-body junction flow (Paik et al., 2007).

Kirkil et al. (2009) used DES based on a Spalart-Allmaras RANS model to investigate the characteristics of the coherent large-scale eddies in the flow around a circular pier with an equilibrium scour hole. They studied the mechanisms of flow and turbulent structures around the cylinder and their

effects on the sediment transport during the later stage of the scour process and at a high $R_{e\mathrm{D}}$ =2.06 x10^5 (based on the diameter of the pier).

Chang et al. (2013) demonstrated the flow patterns and turbulent structure of a round nose bridge pier with three cases: the first case with the pier alone; the second when the pier is back to back with another circular column and the third case when the foundation of pier is partially exposed as shown in Figure 2.6 cases a, b and c respectively using the Spalart-Allmaras model a DES technique. They found that the bed friction velocity was primary affected by the shape and size of the pier column. In addition, they also concluded that the large-scale vortex behind the main column greatly influenced flow pattern and increased bed friction velocity around the downstream column for piers with two back-to-back columns.

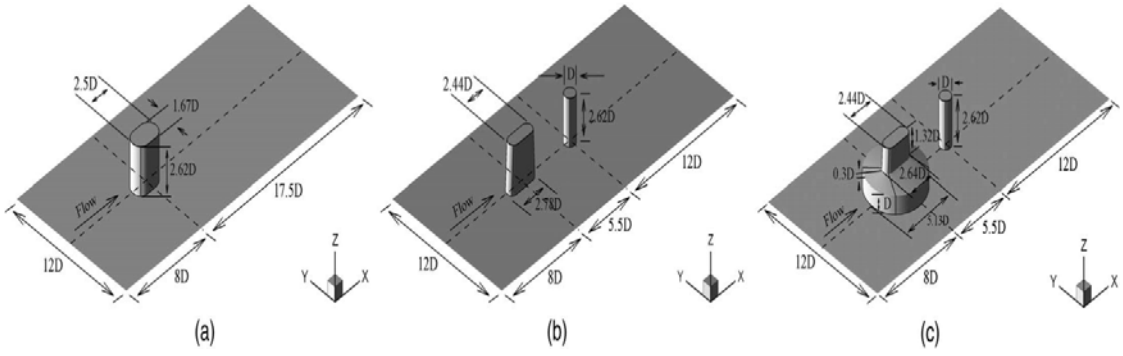

Figure 2.6: Computational domain proposed by Chang et al. (2013).

LES approach is developed using spatially and temporally filtered-averaged Navier-Stokes equations to separate the larger and smaller eddies. The separation methodology is achieved by a selection of filtering functions and setting a certain cut-off width. The large eddies are resolved directly and thus they can be captured with high accuracy. The small eddies are modelled with certain subgrid-scale (SGS) models (Versteeg and Malalasekera, 2007). The

most prominent SGS models include the standard Smagorinsky's SGS model, the dynamic Smagorinsky's SGS model, the RNG-LES model, the Wall-Adapting Local Eddy-viscosity (WALE) and the kinetic energy subgrid-scale model (Tao, 2013). All the previous studies dealing with the area of bridge scour used the simplest classical Smagorinsky with a constant coefficient (C_s) and dynamic Smagorinsky's SGS turbulence models, due to higher demand on computational requirements.

Moreover, the investigations carried out using LES to study the flow field around circular bridge piers are described. Choi and Yang (2002), used the LES model with a constant coefficient (C_s), classical Smagorinsky and wall function approach using FLOW-3D to simulate the flow around a circular pier with flat bed and equilibrium scour bed. They found that the LES able to simulate the horseshoe vortex upstream of the cylinder much better than the RNG *k-ε* model. In addition, the down-flow upstream of the pier was also investigated and they concluded that the strength of the down-flow computed by the LES is much bigger than that computed by the URANS.

Kirkil et al. (2005) presented the LES with dynamic Smagorinsky's SGS model and without wall function using massively parallel LES flow solver to study the horseshoe vortex structure and bed shear stress distribution around a cylindrical bridge pier mounted on equilibrium scoured bed with R_{eD} =1.8×10^4. They concluded that the structures of the horseshoe vortex located inside the scour hole were characterised by high pressure fluctuations and kinetic energy levels. Furthermore, the maximum bed shear stress was located underneath the horseshoe vortex structures.

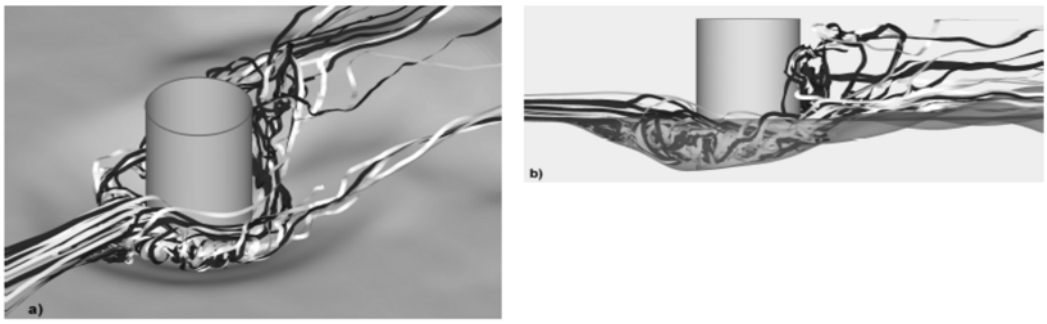

Figure 2.7: 3D velocity streamlines inside the scour hole proposed by Kirkil et al. (2005): (a) perspective view; (b) side view.

Wei and Huhe (2006) investigated numerically the turbulent flow field and the scouring effect around a circular pier using the LES method with Smagorinsky's SGS turbulence model for three scouring holes (scour depth (*S*) to pier diameter (*D*) ratio = 0, 0.375 and 0.85 respectively). They found that the value of mean bed shear stress is essentially affected by the horseshoe vortices inside the scour hole, which is shown in Figure 2.8. Whereas, at the downstream of the pier the bed shear stress gradually decreased and reached to the undistributed shear stress when the scouring depth increased.

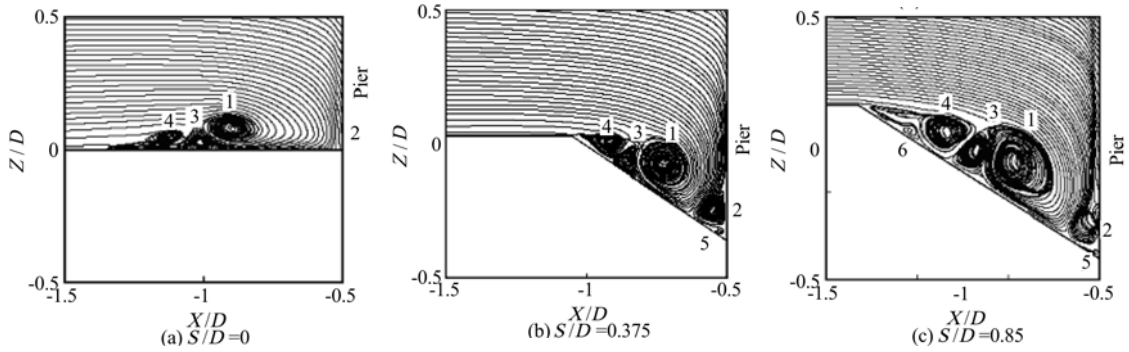

Figure 2.8: Instantaneous flow patterns of the horseshow vortex system (Wei and Huhe, 2006).

Link et al. (2008) used the LES model with dynamic Smagorinsky model, and wall function model suggested by Werner and Wengle (1993). The geometry of the developing scour hole was provided from the experimental data at time = 6 hrs as shown in Figure 2.9. During the simulation the geometry

was kept constant. The predicted results provide good evidence that the dynamics of the vortex system has a significant effect on the shape of the scour hole and vice versa.

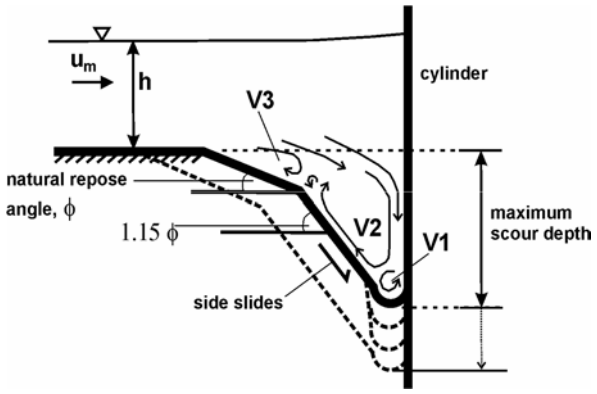

Figure 2.9: scouring mechanism in sand from topography measurements suggested by Link et al. (2008)

Kirkil et al. (2008) investigated coherent structures present in the turbulent flow around a circular bridge pier located in equilibrium scour condition. They used LES with the dynamic Smagorinsky's SGS model and without wall functions approach. They found that the maximum bed shear stress is underneath the primary necklace vortex. Furthermore, LES has enabled the authors to capture the presence of bimodal aperiodic oscillations inside the horseshoe vortices system as shown in Figure 2.10. This physical phenomena was experimentally studied in detail by Devenport and Simpson (1990) of the flow in the around the leading edge of a cylindrical wing at $R_e = 1.15 \times 10^5$. Their results showed that the horseshoe vortex is distinguished by low-frequency oscillations that induce bimodal Probability Density Function (PDF) of the streamwise and down-flow velocities close to the wall at the symmetry plane. These two separable dynamic states compatible with the backflow mode, in which the return flow of the horseshoe vortex produces a wall jet that penetrates upstream of the cylinder, and the zero-flow mode that occurs when

the near-wall flow cannot penetrate upstream, and it is ejected vertically upwards.

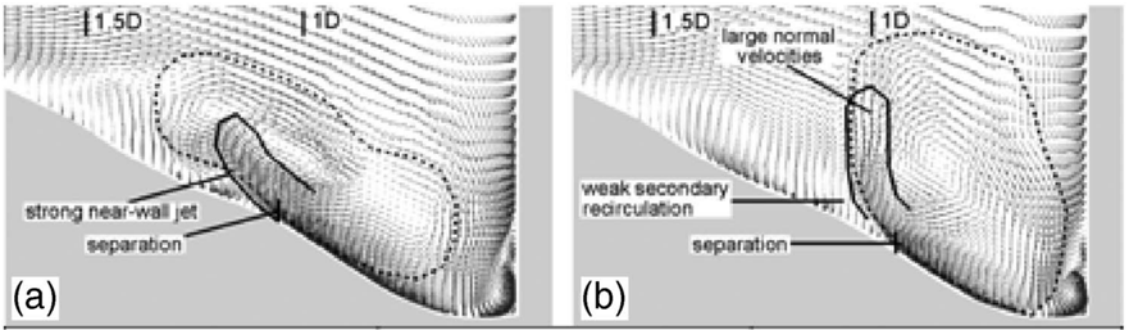

Figure 2.10: Instantaneous velocity vectors in the plane of symmetry at two-time instances at which the primary necklace vortex is in: (a) backflow mode; (b) zero-flow mode (Kirkil et al., 2008).

Pasiok and Stilger-Szydło (2010) examined the turbulent flow structure around the circular bridge pier with a scour hole using LES with dynamic Smagorinsky's SGS scale model. They concluded that LES gives good prediction when modelling the turbulent flow around the circular bridge piers. Furthermore, the simulation confirmed that all the significant turbulent flow structures such as down-flow, wake vortices, and the horseshoe vortex around a bridge pier were affected as one system. They also developed a simple Lagrangian model of particle transport. Using the flow field solutions of their LES computations, they evaluated the forces and trajectories of particles as shown in Figure 2.11.

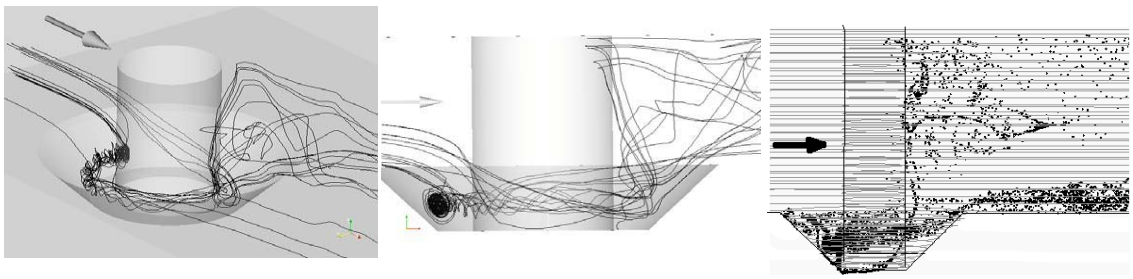

Figure 2.11: Instantaneous velocity streamlines and flow particles around the cylinder with scour hole developed by Pasiok and Stilger-Szydło (2010).

Apsildis (2012) investigated the initial stages of the pier scour process by focusing on the characteristics of the turbulent horseshoe vortex as an important scour factor. The study was applied to the flow past a circular bridge pier placed on a flat bed, using LES with hybrid staggered/non-staggered grid. They found that the LES could capture the presence of secondary small vortices that formed under the main turbulent horseshoe vortex and wrapped around it in the horseshoe vortex-wall interaction region as shown in Figure 2.12.

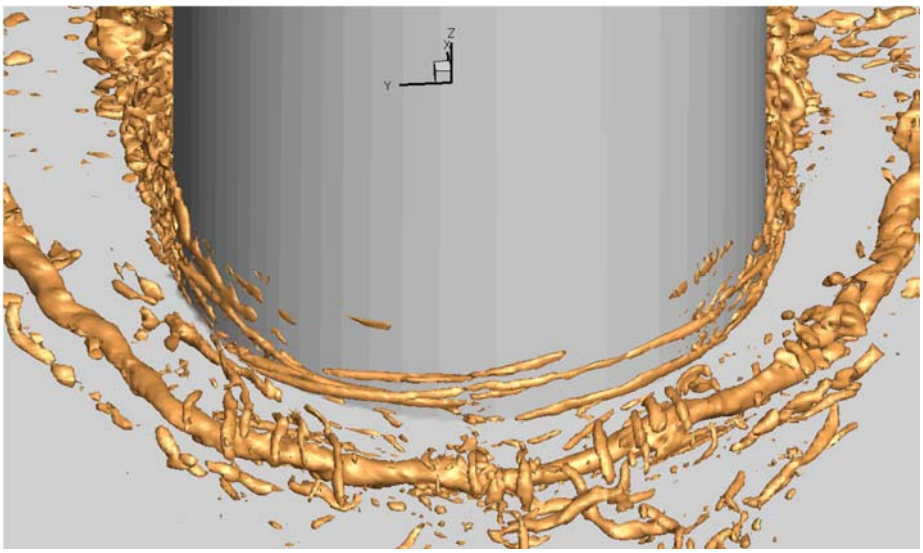

Figure 2.12: Visualisation of instantaneous vortical structures obtained from the LES study by Apsildis (2012) using the Q-criterion.

Kardan (2012) investigated the turbulent flow and bed shear stress around and downstream of the circular bridge pier mounted on flat bed with $R_{e\mathrm{D}}$=8.0×10^4. The simulation was undertaken using various turbulent flow models (*k*-*ε*, RSM, and LES). They found that LES presented more accurate results for simulating the wake vortices shedding at the downstream of the bridge pier than other URANS models, and for evaluating the vortex fluctuation and predicted bed shear stress.

Ramos et al. (2016) studied the flow around a circular cylinder mounted on flat and fixed bed using LES approach with a constant Smagorinsky model C_S =0.1. They concluded that the LES is capable of qualitatively investigating the characteristic flow features around the pier, such as the horseshoe vortex system, and the vortex shedding in the wake. The predicted bed shear stress magnitudes agree well with the observations that are reported by the experiments.

There are very few studies investigating the flow field around non-circular pier shapes using LES. Tseng et al. (2000) presented the 3D LES together with Smagorinsky's SGS turbulence model and wall function method to investigate the vortex structures patterns around bridge piers with different shapes, namely square and circular on a rigid flat bed. They concluded that the down-flow is found at the upstream of the pier and this affects the creation of the horseshoe vortex. In addition, they found that the strengths of the down-flow and horseshoe vortex in the square pier are greater than in the case of the circular pier as shown in Figure 2.13. However, in the case of a circular shape the horseshoe vortex formed closer to the front face than for a square pier as shown in Figure 2.14.

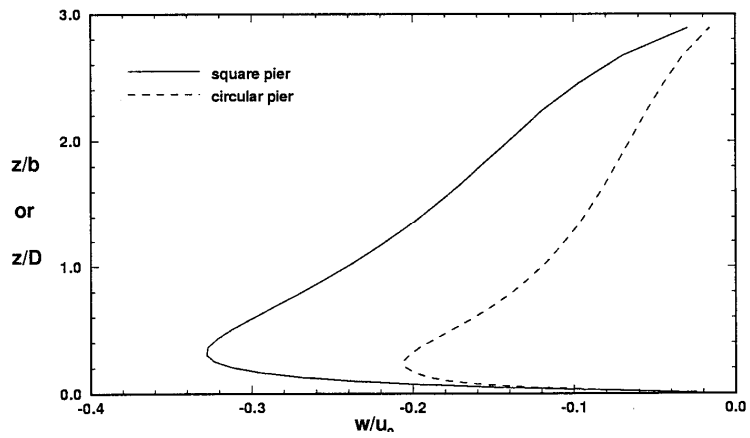

Figure 2.13: comparison of down-flow velocity along the central vertical upstream of the cylinder proposed by Tseng et al. (2000).

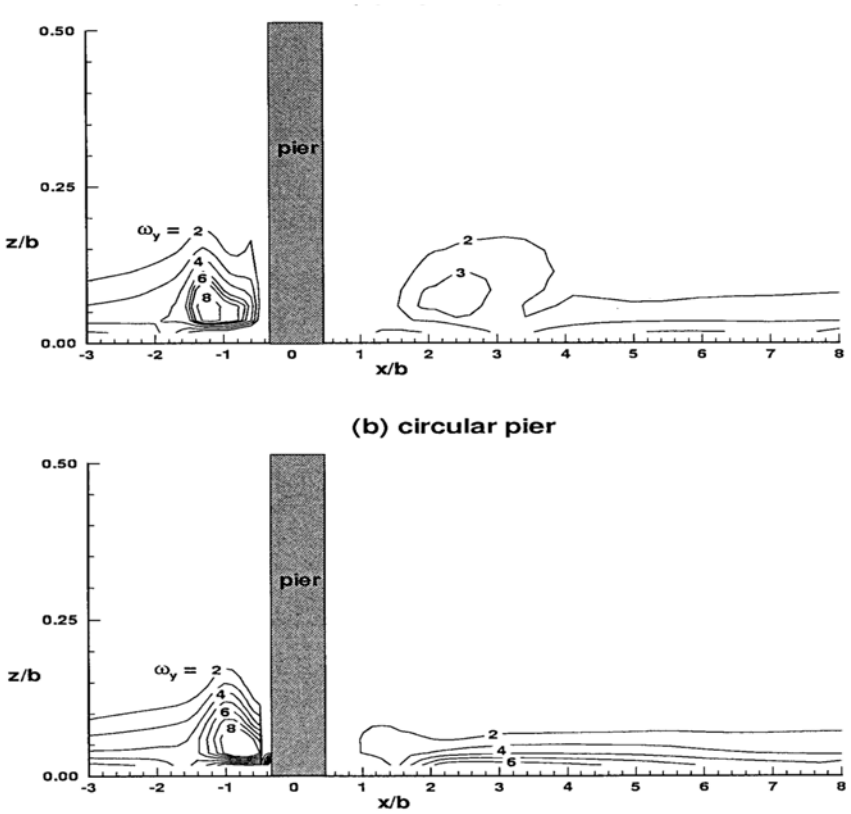

Figure 2.14: Mean vorticity ω_y on the plane of symmetry proposed by Tseng et al. (2000) .

Younis and Abrishamchi (2014) predicted the unsteady flow structure around a 3D square bridge pier mounted on a flat bed at R_e in the range 10^4–10^5. They used two approaches to analyse their model. The first method was by improving LES with classical Smagorinsky's model, and the second method used URANS with *k-ε* turbulence model to calculate the output Reynolds stresses to solve the model. They found that the use of URANS can produce similar predictions to those obtained with LES; however only by using LES can the effects of turbulent vortex shedding be accurately predicted.

Overall, LES has the ability of resolving the strong unsteady dynamics in the region close to the bridge piers subjected to turbulent flow. However, the applications of computational simulations with LES are limited with simple subgrid-scale model (classical Smagorinsky with constant coefficient and

dynamic Smagorinsky's SGS turbulence models) mainly due to computational power requirements.

2.3.2 Flow around a bridge pier with erodible bed

Several studies were carried out to investigate the effects of coherent structures around bridge pier on the scour depth. Some of these studies used single phase models of sediment transport by coupling the RANS or URANS methods to simulate the flow field around the cylinder, and an empirical formula to simulate the sediment movement. The 3D simulations of Olsen and Melaaen (1993) utilised the RANS equations with k-ε turbulence model and the bed-load formula of Van Rijn (1986) to solve the conservation of mass equation at the bed and calculate the scour around a cylindrical pier. The bed elevation had been adjusted based on the condition that the maximum change of 10% of the water depth was allowed. The updated bed geometry then used as input for the second water flow calculations. This procedure was continued until the maximum scour depth equal to that observed from physical model. The resulting scour hole compared well with the measured scour hole from the experimental study. Also, other flow features given by the numerical model agreed with observations from the experimental study.

Adhikary et al. (2009) proposed an iterative computational methodology with a single-phase slip-flat-top surface with re-moving boundary formulation by means of empirical correlation of critical shear stress to characterise initiation of sediment motion. Their study deals with the simulation of turbulent flows over inundated bridge deck and evolution of scour hole under various flooding conditions. They found that the computational model demonstrated stable and converged solutions for the evolution of the scour hole depth and size using a

constant empirical critical-shear-stress value as shown in Figure 2.15. Since the transient terms are neglected in the RANS model, the above studies done by Olsen and Melaaen (1993) and Adhikary et al. (2009) do not confirm that the RANS model could be capable of dealing with all cases of scour around pier. Nor is it confirmed that the model could compute accurate maximum scour depths.

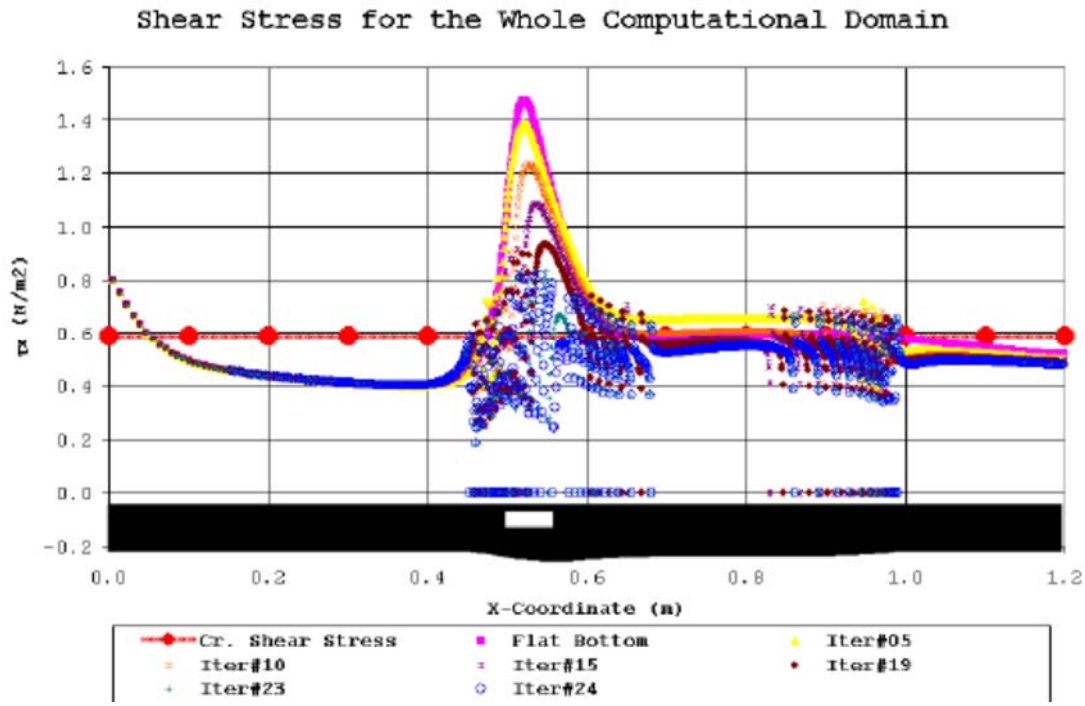

Figure 2.15: Shear stress distribution along bottom boundary at different iterations along the bottom of whole domain (Adhikary et al., 2009).

Olsen and Kjellesvig (1998) continued the work reported in Olsen and Melaaen (1993). The numerical model was solved using URANS the *k-ε* turbulence model. The investigation was not limited to the initial stage of scour, which was the case in Olsen and Melaaen (1993), the entire scour process was simulated. They concluded that the maximum scour depth corresponds reasonably well with empirical formulae. Also, other calculations for flow characteristics such as the development of the scour hole, the shape of the

scour hole and the water surface elevation around the cylinder gave good agreement with observations from physical model studies.

Roulund et al. (2005), performed experiments and numerical simulations of scur around a cylindrical pier in live bed conditions at $R_{e\mathrm{D}}$=4.6x10^4. A sediment transport and scour model were incorporated into the URANS. They used the *k-ω* turbulence model and computed the boundary conditions with an analytical expression for the shear-stress. For the sediment transport simulations, Roulund et al. (2005) utilised the equilibrium bed-load formula of Engelund and Fredsøe (1976) to compute a sediment velocity proportional to the shear velocity at the bed, assuming constant particle velocity on the balance of momentum for the sediment. The bed elevation was computed from the mass conservation at the bed, using a time-step larger than the flow solution and without considering the moving boundary effects.

Huang et al. (2009) conducted a 3D model to examine the large-scale effect on turbulent flow and sediment scour around circular bridge pier. The results obtained by 3D modelling were compared with the results from a physical model, and depended on the F_r similarity. The two-phase (water and sand) Eulerian model was used to simulate the local scour. The top layer is phase water, and the bottom layer is phase sand. The maximum scour depth and the deepest scour hole in front of the cylinder are reasonable in good agreement with those from the experiments conducted by Yanmaz and Altinbilek (1991).

Khosronejad et al. (2012) studied the clear water scour around bridge piers with different shapes as shown in Figure 2.16, using URANS equations with *k-*

ω model to simulate the turbulent structures around the pier, and the curvilinear immersed boundary method to model the fluid sediment interaction. They divided the model into the fluid domain and sediment domain and solve the governing equations for the flow and the bed morphodynamical equation separately in each domain, the interaction between the two domains had been accounted by applying boundary conditions at the sediment/water interface. They concluded that the URANS method could predict the flow field around complex shapes (diamond pier); however, this model was found inadequate for prediction of the scour around blunt edges and cannot sufficiently resolve the horseshoe structures at the region near the bed.

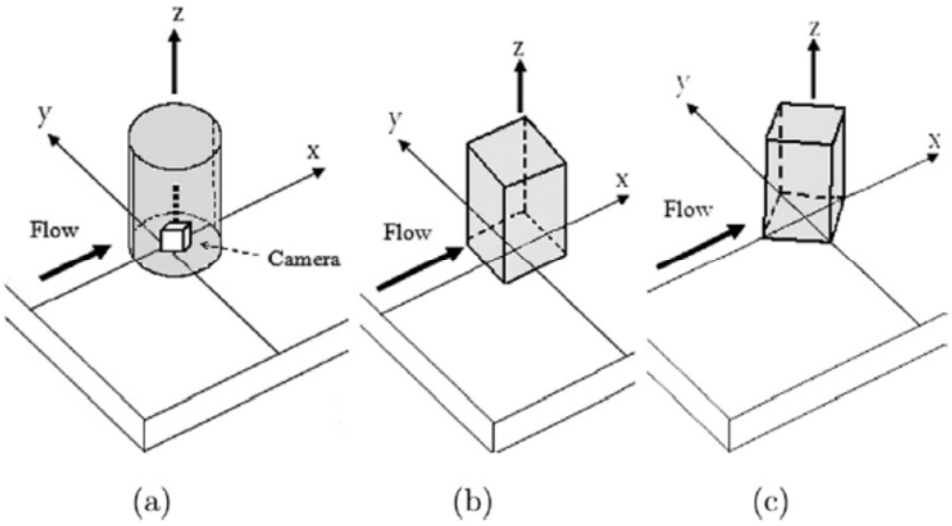

Figure 2.16: Schematic of the three pier shapes studied by Khosronejad et al. (2012): (a) circular cylinder, (b) square cylinder, and (c) diamond cylinder.

Xiong et al. (2014) simulated 3D scour behaviour around a circular bridge pier by coupling k-ε model with dynamic mesh technique. They validated the maximum scour depth with the experiment reported by Yanmaz and Altinbilek (1991). The predicted results presented a discrepancy in the scour shape upstream of the cylinder, and this discrepancy is primarily attributed to the use

of *k-ε* turbulence model. Other flow fields show a close agreement between the simulation and experiment.

To explore the direct effect of the coherent structures on sediment grains, Xiong et al. (2016) simulated the scour around bridge piers. They proposed Eulerian two-phase flow model in conjunction with the *k-ε* wall function model. The development of a scour hole around a bridge pier in a mobile bed strongly depends on the local flow field induced by the cylinder, which in turn depends on the approach flow conditions (Guemou et al., 2016).

As said, the studies implementing URANS models to simulate the scour evolution, it can be concluded that despite URANS giving good agreement with observations from physical model studies and corresponding reasonably well to empirical formulas, predicted results can show discrepancy in the scour shape upstream of the piers, and that this discrepancy is primarily attributed to the fact that the URANS model does not have the capability to capture all of the characteristics of the horseshoe vortex system upstream the bridge pier. It is apparent that no researchers have coupled the high resolving techniques and scour evolution process around bridge piers except Escauriaza and Sotiropoulos (2011). They used a URANS/LES such as DES model together with a bed-load transport model in which the sediment motion is solved using a Lagrangian-Eulerian approach by assuming that the sediment consists of spherical particles. They focused their research on the interactions between turbulent horseshoe vortices and a mobile bed. In addition, they also studied the initial scour bed formation within and around the scour hole as shown in Figure 2.17. The maximum scour depth computed from their study was found to be minimal when compared with the experimental studies that have the

same flow characteristics. All the previous studies highlight the importance of coupling the sediment dynamics with a coherent structure resolving turbulence model.

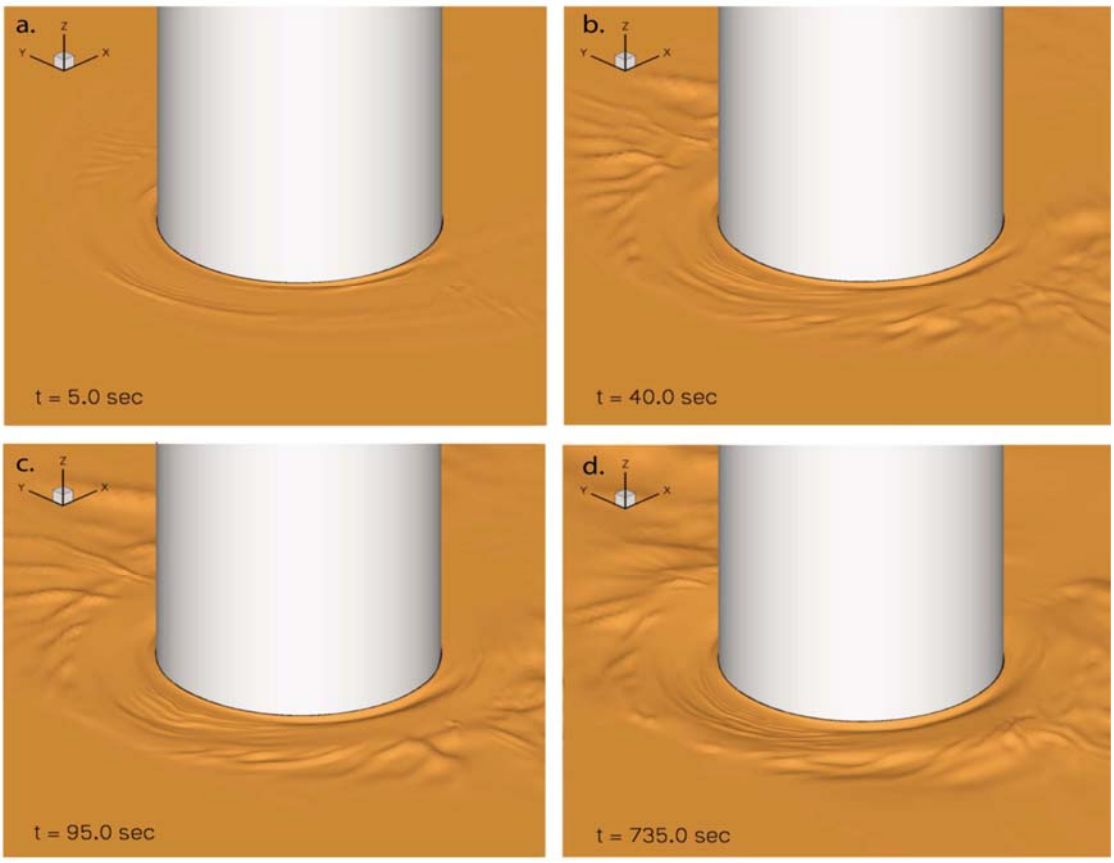

Figure 2.17: 3D images of the bed elevation, showing the evolution of the scour hole around the cylinder (Escauriaza and Sotiropoulos, 2011).

2.3.3 Numerical studies on the pier alignment to the flow direction

All the previous mentioned studies were carried out with zero angle of attack as there was no relative orientation between the pier and the incoming flow. For bridge piers located in a river bend or near the river bank the flow direction and the pier direction will not coincide and the angle between the two is called the attack angle. Furthermore the change of about 30% in the angle of attack of the approaching flow at high flood conditions is not uncommon

(Chang et al., 2011). This motivates the need to investigate the changes in the coherent flow structure and its relationship with the sediment transport mechanisms.

There are very few studies on the effect of pier shape and angle of attack around the bridge pier based on numerical investigations. Briaud et al. (2004) studied the effect of attack angle on the maximum shear stress for the rectangular pier shape using numerical methods and proposed the correction factor for calculation of the maximum shear stress Equation 2.7.

$$K_\alpha = \frac{\tau_{max}}{\tau_{max(0deg)}} = 1 + 1.5\left(\frac{\alpha}{90}\right)^{0.57} \quad 2.7$$

Tao and Yu (2014) studied the flow field around piers with different configuration using 3D; *k-ω* model. They quantify the effect of the angle of attack on the maximum shear stress values for different aspect ratios (L/b =2, and 4). They adopted the relation for K_α in Equation 2.8, relating the angle of attack, maximum shear stress, and aspect ratio:

$$K_\alpha = \frac{\tau_{max}}{\tau_{max(0deg)}} = \left(\frac{L}{b} sin\,\alpha + cos\,\alpha\right)^n \quad 2.8$$

where n is an exponent index and it's found to be equal to 0.9, depending on the fit to data undertaken by Tao and Yu (2014) using a regression method.

In a related DES study, Kirkil and Constantinescu (2010) investigated the flow past a rectangular cylinder at an angle of attack of 90° with equilibrium scour hole, as shown in Figure 2.18. They concluded that, for this orientation of the cylinder, the maximum scour depth at equilibrium scour conditions is observed. Their investigations have also shown important changes that takes place in the sediment entrainment mechanisms between piers of circular shape

and rectangular piers at high angle of attack with the same projected width. However, the direct relevance of this case is rather limited for the present study, as the angle of attack is rarely more than 45° on a rectangular in-stream.

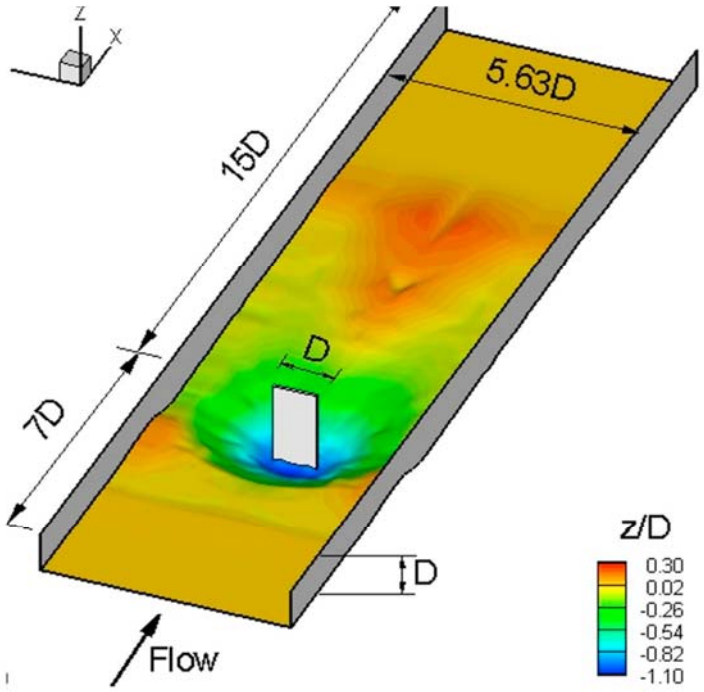

Figure 2.18: 3D view of the computational domain proposed by Kirkil and Constantinescu (2010).

Chang et al. (2011) investigated the vortical structure of the flow around a rectangular pier with high aspect ratio and with R_{eD}= 2.4x10^5, with small angles of attacks (0° and 15°) and moderate angle of attack (30°) using DES as shown in Figure 3.19. For small angles of attack, the results showed that the horseshoe vortex system played a relatively minor role in the entrainment of sediment from the bed and the amplification effect of the bed friction velocity due to the passage of the roller vortices was relatively small. For moderate attack angle, the bed friction velocity was significantly amplified due to the dynamics of the horseshoe vortex and the roller vortices. In general, all the previous studies deal with bridge scour, which caused by the effect of

horseshoe vortices around the bridge piers and produce sediment motion and scour. The horseshoe vortex system has a significant effect on the bed shear stress increment, and when the bed shear stress around the pier foundation becomes greater than the critical shear stress of the soil particle the initiation of the sediment motion will start. After gathering all the information from the previous studies, it appears that there is no one using LES to study the effect of pier alignment on the maximum scour depth.

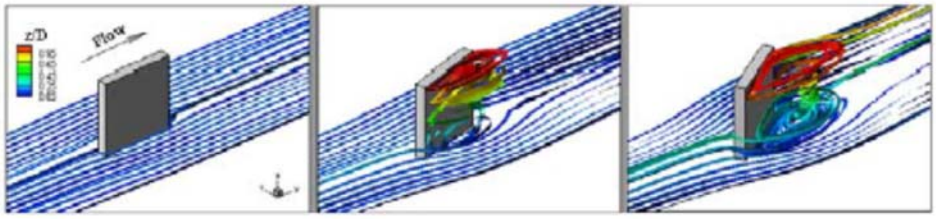

Figure 2.19: Visualisation of the time-averaged flow around the cylinder, the angles of attack are 0°, 15° and 30° respectively from left to right (Chang et al., 2011).

2.4 Findings of the literature review

The findings reveal a lack of data and research on the topic of investigation undertaken in this research, and it is discussed as:

- The prior experimental studies have made a significant progress with respect to the maximum depth of scour and the turbulent flow around the bridge piers. However, it was found that they have weaknesses in the scour depth investigations, such as the limitation that small scale laboratory models are used. In addition, the experimental approaches are not always easy to conduct and control for the parametric studies. These factors reflect on the predicting of the angle of attack correction factor equations.

- Since the transient terms are neglected in the RANS model, it is not able to compute accurately the maximum scour depth at the equilibrium condition.
- Despite this the URANS gave good agreement with observations from physical model studies and corresponds reasonably well with empirical formulas that are used in scour depth prediction. The predicted results presented discrepancies in the scour shape upstream of the cylinder, and these discrepancies are primarily attributed to the use of the URANS model that does not have the capability to capture the whole characteristics of the horse shoe vortex system upstream the bridge pier.
- DES has the capability to resolve the unsteady coherent structures in the turbulent flow past the bridge pier. As a comparison between the results from studying the mean flow and turbulence statistics around circular bridge piers using DES and LES methods, Kirkil et al. (2009) concluded that the predicted results from DES at a R_{eD}=1.62 x10^4 were very close to LES results at the same R_e. The DES model together with a bed-load transport model in which the sediment motion is solved in a Lagrangian-Eulerian framework by assuming the sediment consists of spherical particles. The maximum scour depth computed from their study was very small compared with that measured by the experimental study from the literature that has the same flow characteristics. All the previous studies highlight the importance of coupling sediment dynamics with a coherent structure resolving turbulence model.

Based on a review undertaken to investigate the CFD methods which were implemented to study the flow around obstacles and scour process. LES approach was adopted alongside dynamic meshing technique to enable the simulation of scouring around a bridge pier. The dynamic mesh updating technique is implemented to move the bed and assures a practical and accurate scour simulation by individually updating the domain's nodes of the riverbed at each time step. No other researcher appears to have used LES to study the effect of pier alignment on the maximum scour depth, and based on previous studies, the adoption of the LES approach in this study has the following advantages over other CFD models:

- LES has the ability to resolve strong unsteady dynamics in the region close to bridge piers subjected to turbulent flow.
- LES can capture the presence of bimodal aperiodic oscillations inside the horseshoe vortex system.
- LES is able to capture the presence of secondary small vortices that are formed upstream of the bridge piers, behind the main horseshoe vortex.
- LES gives more accurate results for simulation of the wake vortices shedding downstream of the bridge pier compared to other URANS models. It is also capable showing accurate results for evaluating the vortex fluctuation and predicted bed shear stress.
- LES is capable of qualitatively investigate the characteristic flow features around the pier: the horseshoe vortex system; the vortex shedding in the wake; and the predicted bed shear stress.

To further consider the advantages of LES over other CFD methods, validation of the most significant experiments done by Dargahi (1989) for fixed bed and Dargahi (1990) for mobile bed were undertaken. This is described in detail in the next two chapters (chapter 3 for fixed bed, and chapter 4 for erodible bed).

Chapter 3

Turbulent Flow past a Circular Cylinder Bridge Pier Mounted on a Flat Bed

The purpose of this chapter is to describe the effect of numerical parameters of the LES on the predicted time-averaged flow and turbulent statistics of the flow around a circular cylinder. The results from the LES will be compared with two URANS models, *k-ε* standard and *k-ω* SST. *k-ε* standard is commonly used in industry applications for the prediction of flow around circular cylinders; however, the *k- ε* methods has shown poor predictions for near-wall behaviour in separated flow conditions (Wilcox, 2006). On the other hand Nieto et al. (2015) concluded that *k-ω* SST provides the right balance between computational cost, robustness and accuracy. A comparison between the results of LES and two URANS methods, *k-ε* standard and *k-ω* SST will be defined. Furthermore, all the methods used will be compared to existing experimental data reported by (Dargahi, 1989).

Section 3.1 describes the equations that are going to be used. Section 3.2 states the geometry and boundary conditions of the computational domain. A set of fully developed flow results from a precursor RANS calculation have been investigated in Section 3.3. Section 3.4 presents the turbulent inlet condition, the discretisation, and the computational grid for the LES main domain. Section 3.5 explores the model predictors in the region close to the cylinder and discusses the consequence of grid resolution. The distribution of

the turbulent kinetic energy has been also studied in Section 3.5. in order to show that the energy transferred from large to small eddies is achieved by inertial forces as demonstrated by the $k^{-5/3}$ proportionality of the energy spectra E(k). In addition, a 3D dynamics of the coherent structures around the cylinder have been identified using the Q criterion. This is considered to be effective vortex indicator in wall turbulence, to visualise the instantaneous resolved flow fields and study the resulting coherent structures of the horseshoe vortex system around the cylindrical pier.

3.1 Governing equations

For all the simulation strategies for the turbulent flows, whether its DNS, LES, or URANS method, the Navier-Stokes equations are the fundamental part. For the undertaken research, incompressible time-dependent Navier-Stokes equations is considered along with conservation of mass to describe the flow for the spatial domain, as given below:

Mass conservation: continuity equation

$$\frac{\partial u_i}{\partial x_i} = 0 \tag{3.1}$$

Momentum conservation: Navier-Stokes equations

$$\frac{\partial u_i}{\partial t} + \frac{\partial u_i u_j}{\partial x_j} = -\frac{1}{\rho}\frac{\partial P}{\partial x_i} + v\frac{\partial^2 u_i}{\partial x_i \partial x_j} \tag{3.2}$$

where, u_i and u_j are the velocity vector components, P is the pressure, ρ is the fluid density, and v is the kinematic molecular viscosity.

3.1.1 Direct Numerical Simulation (DNS)

DNS is the branch of CFD devoted for solving the Navier-Stokes equations without any approximation. In the event of turbulent flow in this study, the mesh

and time stepping must be sufficiently fine to resolve the smallest eddies down to the Kolmogorov scale. This ability, however, comes at extreme computational cost, which prevents DNS from being used for many real world engineering applications. This research will therefore consider CFD approaches that include a range of approximations that can model the turbulence behaviour.

3.1.2 URANS

URANS equations for a turbulent flow are related to the principle of the Reynolds decomposition of the velocity u_i into a mean $\overline{u}_i$ and fluctuating part u_i'.

$$u_i = \overline{u}_i + u_i' \tag{3.3}$$

where $\overline{u}_i$ denotes the time average velocity. The resultant of applying the decomposition and time-averaging on the standard Navier-Stokes Equations 3.1 and 3.2 are the RANS set as shown below:

$$\frac{\partial \overline{u_i}}{\partial x_i} = 0 \tag{3.4}$$

$$\frac{\partial \overline{u_i}}{\partial t} + \frac{\partial \overline{u_i u_j}}{\partial x_j} = -\frac{1}{\rho}\frac{\partial \overline{P}}{\partial x_i} + \nu \frac{\partial^2 \overline{u_i}}{\partial x_i \partial x_j} - \frac{\partial \overline{\acute{u}_i \acute{u}_j}}{\partial x_j} \tag{3.5}$$

where the last term on the right hand side is the Reynolds stress tensor. In order to solve this system it must to be closed by providing extra model equations. There are numerous conceivable outcomes of solving this closure problem. In this study two models of URANS will be used (i.e. *k-ε* standard, and *k-ω* SST) to compare the results of unsteady flow around circular cylinder with respect to LES.

3.1.3 Large Eddy Simulation Model (LES)

LES is an increasingly popular technique for simulating turbulent flows. It follows the Kolmogorov's theory that describes the transferred energy from the large eddies to the small eddies. The concept of LES is to simulate explicitly the movement of the large scale eddies by using the governing 3D time-dependent equations and to model, separately; the movement of the small scale eddies by using a SGS. This evades from the issue in URANS method of having to model the large scale eddies, and at the same time the problem of DNS of having to resolve the small scale eddies.

Figure 3.1 illustrates the concept of LES in relation to energy flux and energy spectrum. The large eddies which has energy from the mean flow are unstable and break up, transferring their energy to smaller eddies in the energy cascade. For these small scale eddies which are modelled using a SGS model, the kinetic energy is dissipating by the mechanism of viscosity. The separation between the solving of large scales and modelling of small scales should occur in a spectral region where only energy transfer happens to ensure that only the dissipative motions are modelled.

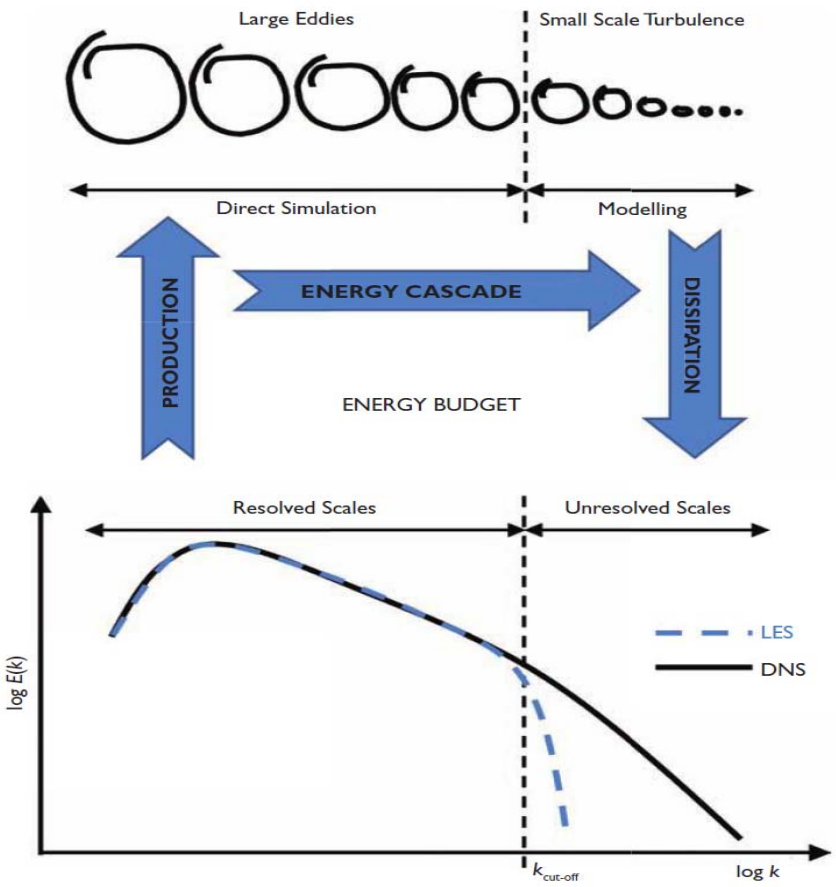

Figure 3.1: Concept of Large Eddy Simulation in relation to energy flux and energy spectrum (Rodi et al., 2013).

In the LES, the spatially filtered 3D time-dependent Navier-Stokes equations are solved numerically for all eddies with a scale larger than the mesh size of the chosen numerical grid, while the small scale eddies; mainly dissipative motion is simulated by SGS model.

The subgrid-scale stresses resulting from the filtering operation are unknown, and require modelling. The subgrid-scale turbulence models usually employ the Boussinesq hypothesis (Hinze, 1975), and calculate the SGS stress τ_{ij} using:

$$\tau_{ij} - \frac{1}{3}\tau_{kk}\delta_{ij} = 2\mu_t\bar{S}_{ij} \qquad 3.6$$

where μ_t is the subgrid-scale turbulent viscosity. τ_{kk} is the isotropic part of the subgrid-scale stresses. $\overline{S}_{ij}$ is the rate-of-strain tensor for the resolved scale defined by:

$$\bar{\mathrm{S}}_{\mathrm{ij}} = \frac{1}{2}\left(\frac{\partial \overline{\mathrm{u}}_{\mathrm{i}}}{\partial \mathrm{x}_{\mathrm{j}}} + \frac{\partial \overline{\mathrm{u}}_{\mathrm{j}}}{\partial \mathrm{x}_{\mathrm{i}}}\right) \quad 3.7$$

The simple subgrid-scale-model was first proposed by Smagorinsky (1963). In Smagorinsky-Lilly model, the eddy-viscosity is modelled by:

$$\mu_{\mathrm{t}} = \rho \mathrm{L}_{\mathrm{s}}^2 |\bar{\mathrm{S}}| \quad 3.8$$

where L_s is the mixing length for subgrid scales and $|\bar{S}| \equiv \sqrt{2\bar{S}_{ij}\,\bar{S}_{ij}}$. L_s is computed using:

$$L_s = min(kd, \mathrm{C_s}\,\Delta) \quad 3.9$$

where k is the von Karman constant, d is the distance to the closest wall, C_s is the Smagorinsky constant, and Δ is the local grid scale. Δ is computed according to the volume of the computational cell using:

$$\Delta = \mathrm{V}^{1/3} \quad 3.10$$

Lilly derived a value of 0.17 for C_s for homogeneous isotropic turbulence in the inertial sub-range. However, this value was found to cause excessive damping of large-scale fluctuations in the presence of mean shear and in transitional flows as near a solid boundary. It has to be reduced in such regions. In other words, C_s is not an universal constant, which is the most serious vital of this simple model. Nonetheless, a C_s value of around 0.1 has been found to yield the best results for a wide range of flows.

In this study the sub-grid-scale eddy viscosity μ_t is computed using the dynamic Smagorinsky model proposed by Germano et al. (1991), and modified

by Lilly (1992). In this model, the coefficient C_s is computed dynamically based on the information provided by the resolved scales of motion. The dynamic procedure thus obviates the need for users to specify the model constant C_s in advance.

The C_s obtained using the dynamic Smagorinsky-Lilly model varies in time and space over a fairly wide range. To avoid numerical instability, C_s is clipped between zero and 0.23.

3.2 Configuration investigated

The flow studied in this chapter was set up to correspond to the experiment conducted by Dargahi (1989), so that a comparison with experimental data is possible. The Dargahi (1989) experiments were carried out in a rectangular cross section flume of width B = 1.5m, and water depth of H = 0.2m. A circular cylinder of 0.15m diameter was placed vertically on the flume bed along the centre line at a distance of 18m from the inlet. Sand with a mean diameter d_{50}= 0.365 mm was placed in flume. The R_e of the approaching flow based on the cylinder diameter was R_{eD}= 3.9×10^4. Table 3.1 lists the basic dimensions and scales considered in the investigation.

The computational domain used to simulate the turbulent flow around a single circular cylinder is given in Figure 3.2. The coordinate system used in this study is also shown.

Table 3.1: Dimensions of the flow studied, with the corresponding Reynolds and Froude numbers.

U_{Mean} (m/s)	D (m)	B (m)	H (m)	R_{eD}	F_r
0.26	0.15	1.5	0.2	3.9×10^4	0.19

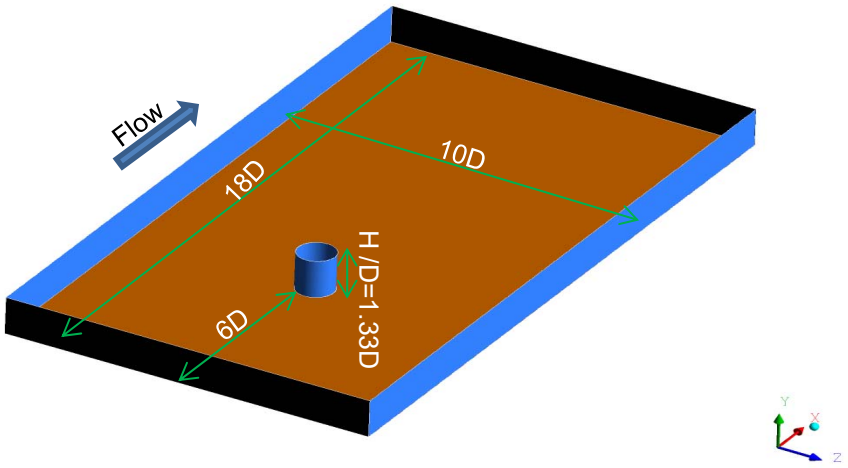

Figure 3.2: Geometry of the computational domain, showing the section of the channel considered in the simulations.

The vertical direction of the domain extends in the full water depth (H), and in streamwise direction the inflow boundary condition is located at a distance of 6 times the diameter of the cylinder (D) upstream of the cylinder. A fully developed turbulent flow at the inlet is specified by using a separate RANS simulation upstream of the cylinder. For LES calculations a vortex method was used at the inlet of the main domain to randomly perturb the fully developed mean velocity profile. The turbulent kinetic energy and turbulent dissipation energy profiles were also computed from results of an auxiliary steady RANS simulation. According to the study conducted by (Sarker, 1998), if the flow is 12 times the pile diameter away from the pile centre, it can be regarded as an area with no pile influence. Therefore to achieve non-reflecting characteristic boundary conditions in the numerical model, the outlet boundary at the exit is placed at 12D downstream of the pier.

No-slip boundary conditions are applied on the bottom wall, cylinder surface, and the sidewalls of the channel. Note that the width of the channel of

interest is narrow enough to directly affect the flow features in the vicinity of the cylindrical pier. For this reason the side walls of the channel are included in the calculation and treated as no-slip walls.

The free surface is approximated as a flat and rigid with free slip condition, which is justified as the channel $F_r = 0.19$. Simulating free slip wall boundary condition has been achieved by using wall boundary condition with zero specified shear. Most studies of flow past a surface mounted bodies were conducted using this boundary condition such as Tseng et al. (2000), Paik et al. (2004), Kirkil et al. (2005), Kirkil et al. (2008), Link et al. (2008), Palau-Salvador et al. (2008), Kirkil and Constantinescu (2009), Kirkil et al. (2009), Kirkil and Constantinescu (2010), Chang et al. (2011), Chang et al. (2013). The advantage of this assumption is that does not need a huge amount of CPU time as a free surface modelled and its acceptable approximation for the case of relative large water depth considered in this study.

To study the grid size sensitivity of the solution, the computational domain has been discretised using hexahedral grid and simulations are undertaken with two computational meshes ($12x10^6$ grid cells and $24x10^6$ grid cells). The flow field is computed to examine whether the essential dynamics of the horseshoe vortices system can be captured with similar accuracy using different grid densities.

For both grid densities, an O-type grid has been used for the region close to the cylinder as shown in Figure 3.3. In this region the finest grids are closest to the cylinder, and have a cylindrical shape with an external diameter equal to 3D, (taking the coordinate origin at the centre of the cylinder). This distribution

allows an efficient clustering of grid nodes, without producing high aspect ratio cells. This can happen if a single grid size was used for the entire domain.

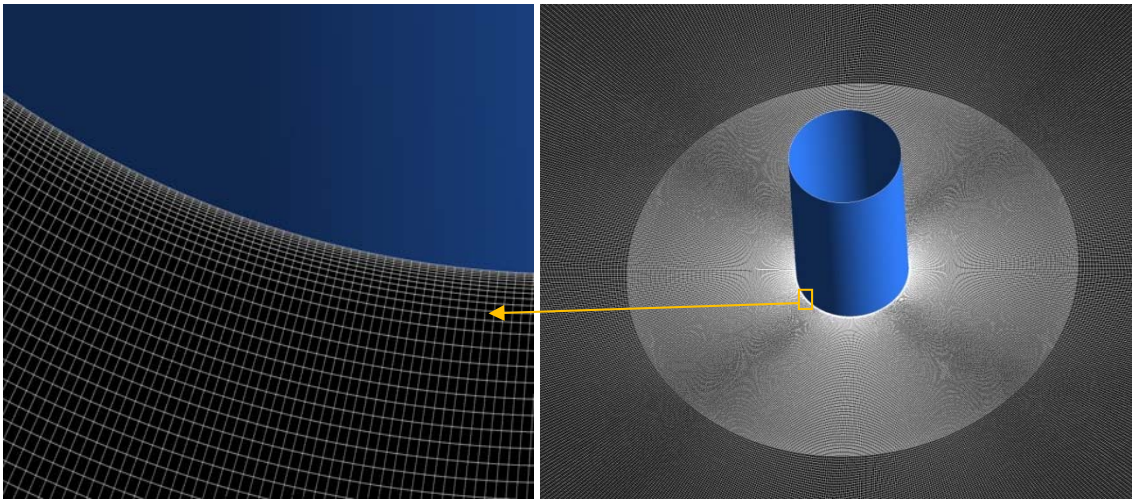

Figure 3.3: Hexahedral grid layout in the region close to the cylinder.

3.3 Precursor calculations and inflow conditions

To achieve a fully developed flow in the inlet boundary condition of the main domain, a separate RANS simulation was undertaken of the upstream section of the channel using the *k-ε* turbulence model at the same R_e, and the same width and depth as in the computational domain for the cylinder calculation. The residual tolerance has been set to $1x10^{-4}$ for all equations (Menter, 2012).

To produce the actual length configuration upstream of the cylinder and to achieve a fully developed flow which was used in the experiments of Dargahi (1989 and 1990), inflow profiles for the velocity field and turbulence quantities are obtained at 85(H) downstream of the entrance of the rectangular channel. where H is the total water depth.

Figure 3.4 shows the boundary layer development to fully developed flow in the precursor domain. There is no defined criterion for flow establishment length in channels. One of the criteria suggests finding the established length,

which is used in this study, is the mean velocity profile along the whole the cross section; which remains the same. This criterion takes into consideration the effect of wall on the velocity field in the cross section. Depending on this criterion, the fully developed flow is located at distance equal to 65H from the inlet. The boundary layer thickness δ increases with distance from the entrance of the domain, after a certain distance the boundary layer reaches a consistent height (0.1(H)), and the velocity profile becomes invariant. Past this distance, the flow is assumed fully developed.

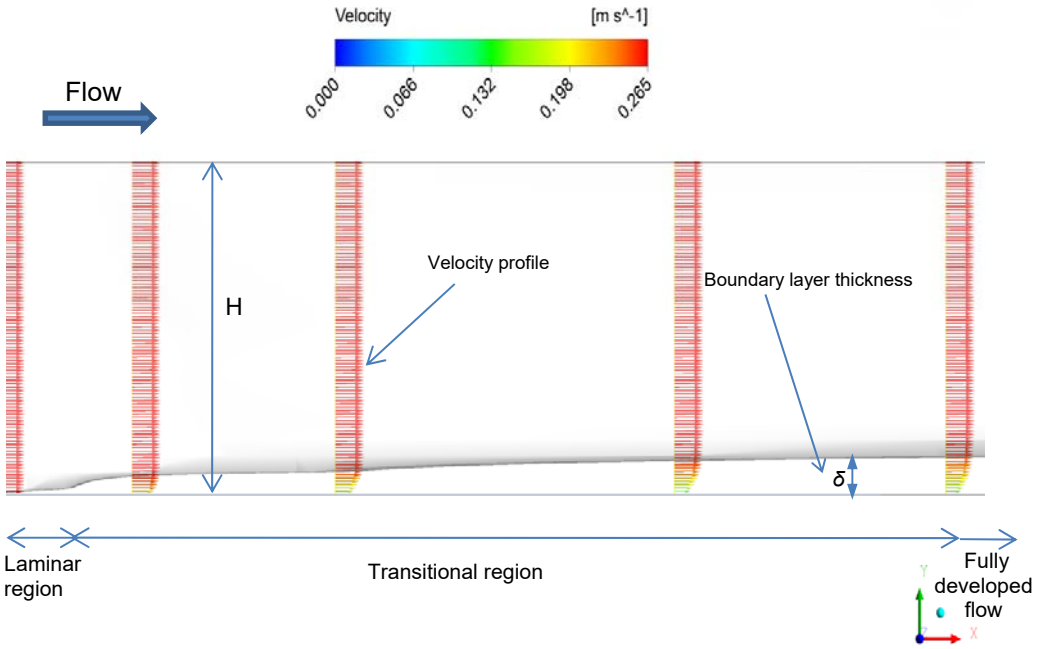

Figure 3.4: Boundary layer and fully developed flow in the precursor domain.

3.4 Computational method for the main domain

In order to add a perturbation to the fully developed mean velocity profile that is produced from the precursor domain on the inlet flow of the LES main domain, a random 2D vortex method is considered.

3.4.1 Vortex method for LES inlet condition

The vortex method (VM) based boundary condition was implemented. In this approach, a perturbation is added to a specified mean velocity profile via a fluctuating two dimensional vorticity field (two dimensional in the plane normal to the streamwise direction). The vortex method is based on the Lagrangian form of the 2D evolution equation of the vorticity and the Biot-Savart law (Batchelor, 1967).These particles or "vortex points" are embedded arbitrarily and carry information about the vorticity field. If N is the number of vortex points in Equation 3.11, then based on prior studies that have looked at a water flow in open channel (Mathey et al. (2006) and Jørgensen and Nilsson (2012)), it has been considered that the flow field can be simulated in an accurate way with vortices number at the inlet face is equal to 200. This value is already validated for turbulent flow in the open channel by. The term A represents the area of the inlet section, the amount of vorticity carried by a given particle i is represented by the circulation Γ_i and an assumed spatial distribution η:

$$\Gamma_i(x,y) = 4\sqrt{\frac{\pi A k(x,y)}{3N[2ln(3)-3ln(2)]}} \tag{3.11}$$

$$\eta(\vec{x}) = \frac{1}{2\pi\sigma^2}\left(2e^{\frac{-|x|^2}{2\sigma^2}} - 1\right)2e^{\frac{-|x|^2}{2\sigma^2}} \tag{3.12}$$

where k is the turbulence kinetic energy. The parameter σ provides control over the size of a vortex particle. The resulting discretisation for the velocity field is given by:

$$\vec{u}(\vec{x}) = \frac{1}{2\pi}\sum_{i=1}^{N}\Gamma_i\frac{((\vec{x}_i-\vec{x})\times\vec{z})(1-e^{\left|\vec{x}-\vec{x}\right|^2})}{\left|\vec{x}-\vec{x}_i\right|^2} \tag{3.13}$$

where $\vec{z}$ is the unit vector in the streamwise direction. So as to make the vortex method strategy for the most part applicable, a local vortex size is determined through a turbulent mixing length theory. σ is computed from a known profile of mean turbulence kinetic energy and mean dissipation rate at the inlet as indicated by:

$$\sigma = \frac{ck^{3/2}}{2\epsilon} \qquad 3.14$$

where $c = 0.16$. So as to guarantee that the vortex will dependably have a place with resolved scales, the minimum value of σ in Equation 3.14 is bounded by the local grid size Δ so that $\sigma \geq \Delta$.

This method has previously been applied to the case of fully developed channel flow by Mathey et al. (2006). They concluded that the vortex method provided a relatively inexpensive, yet accurate way to generate random fluctuations representing a turbulent flow field at the inlet. Figure 3.5 shows the turbulent velocity in the main domain after the vortex method used.

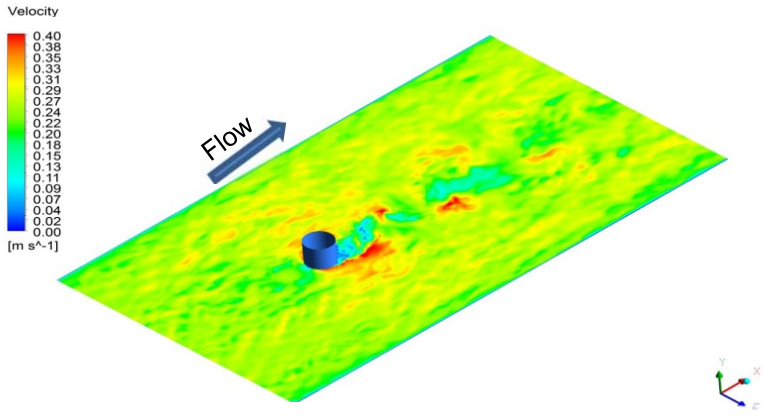

Figure 3.5: The velocity distribution in the main domain using vortex method.

3.4.2 **Solution method**

The simulations were carried out using the ANSYS Fluent CFD software. Segregated pressure solver was used to solve the spatially filtered 3D time-

dependent Navier-Stokes equations. The solver uses the SIMPLE scheme for pressure-velocity coupling and a least-squares cell-based approach for gradient evaluation. The unsteady LES employs a second-order bounded central spatial discretisation scheme along with an implicit second order time marching scheme. The time step is calculated to keep the maximum Courant–Friedrichs–Lewy (CFL) number smaller than 1.0 for the main calculation. Maximum of 20 error-reduction sub-iterations per time step was used. Simulations were run on a High Performance Computer (HPC) in parallel mode. Table 3.2 below represents the setup parameters used in the study for the turbulent flow around cylinder bridge pier using LES.

Table 3.2: CFD setup parameters

General		**Solution controls and residual monitors**	
Solver Type	Pressure-Based	**Under relaxation factor**	
Velocity Formulation	Absolute	Pressure	0.3
Time	Transient	Density	1.0
Viscous	LES	Body Force	1.0
Material		Momentum	0.7
Fluid	Water Liquid	**Convergence absolute criteria**	
Density	998.2 kg/m^3	Continuity	1x10^{-4}
Viscosity	0.001003 kg/(m. second)	x-velocity	1x10^{-4}
Solution methods		y-velocity	1x10^{-4}
Scheme	SIMPLE	z-velocity	1x10^{-4}
Spatial discretisation			
Gradient	Least Squares Cell Based		
Pressure	Standard		
Momentum	Bounded Central Differencing		
Transient Formulation	Bounded Second Order Implicit		

3.4.3 Computational grid

The LES having $12x10^6$ and $24x10^6$ grid size, the doubling of the cell account is achieved by a global reduction for the mesh size equally applied in all three directions. The grid density is varied so that the mesh is very fine in the regions containing the horseshoe vortex system, the downflow, and the near wake. The mesh in the horizontal plane around the cylinder is already shown in Figure 3.3. As the mesh contains only hexahedral cells to ensure maximum quality, the mesh is structured. For both grid sizes, the first row of cells is situated at 0.000667D away from the walls, corresponding to wall unit smaller than one, and approximately equal to 0.86. Typical computational cell dimensions in three directions inside the horseshoe vortex region, away from the walls and inside the downstream flow in the wake vortices region are 5-18 wall units. Simulations were run on a HPC with up to 64 processors.

3.5 Mean flow and turbulence statistics around the cylinder

The comparison of the LES of two different grid sizes $12x10^6$ and $24x10^6$ with time steps equal to 0.001 and 0.0008 seconds respectively is studied. Also, URANS approaches with k-ε standard and k-ω SST models with mesh size equal to $12x10^6$ and time step equal to 0.001 seconds for unsteady flow around a circular cylinder is given. The mesh independency that already carried out on these two models (k-ε standard and k-ω SST) show that there is no significant effect on the predicted results after $9x10^6$ grid size (pressure coefficient at the bed in the symmetry plane upstream of the cylinder, pressure coefficient at the stagnation point in front face of the cylinder, and the bed shear stress in the symmetry plane upstream of the cylinder); as presented in

Figure 3.6. The main objective of this section is to verify the efficacy of the LES model to simulate the complex flow around bridge pier.

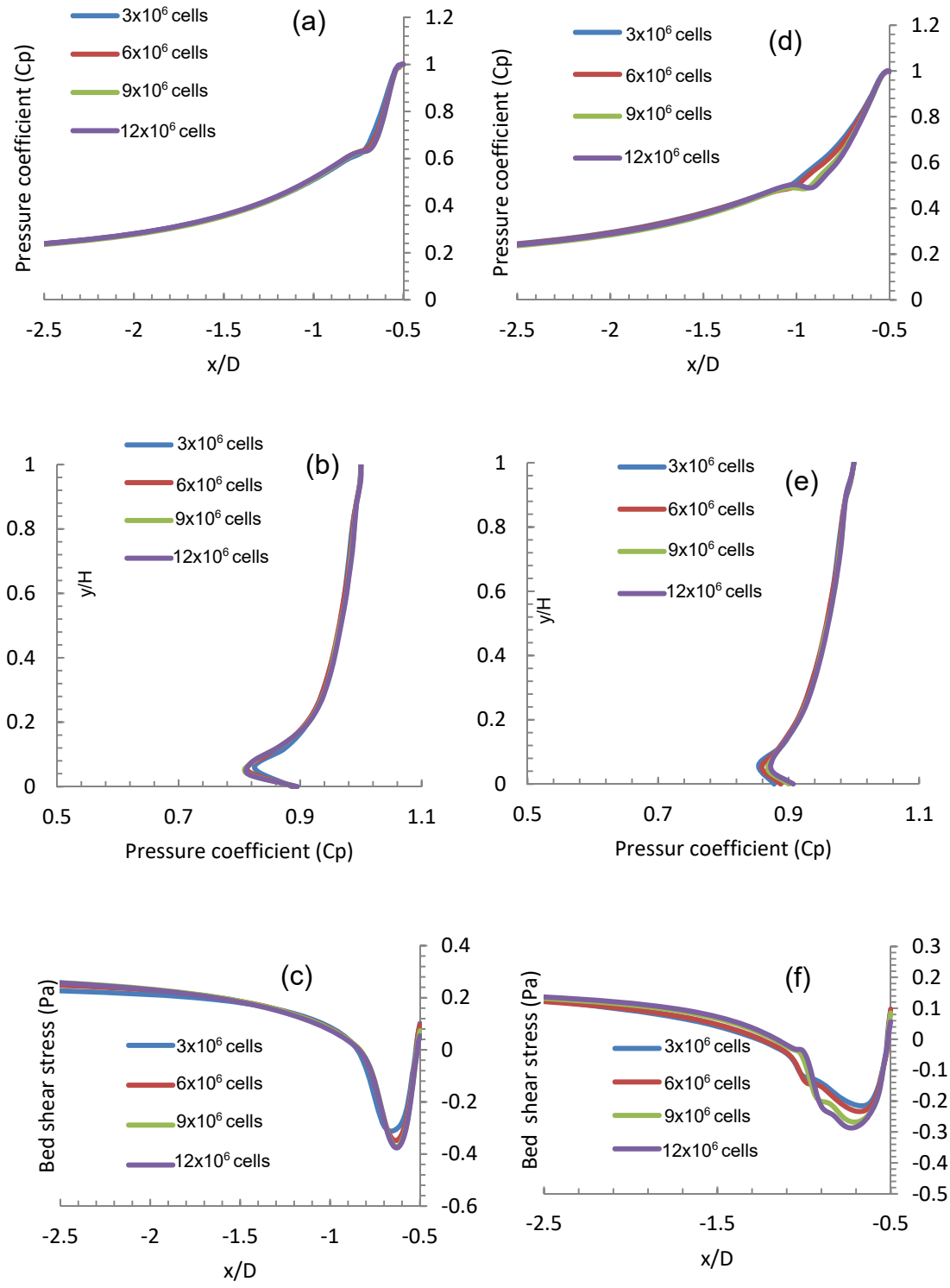

Figure 3.6:Mesh independency study for *k-ε* standard model (Figures a, b and c), and *k-ω* SST model (Figures d, e and f).

The averaging of the predicted results (i.e., velocity distribution, pressure coefficient, and wall shear stress) was started after fully developed turbulent flow has been achieved. It initially corresponds to 30,000 time steps and then carried out additionally over another 30,000 time steps to collect flow statistics. The results have been compared to the experimental results provided by Dargahi (1989). To demonstrate the flow features, profiles were produced from the simulation results along the symmetry plane upstream of the cylinder, and along lines transverse to the flow direction located at two heights from the channel bed (y/H=0.1 and y/H=0.95) and at several distances downstream of the cylinder as show in Figure 3.7.

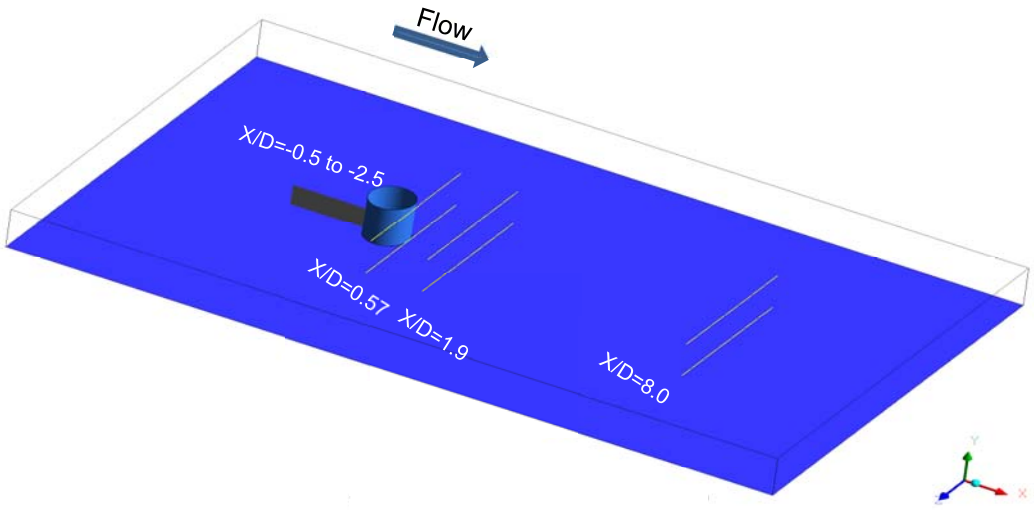

Figure 3.7: Plane and lines where profiles are compared.

3.5.1 Horseshoe vortices upstream of the cylinder

Figure 3.8 (a) shows the topology of the horseshoe vortex system described by Dargahi (1989) for the entire range of R_e (6,600 ≤ R_e ≤ 65,000), while Figure 3.8 (b) shows the modelled flow field in the symmetry plane from *k-ω* SST model. The Figure 3.8 (b) shows a clear single vortex at a distance of

-0.85 times the diameter of the cylinder from the pier centre and this is contrary to the experimental observation of Dargahi (1989). In the LES model, the horseshoe vortex system for the same R_e of Dargahi (1989) shown in Figure 3.8(c). It is clear that the horseshoe vortex system consisted of 5 major vortices in front of the pier. Two primary vortices identified as V2 and V4 located at a distance of -0.8 and -0.95 times the diameter of the cylinder from the pier centre respectively, with their respective secondary structures that emerge due to the vortex-wall interaction, called V3 and V5 which located at 0.86 and 1.06 times the diameter of the cylinder from the pier centre respectively, and a corner vortex at the base of the pier identified as V1 as described in Dargahi (1989).

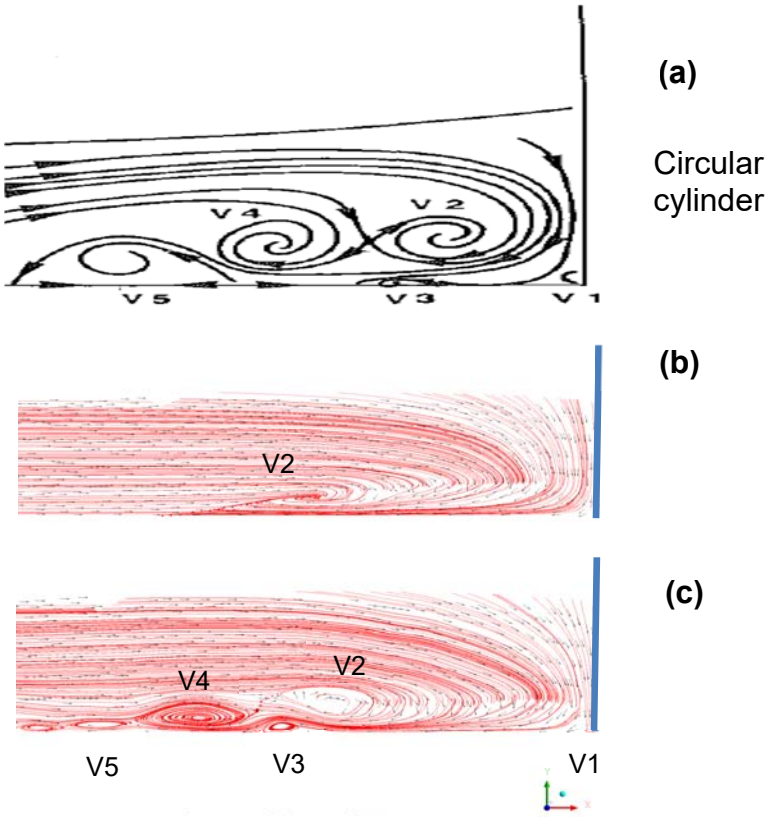

Figure 3.8: Instantaneous horseshoe vortex system at the symmetry plane in front of the cylinder (a) reported by Dargahi (1989), (b) *k-ω* SST model and (c) LES ($12x10^6$).

3.5.2 Averaged velocity profile: downstream region

In addition to the instantaneous velocity distributions computed upstream of the cylinder, the time averaged velocity profiles in the direction perpendicular to the flow downstream of the cylinder are shown in Figure 3.9. The data have been taken in two levels above the bed (y/H=0.1 and y/H=0.95) and they located at a three different distances downstream of the cylinder as shown in Figure 3.7 (X/D=0.57, X/D=1.9 and X/D=8.0). Predictions form the three different models are shown. In case of comparing the results close to the bed (y/H=0.1), the results for both LES simulations are in very close agreement in all locations. The k-ε model and k-ω SST predict well in some places and overall trends are predicted well. However, there are locations where both are marginally over and under predicting. The *k-ω* SST model in general is better than *k-ε* standard. In case of the comparing the results close to the surface (y/H=0.95) it can be seen there are a discrepancy for predict the time-averaged velocity for all modes and specially in the region close to the cylinder, this discrepancy is due to the slip wall used at the free surface.

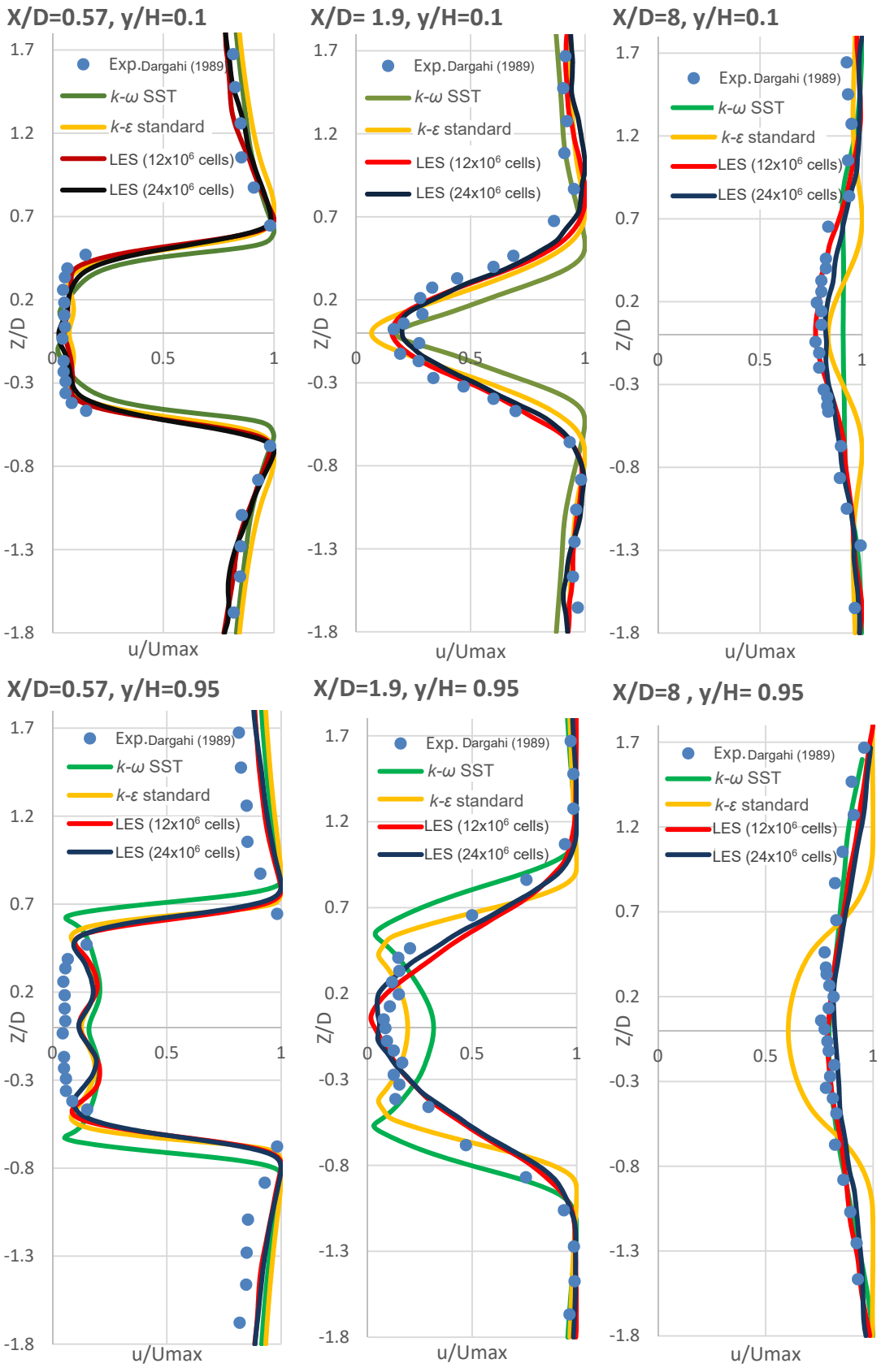

Figure 3.9: Streamwise velocity distributions downstream of a cylinder.

3.5.2.1 Vortex shedding and Strouhal number

Since considering the flow upstream of the cylinder, it is useful to evaluate the model predictions downstream of the cylinder. Flow past an obstacle can result in vortices forming and shedding in the wake region. An important evaluation of the model is to consider if the phenomena are simulated appropriately.

The Strouhal number (St) is a dimensionless parameter which describes the shedding behaviour of the vortices in the wake region of a flow:

$$St = \frac{f_s D}{u} \qquad 3.15$$

where D is the diameter of the cylinder and u is the mean velocity of the flow, f_s is the shedding frequency of the vortices equal to $1/T$, where T denotes for period of one complete vortex shedding.

The vortex shedding in the wake region of the cylinder with $R_{e\mathrm{D}}$=3.9x10^4 is discussed and evaluated by comparing the results from URANS models, and LES model with the experimental results reported by Dargahi (1989). The URANS models are both implemented using a grid size of 12x10^6 cells, whereas the LES was implemented with two grid sizes of 12x10^6 cells and 24x10^6 cells (to study the effect of grid size on the LES results). Table 3.3 presents the mean drag coefficient; C_d, the shedding frequency, f_s, and Strouhal number, St from the results of each of the turbulence model simulations so that the predicted results can be compared with the experimental data which reported by Dargahi (1989) such as (C_d=1.15, f_s=0.32Hz, St =0.185). This shows that LES model with 24x10^6 cells computes the drag coefficient, C_d is in close agreement to the measured experimental

values. However the *k-ε* model and *k-ω* SST predicted the lower values of C_d than that of in the experimental. The Strouhal number of the flow is calculated based on the shedding frequency of the lift coefficient. The time domain data of the lift coefficient is converted into the frequency domain by using Fast Fourier Transform (FFT).

The frequency of the lift coefficient, f_s, is then substituted into Equation 3.21 to get the Strouhal number. The increase in percentage (between 11% to 16%) for the visualisation prediction which is reported in Table 3.3 is due to the energy dissipation away from the peck using the FFT method, which is not very steep, as shown in Figure 3.10. The k-ε model is not able to predict any vortex shedding frequency, as expected and in agreement with Patel (2010), whereas both the LES and *k-ω* SST models are able to simulate vortex shedding.

Table 3.3: Summary of predicted drag coefficient, C_d, and downstream vortex shedding parameters for circular cylinder using FFT method and visualisation method.

Model	C_d	FFT method		Visualisation method		Difference between the two methods
		f_s (Hz)	St	f_s (Hz)	St	
k-ε-standard	0.80	-------	------	-------	------	--------
k-ω SST	0.91	0.182	0.11	0.22	0.128	14%
LES ($12x10^6$)	1.24	0.290	0.17	0.33	0.190	11%
LES ($24 x10^6$)	1.19	0.275	0.16	0.33	0.190	16%
Experimental Study by Dargahi (1989)	1.15	-------	-------	0.32	0.185	-------

Figure 3.10 shows the spectral analysis of the lift coefficient using FFT applied to predicted the flow in URANS and LES models for the flow past a

circular cylinder in Z-direction and at the free surface of the channel ($y/H = 1.0$). It can be clearly noticed that the *k-ε* model fails to predict vortex shedding, while the *k-ω* SST model slightly underestimates it for $R_{e(D)}$ of

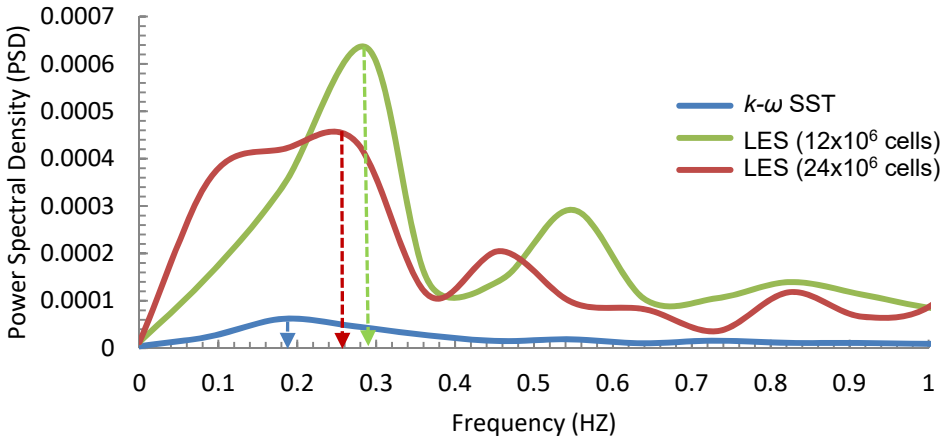

Figure 3.10: Spectral analysis of lift Coefficient.

The Strouhal number and the vortex shedding frequency are also computed through plotting streamlines of the velocity field behind the cylinder for a time series and visualising the frequency of the vortices being shed. Figure 3.11 presents the velocity magnitude streamlines in the wake region of the flow past a circular cylinder using *k-ε* standard. From monitoring the velocity distribution around the cylinder for a specific time of flow, it is clear that, there is no change in the profile with respect to time. As mentioned above, in Figure 3.11 that the *k-ε* standard is not able to capture the vortex shedding behind the cylinder.

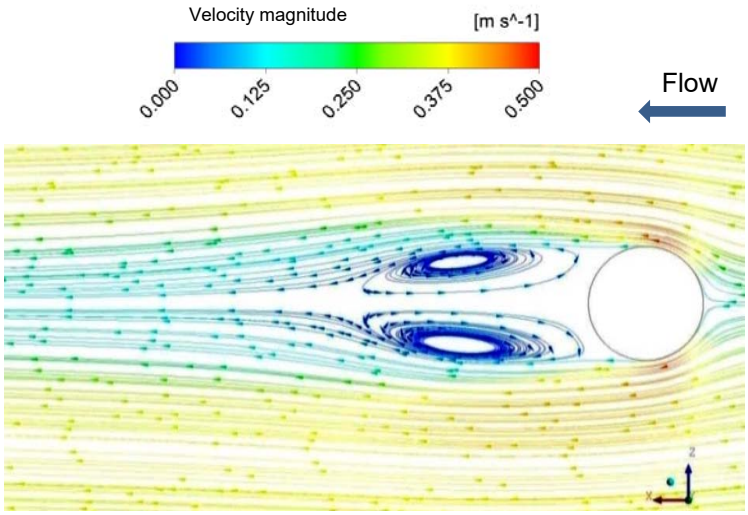

Figure 3.11: Velocity magnitude streamlines using *k-ε* standard.

Figures 3.12 and 3.13 show the velocity magnitude streamlines for the flow behind the circular cylinder for *k-ω* SST and LES (12x10^6 cells) respectively. From these two figures it can be seen that the *k-ω* SST, and LES successfully captured vortex shedding (from which frequency can be determined) downstream of the cylinder at $R_{e\mathrm{D}}$=3.9x10^4. Figure 3.12 shows the velocity magnitude streamlines behind the cylinder every 0.5 seconds of flow simulation using *k-ω* SST, it shows that the time needed for full complete one periodic vortex shedding is approximately 4.5 seconds, and that is equivalent to 0.22Hz for vortex shedding frequency, this value is closer as compared to that computed from FFT method (f_s=0.182Hz) from the experimental data (f_s=0.32Hz). But it is still under predicted. Figure 3.13 shows the velocity magnitude streamlines every 0.275 seconds in the wake region of the circular cylinder using LES (12x10^6) grid size. It shows a complete period of the one vortex shedding which needs about 3 seconds. This is equivalent to 0.33 Hz for the vortex shedding frequency, a value is very close to the experimentally vortex shedding frequency reported by Dargahi (1989). The results for case of large eddy simulation with 24x10^6 were not included because they are similar to those for case of LES with 12x10^6 grid size. By comparing the results of vortex shedding frequency produced from FFT method and visualising method, it can be seen that the f_s predicted from FFT method for both models (*k-ω* SST, and LES) is usually underestimated compared with that computed from the visualising method.

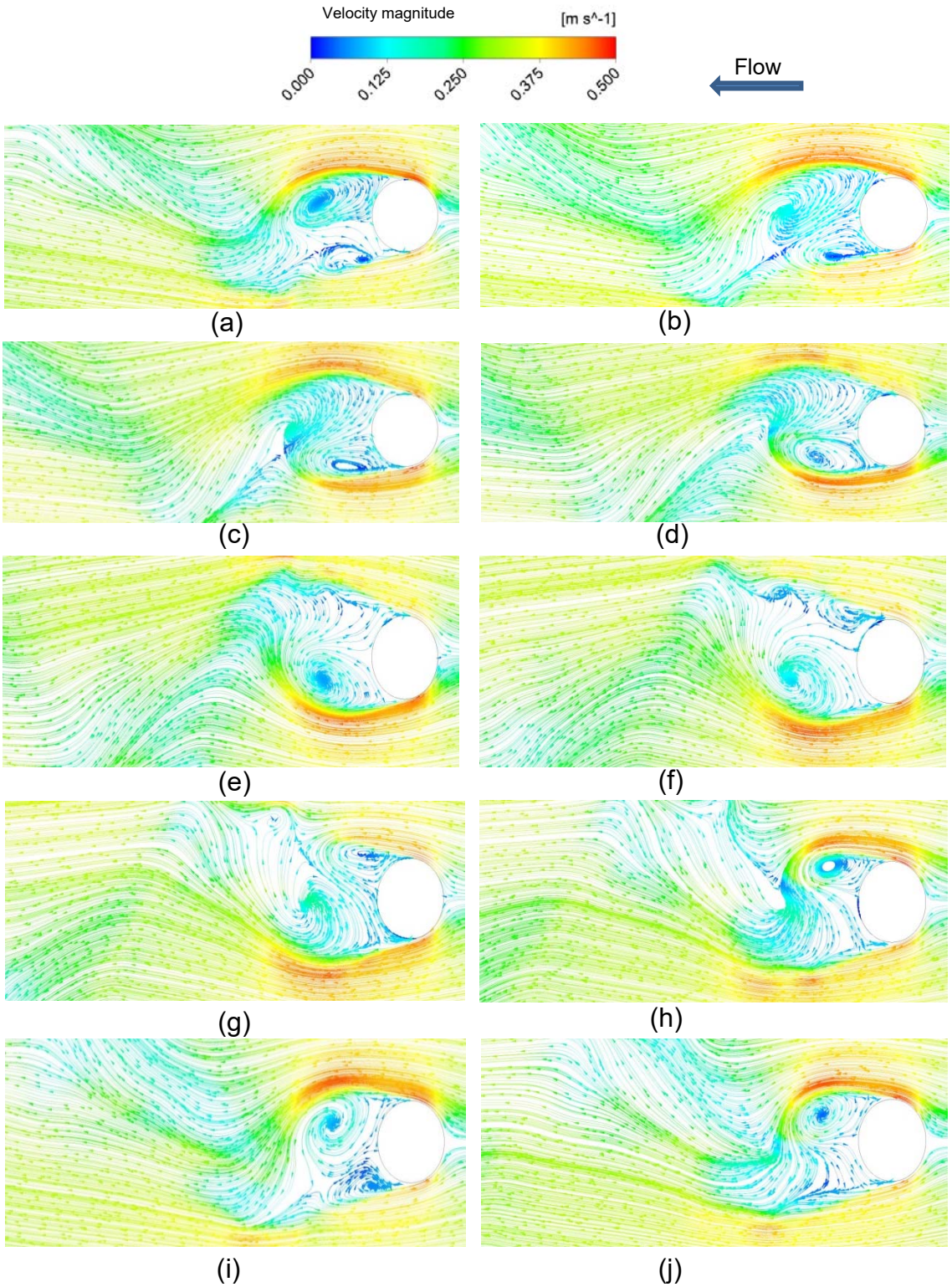

Figure 3.12: Velocity magnitude streamlines downstream of the cylinder at every 0.5 second using *k-ω* SST.

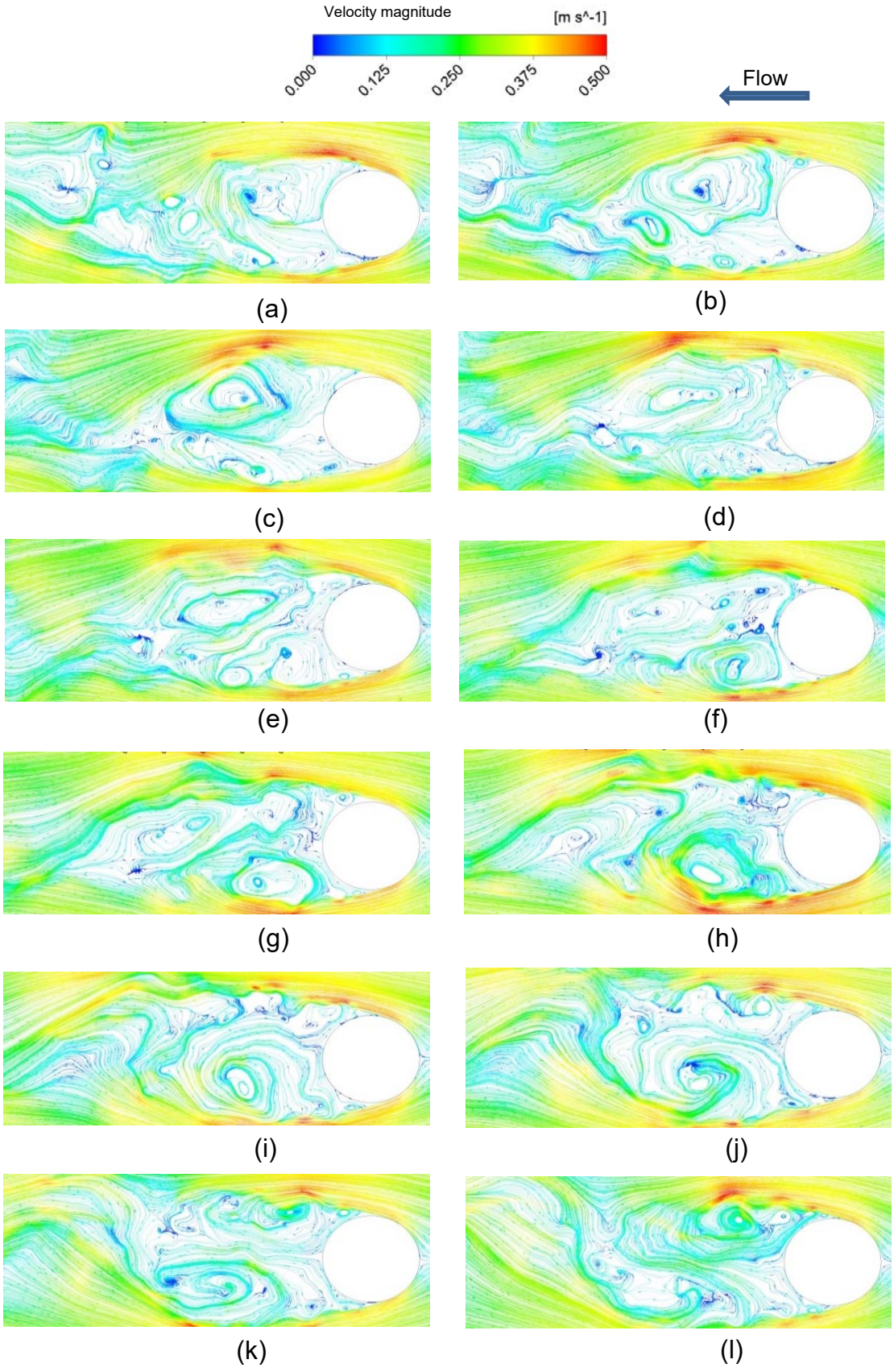

Figure 3.13: Velocity magnitude streamlines downstream of the cylinder at every 0.275 second using LES.

3.5.3 Mean pressure distributions

Figure 3.14 shows the pressures coefficient upstream of the cylinder along the line of symmetry for the three different models. Averaging of the results was initiated after 30,000 time steps to ensure that the averaged quantities are smooth, corresponding to three flow through times. Then the simulation carried out additionally over another 30,000 time steps to collect flow statistics. All models are broadly in good agreement, but it can be seen that the LES (with both $12x10^6$ and $24x10^6$ grid sizes) marginally closer predicted results are observed with respect to the experimental results and when compared with other URANS models.

In LES, the pressure coefficient at the symmetry plane increases slowly at a constant rate and then the rate of increase starts to decrease at X/D = -1.0 and -1.1 for grid size equal to $12x10^6$ and $24x10^6$ respectively. From Figure 3.8, it can be seen, its due to the impact of horseshoe vortices predicted in this region by LES. This behaviour profile of the pressure coefficient agrees well with the experimental measurements by Dargahi (1989), since the deviation of experimental values starts at about X/D = -0.86, as shown in the figure below.

The LES model described, with both grid sizes, shows a slightly early separation of the flow when compared to the experiment, inducing the vortex to be found further upstream of the cylinder than measured. A similar discrepancy was also observed with an eddy-resolving numerical model based upon the DES by Escauriaza (2008), and URANS models for this flow with *k-ω* turbulence model in the studies of Tao (2013) and Roulund et al. (2005).

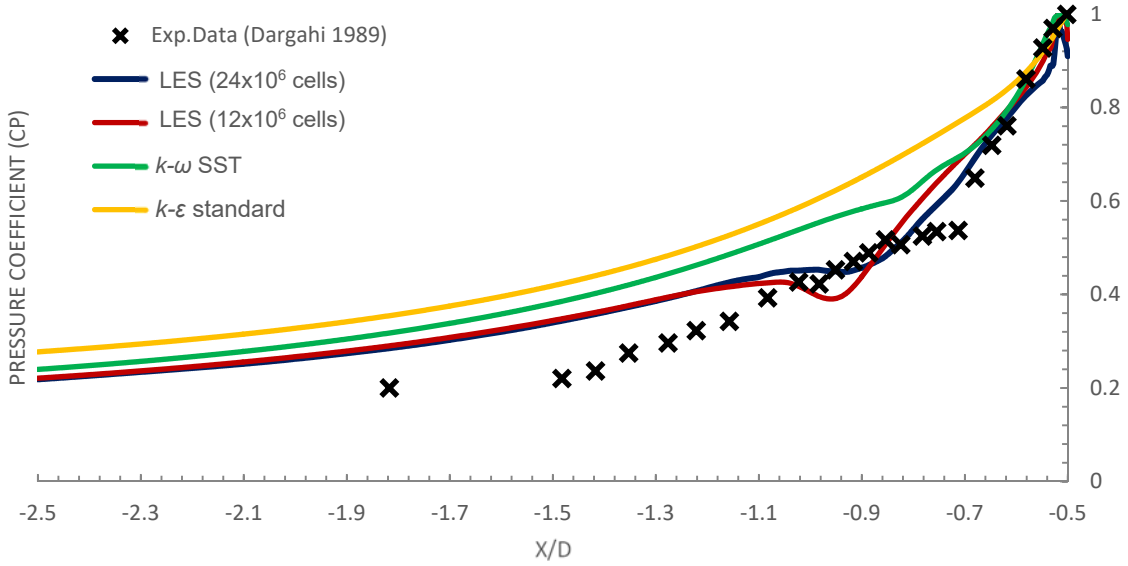

Figure 3.14: Pressure coefficient along the line of symmetry upstream of a cylinder.

The pressure distribution along the vertical face of the cylinder is considered in Figure 3.15. The vertical profile of the pressure distribution for the LES with the finest grid size is very similar to the experimental measurement with the minimum pressure at approximately y/H = 0.075, with $C_p \sim 0.65$, whereas the lowest accuracy in capturing the minimum pressure with *k-ε* was found at approximately y/H = 0.05 with $C_p \sim 0.57$, as shown in Figure 3.15.

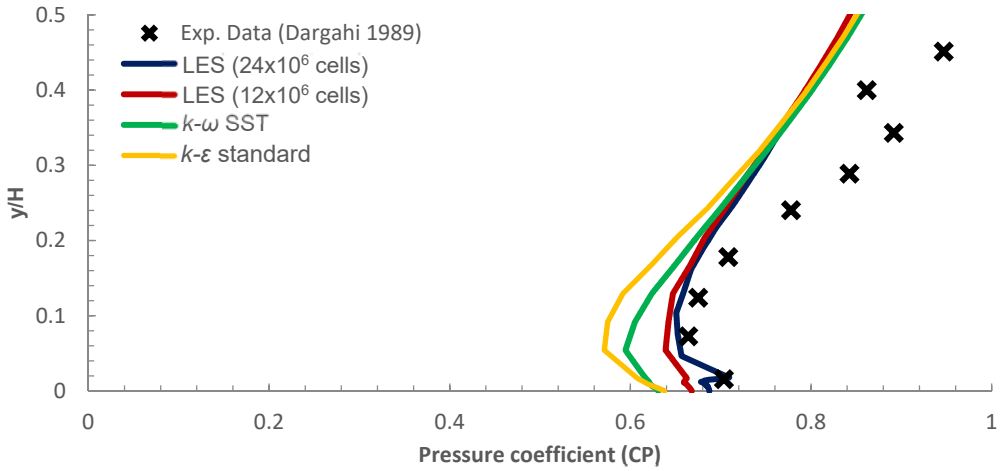

Figure 3.15: Pressure coefficient along the stagnation line at the upstream of a cylinder.

When the flow approaches the cylinder, the water level in the region upstream of the cylinder starts to increase until it reaches the maximum at the pier front face. This is due to the fact that the approaching flow decelerates and the flow separation occurs in the horizontal and vertical planes and an adverse pressure gradient develops. In the wake region, downstream of the cylinder, the pressure decreases due to strong vortices and therefore, the water level decreases. In the region away from the cylinder the influence of the pier on the water level gradually disappeared.

Upstream of the cylinder, the pressure coefficient is positive, indicating a pressure rise and water level increase. Downstream of the cylinder, in the wake region, a negative pressure coefficient indicates a pressure drop and a decrease in water level; as shown in Figure 3.16 the distribution of the pressure coefficient at the free surface of the channel with circular cylinder bridge pier. The pressure coefficient C_p calculated using Equation 3.22:

$$C_p = \frac{(p-p_0)}{(0.5\rho U^2)} \qquad 3.16$$

where p is the local pressure at a point along the flow direction; p_0 upstream static pressure; and U upstream approaching flow velocity.

Figure 3.16 shows a comparison between the experimental pressure coefficient at the free surface resulted from Dargahi (1987) and different CFD models in this study, for a flow around circular cylinder. It is clearly seen that the LES with both grid size gives a good accuracy with the experimental data and when comparing with other URANS models.

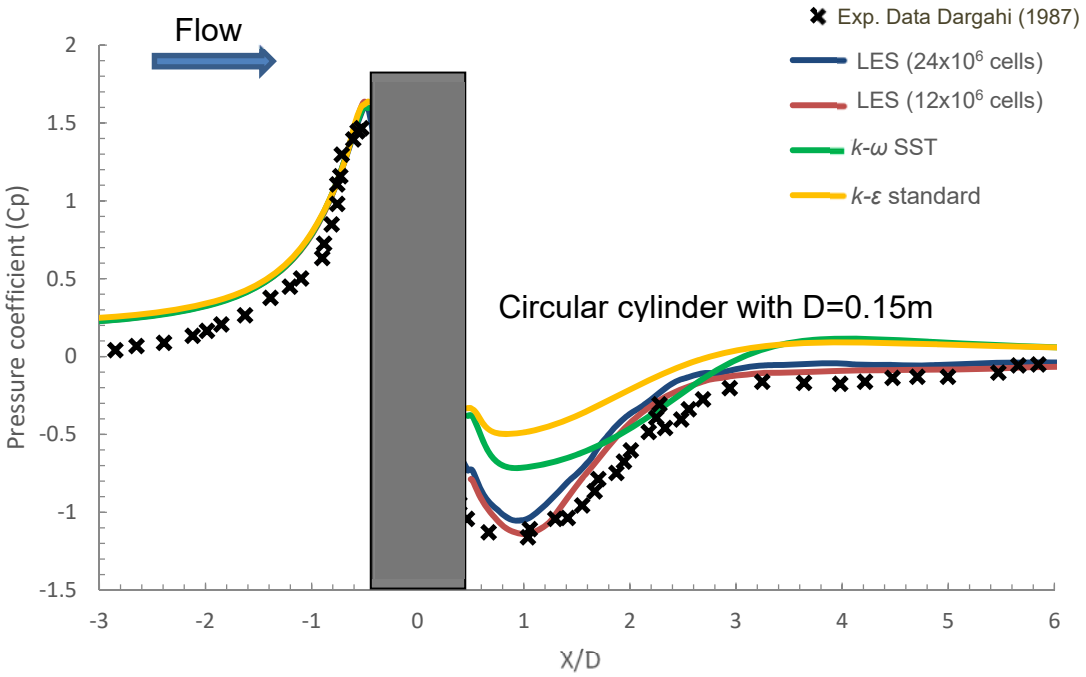

Figure 3.16: Pressure coefficient at the free surface and along the line of symmetry.

3.5.4 Bed shear stress

A comparison is made of the bed shear stress for each of the models in Figure 3.17. The results are normalised with the mean shear stress at a point located at X/D=-2.5 from the cylinder. The shear stresses are reduced as the cylinder is approached. In general, all the models show good agreement with the experimental data. To study the amplification factor of the bed shear stress in the horseshoe vortex region with respect to the undistributed shear stress, the LES simulation with both grid sizes and *k-ω* SST model appears to give a reasonable agreement with respect to the experimental value, which is equal to 1.5, as shown in the figure.

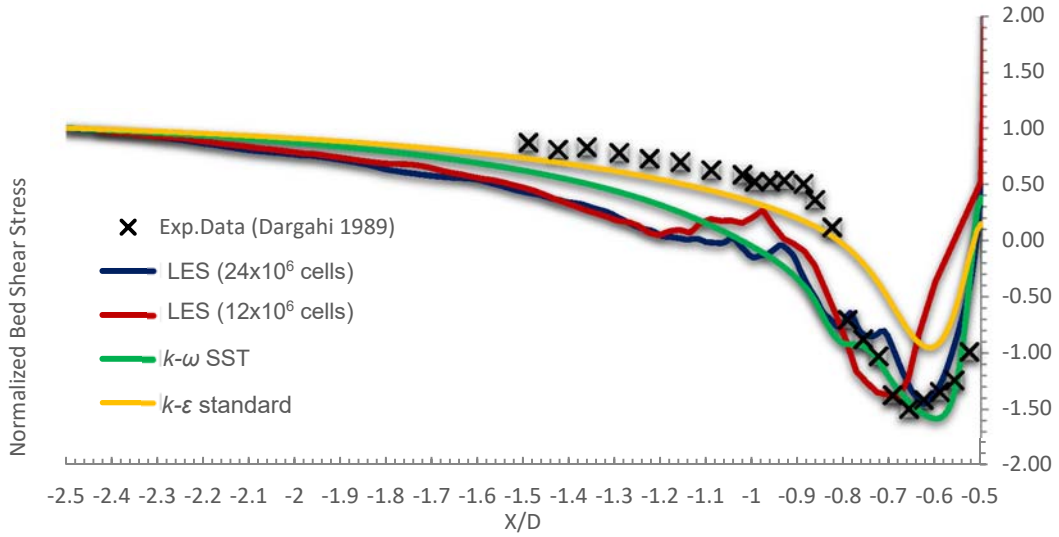

Figure 3.17: Mean bed shear stresses along the line of symmetry upstream of a cylinder.

3.5.5 Energy spectral density

The distribution of the turbulent kinetic energy as a function of different frequency scales, is described by the energy spectrum density (ESD), this is shown below in Figure 3.18. The figure shows that the energy transfer from large to small eddies are achieved by inertial forces as demonstrated by the $k^{-5/3}$ proportionality of the energy spectra E(k) in this inertial range. Figure 3.18 shows the energy dissipation for LES model with $12x10^6$ and $24x10^6$ grid size respectively. The data have been collected at points located at a distance (X/D=1.0) upstream of the cylinder and elevated at $y/H = 0.0025$, 0.25 and 0.5 away from the bottom wall. It is clear from Figure 3.18 that the efficiency of the simulation with LES for both grid sizes to transfer the energy from large to small eddies.

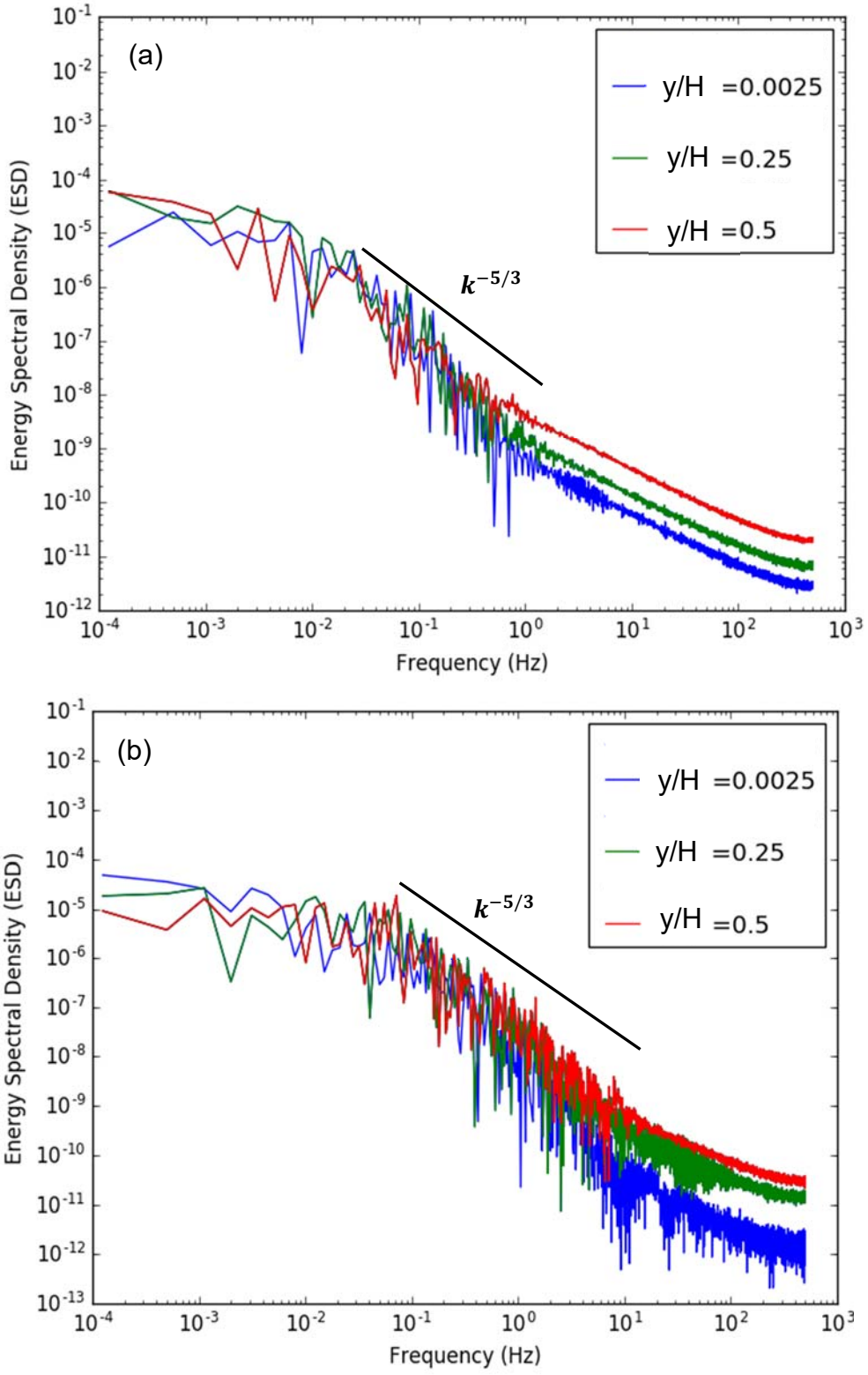

Figure 3.18: The energy spectrum density (ESD) (a) LES model with $12x10^6$ cells and (b) LES model with $24x10^6$ cells.

3.5.6 Three-dimensional dynamics of the horseshoe vortex and scour mechanisms

To understand the complex instability mechanism that occurs upstream of the cylinder the 3D dynamics of the vortices is studied. The 3D coherent dynamics of the horseshoe vortex system is identified using the Q criterion. This is considered as an effective vortex indicator in wall turbulence and it helps to visualise the instantaneous resolved flow fields and study the resulting coherent structures of the horseshoe vortex system around the cylindrical pier.

The Q criterion is used to visualise the vortices, where Q is the second invariant of the velocity gradient tensor with dimension of (s^{-2}).

$$Q = C_Q(\Omega^2 - S^2) \quad 3.17$$

where the constant $C_Q = 0.25$ in ANSYS CFD-Post. In this definition, S is the absolute value of the Strain Rate, and Ω is the absolute value of vorticity, and as shown below:

$$S = \sqrt{2S_{ij}S_{ij}} \quad 3.18$$

$$\Omega = \sqrt{2\omega_{ij}\omega_{ij}} \quad 3.19$$

$$S_{ij} = \frac{1}{2}\left(\frac{\partial U_i}{\partial x_j} + \frac{\partial U_j}{\partial x_i}\right) \quad 3.20$$

$$\omega_{ij} = \frac{1}{2}\left(\frac{\partial U_i}{\partial x_j} - \frac{\partial U_j}{\partial x_i}\right) \quad 3.21$$

The reason behind this definition is to quantify vortices without mean shear rate in order to avoid displaying the steady shear layer (where,$S = \Omega = 1/2\left|\frac{du}{dy}\right|$) (Menter, 2012).

The instantaneous vortices shown in Figure 3.19 reveal the 3D features of the horseshoe vortex with a disorganized thinner vortex closer to the cylinder

and a well-organised thicker upstream vortex that has grown from the separation region. These two vortical structures correspond to the vortices V2 and V4 respectively. In addition to these two primary vortex , there are secondary structures that emerge due to the vortex-wall interaction, called V3 and V5, and a corner vortex at the base of the pier identified as V1, that were initially indicated on the figure shown in Figure 3.8(c) for the symmetry plane. By studying the transient behaviour for 30 seconds time flow, it can be observed that that the V2, and V1 are the most stable vortices around the cylinder compared with the other vortices (V3, V4 and V5) which are found upstream of the main vortex V2. In addition to the horseshoe vortex system upstream of the cylinder, the wake region downstream of the cylinder is also populated with vortices.

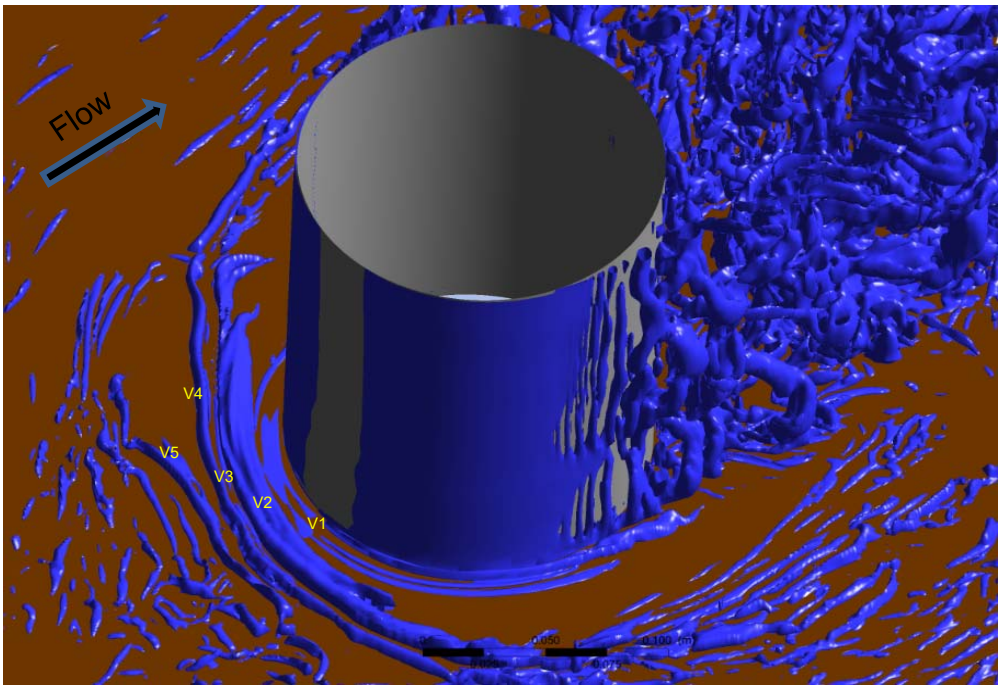

Figure 3.19: Visualisation of the instantaneous 3D coherent structures around the cylinder using LES ($12x10^6$ cells).

3.6 Summary and findings

In this chapter, an eddy-resolving numerical model based upon the LES approach has been implemented for predicting the 3D flow around a circular bridge pier, mounted on a flatbed, with $R_{e\mathrm{D}}$=3.9×10^4. The experimental configuration by Dargahi (1989), was used for validation of the numerical results. Other validation data from the literature were used as well such as Dargahi (1987). To study the effect of grid size on the LES, two grid densities were used (12x10^6 and 24x10^6). The predicted LES results were compared with URANS models (i.e., *k-ε* standard and *k-ω* SST), and with the experimental data. It verifies the reliability and feasibility of the LES to simulate the turbulent flow around obstacles mounted in a flatbed, given as:

- LES model can capture all the horseshoe vortices upstream of the cylinder that observed in Dargahi (1989). In contrast to the URANS models which show a single vortex at a distance of 0.85D from the front face of the cylinder. These horseshoe vortices consisting of two primary vortices identified as V2 and V4 located at a distance of 0.8D and 0.95D from the pier centre respectively, with their respective secondary structures that emerge due to the vortex-wall interaction, called V3 and V5 which located at 0.86D and 1.06D from the pier centre respectively, and a corner vortex at the base of the pier identified as V1. By studying the transient behaviour for the horseshoe vortex system, it can be observed that V2 and V1 are the most stable vortices around the cylinder compared with the other

vortices (V3, V4, and V5) which are found upstream of the main vortex V2.

- In case of comparing the time-averaged flow around the circular cylinder such as velocity distribution profile downstream of the cylinder, the bed pressure coefficient, and the bed shear stress, all the models are in reasonable agreement with the experiments. However, it can be clearly observed that the LES predictions are in the closest agreement with the experiments.
- Furthermore, the LES ($12x10^6$, $24x10^6$ grid size) predicts the vortex shedding in the wake of the cylinder, with a main frequency (and a corresponding Strouhal number 0.19) that is very close to the value reported by (Dargahi, 1989), which is equal to (0.1846). The mean drag coefficient for the entire pier is 1.19, and 1.24 for $12x10^6$, and $24x10^6$ grid size respectively. Although these values are somewhat higher than the value (1.15) derived from Dargahi (1989), it still predicts a very good estimation compared with URANS models such as k-ε standard (C_d=0.8) and k-ω SST (C_d =0.91) models.
- The energy spectrum density investigation has been undertaken for different points located close to the cylinder and at a different distance from the riverbed. It indicates that the accuracy of the simulation with respects to LES can transfer the energy from large eddies to small.

Chapter 4

Circular Cylinder Bridge Pier- Scour Development Using a Dynamic Mesh Updating Technique

In this chapter the LES approach is adopted alongside a dynamic meshing technique to enable the simulation of scouring around a bridge pier. The updating dynamic mesh technique allows an approach that can numerically describe complex 3D scour behaviour around bridge piers through coupling the changes in topography with the local detailed hydrodynamics. By redeveloping a commercial CFD code using user-defined functions (UDF) written in C^{++}, the bed shear stress can be computed using the LES turbulence model at each time step and stored such that the shear stress can be incorporated as a key parameter to control the sediment motion in the scour process. The dynamic mesh updating technique is implemented to move the bed and assures a practical and accurate scour simulation by individually updating the domain's nodes of the riverbed at each time step.

The outline of this chapter is as follows. In Section 4.1, a short description of the equations used to simulate the inception motion of sediment, and the sediment transport rate are given. In Section 4.2, updating mesh strategy used in this study and, the necessary macros used to compute the bed shear stress, and the moving mesh in the UDF have been described. The issue involved in using the dynamic mesh technique in a parallel solver and how to reduce it is

discussed in Section 4.3. Section 4.4 describes the simulation of scour around circular bridge pier using the methodology proposed in this thesis. Furthermore, a comparison of the predicted results with the experimental data by Dargahi (1990), and numerical study by Escauriaza and Sotiropoulos (2011) Escauriaza and Sotiropoulos (2011) is presented. In Section 4.5 the horseshoe vortex system during scour evolution has been investigated, and the bimodal phenomena of the horseshoe vortex system using a probability density function.

4.1 Sediment transport modelling

In addition to the hydrodynamic flow behaviour (described in Chapter 3), the sediment transportation is considered a significant parameter that should be precisely modelled in a scour simulation. The scouring depth and sediment transport rate depend to a great extent on the energy and size of the horseshoe vortex which moves and interacts with the hole created by the scour evolution. As such, using the LES in a CFD model to investigate the horseshoe vortex near to the bridge piers enables an accurate representation and prediction of the depth and shape of the hole that develops during the scour process.

The sediment transport is considered to occur immediately when the bed shear stress, (which was already calculated from the LES), exceeds the critical shear stress of the sediment particle, (this is called the incipient motion of sediment) (Chien, 1999). After the incipient motion, the sediment transport rate becomes another key criterion to quantitatively describe the development and level of scour in real time. Therefore, the incipient motion of sediment and

sediment transport rate must firstly be measured as they are two key parameters that determine the quality of any sediment transport model.

4.1.1 Incipient motion of sediment

A widely used procedure to determine the incipient motion for non-cohesive particles is represented by the Shields curve (Shields, 1936), which is based on the results of numerous laboratory measurements with different grain sizes, densities and wall shear stresses. The most commonly used method to predict the sediment inception is based on the excess critical shear stress (Simões, 2014, Van Rijn, 1984). The critical shear stress of sediment proposed by Shields (1936) is defined by:

$$\tau_{b.cr} = g(\rho_s - \rho)d_{50}\theta_{cr} \quad 4.1$$

$\tau_{b.cr}$ = critical shear stress of sediment; ρ = sediment particle density; ρ_s = sediment material density; d_{50} = median diameter of sediment particle; and θ_{cr}= critical Shields number (dimensionless), which is determined by:

$$\theta_{cr} = \begin{cases} 0.24D_*^{-1} & ,D_* \leq 4 \\ 0.14D_*^{-0.64} & ,4 < D_* \leq 10 \\ 0.24D_*^{-0.10} & ,10 < D_* \leq 20 \\ 0.013D_*^{0.29} & ,20 < D_* \leq 150 \\ 0.055 & ,150 < D_* \end{cases} \quad 4.2$$

where $D_* = d_{50}[(s-1)g/\vartheta^2]^{1/3}$; and ϑ = kinematic viscosity coefficient; s = relative density of the sediment particle. In reality the riverbed is not always flat despite Equation 4.1 being designed for flat riverbed. The formula of dimensionless critical shear stress, as shown in Equation 4.3

$$T = (\tau_b - \tau_{b.cr})/\tau_{b.cr} \quad 4.3$$

where T = dimensionless critical shear stress; and τ_b = shear stress of sediment. Once τ_b becomes greater that $\tau_{b.cr}$, the triggering removal value in the current sediment transport modelling, the incipient motion of sediment can take place immediately.

4.1.2 Rate of sediment transport

After the sediment movement begins, the sediment transport rate becomes another key parameter that describes the scour process. The sediment transport rate is characterised as the movement of solid particles, both particulate and dissolved, that goes over a given stream transverse cross section of a given flow in a unit time, and its calculation can be given by Van Rijn (1986):

$$\frac{dh}{dt} = -0.00033\,\rho_s(\Delta g d_{50})^{0.5}\,\frac{D_*^{0.3}}{1-n}\,T^{1.5} \qquad 4.4$$

In which h = riverbed elevation; t = time; n = void ratio of sediment (which is set as 0.4 based on (Yanmaz and Altinbilek, 1991, Melville, 1997)); $\Delta = (\rho_s - \rho)/\rho$ = relative density; and T should be obtained from Equation 4.3. This equation only compute the erosion of the sediment around the bridge pier (there is no sediment deposition has been noticed around the cylinder).

By programming Equation 4.4 in computer language such as C^{++} and embedding it in the CFD code (ANSYS Fluent) as a UDF, the bed of the river can be updated according to the calculated shear based on the riverbed elevation (h) for each time step of the scour simulation. This way the transient variations of the riverbed elevation can be technically accounted for in real time using the CFD simulation.

4.2 Updating the mesh dynamically

Updating the computational grid dynamically (also known generically as dynamic meshing) indicates that the computational grid changes dynamically as the CFD simulation progresses. By implementing this updating technique in the scour simulation around the bridge pier, every cell of flow field boundary (such as the bed of the river) can be separately updated at each time step, rather than following a hypothetically changing pattern, such as virtual immersed boundary. This dynamic mesh updating technique avoids the disadvantage of predetermining the scour development pattern, and therefore should provide a more accurate representation of how the scour process proceeds over time.

4.2.1 Mesh updating strategy

As mentioned above, updating the dynamic mesh is technically executed by the user-defined functions, which allows to add the necessary functionality to problem of interest. Specifically in this implementation the UDF macro DEFINE_GRID_MOTION is created to control node movements on the riverbed boundary, another macro used to compute the dimensionless critical shear stress of each cell at the bottom wall of the channel is NV_MAG (f, t, SV_WALL_SHEAR). Equation 4.4 is used in the UDF to calculate the accumulative variation of the riverbed elevation (bottom wall) for each individual cell at each time step. The dynamic mesh updating strategy proposed in this study is primarily based upon the spring-based smoothing method, which was found to be the most compatible moving mesh strategy in conjunction with bounded second-order implicit transient formulation that was used in

performing the time-dependent computation in LES. The smoothing is used to regulate the mesh of the domain during the moving and deforming of the boundaries. In the smoothing method the interior nodes of the mesh move, but the number of the nodes and their connectivity does not change. Thus, the interior nodes absorb the movement of the boundary. For the spring-based smoothing method, the edges between any two mesh cells are idealised as a network of interconnected springs. The initial spacing of the edges before any boundary motion forms the equilibrium state of the mesh. A displacement at a given boundary node will generate a force proportional to the displacement along all the springs connected to the node. Using Hooke's law, the force on a mesh node can be written as:

$$\vec{F}_i = \sum_j^{n_i} k_{ij}(\Delta\vec{x}_j - \Delta\vec{x}_i) \quad 4.5$$

where $\Delta\vec{x}_i$ and $\Delta\vec{x}_j$ are the displacements of node i and its neighbour j, n_i is the number of neighboring nodes connected to node i, and k_{ij} is the spring constant (or stiffness) between node i and its neighbour j. The spring constant for the edge connecting nodes i and j is defined as:

$$k_{ij} = \frac{k_{fac}}{\sqrt{|\vec{x}_i - \vec{x}_j|}} \quad 4.6$$

where k_{fac} is the value for Spring Constant Factor, which is between 0 and 1.0. A value of 0 indicates that there is no damping on the springs, and boundary node displacements have more influence on the motion of the interior nodes. A value of 1.0 imposes the default level of damping on the interior node displacements as determined by solving Equation 4.7. This study uses the default value for k_{fac} =1.0.

At equilibrium, the net force on a node due to all the springs connected to the node must be 0. This condition results in an iterative equation:

$$\Delta\bar{x}_i^{m+1} = \frac{\sum_j^{n_i} k_{ij}\,\Delta\bar{x}_i^m}{\sum_j^{n_i} k_{ij}} \qquad 4.7$$

where m is the iteration number. Since displacements are known at the boundaries (after boundary node positions have been updated), Equation 4.7 is solved using a Jacobi sweep on all interior nodes. At convergence, the positions are updated such that:

$$\bar{x}_i^{n+1} = \Delta\bar{x}_i^n + \Delta\bar{x}_i^{converged} \qquad 4.8$$

where $n+1$ and n are used to denote the positions at the next time step and the current time step, respectively. This mesh updating strategy is appropriate for the scour simulation and model generation in the present study.

4.3 Dynamic mesh in parallel mode

The optimal partition (splitting of the computational mesh into linked domains – one for each computer processor) is created depending on both the problem and computer used for the simulation. To partition the given problem into “n” sub-problems with approximately the same of number of cells for each sub-problem a technique known as “load balancing” was used. This technique at the same time reduced the amount of communication between the processors i.e. so that the length of the boundary lines between the partitions is minimised.

The issue of using partitioning become significant when dynamic mesh in ANSYS Fluent with multiple versions (V14.5, V15.0 and V17.0) was used to simulate scour evolution around bridge pier. The dynamic mesh simply updates

the bed movement around the cylinder. Simulations worked fine in serial (one processor) cases, but for parallel execution, the mesh was seen to be moving in a strange way in between the processor boundary. Figure 4.1a shows the top view of the computational domain considered in this study (for more details see Section 3.2 in the Chapter 3) after it was divided into equal 8 mesh size partitions using METIS method. Figure 4.1b shows the time dependent moving mesh in Y-axis of the domain due to scour around the bridge pier. The location where the unphysical movement of the mesh occurs is precisely between the domains (partitions) for processors as shown in Figure 4.1b. A closer look into the problem revealed that the mesh at the processor boundary does not move at all, as illustrated in Figure 4.1c. The issue identified was that nodes which located in the partition lines between two adjacent domains were not moving correctly.

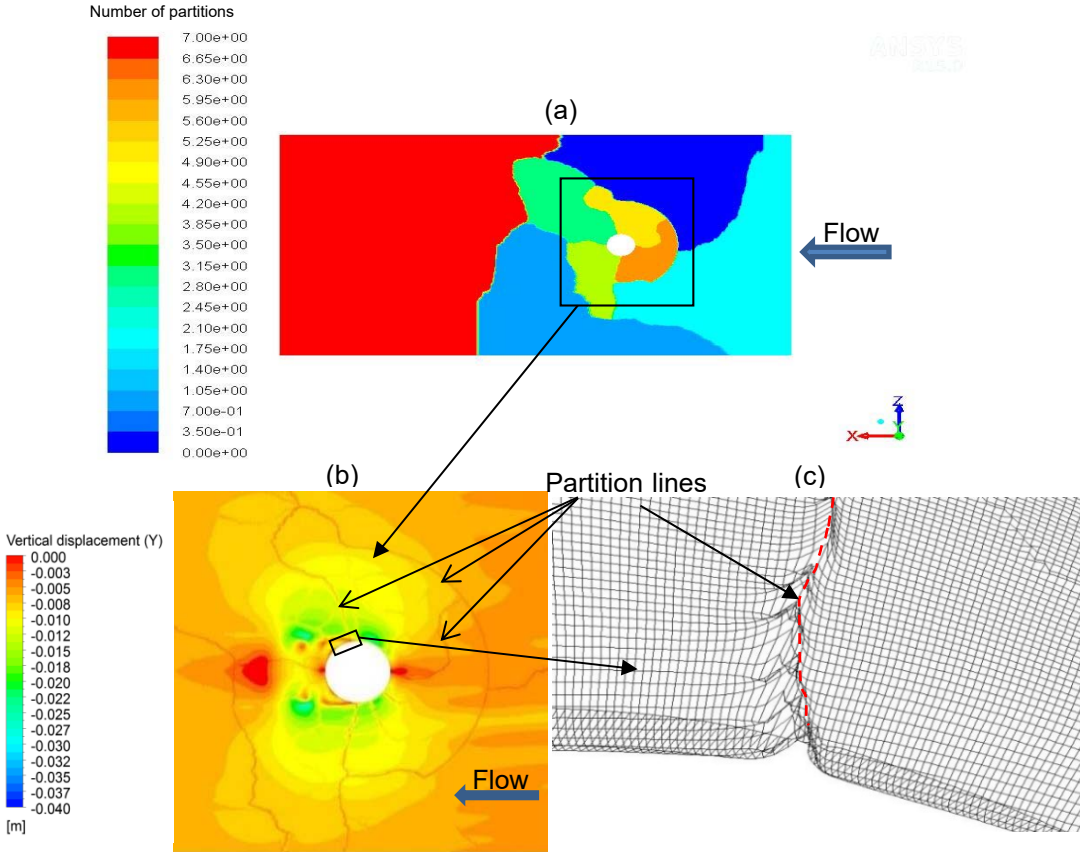

Figure 4.1: The dynamic mesh problem before solving the issue (a) Top view to the domain that divided to 8 partitions using METIS method, (b) Moving mesh in the Y-axis, (c) Nodes on the partition lines.

A number of different approaches were implemented to attempt to resolve the issue described such as adding some macros to the parallel UDF (e.g. [if Principle_face(f,t)] to stop boundary faces been looped twice (by adjacent partition nodes)), implementation of an output file, logging x, y, shear variable plus magnitude of displacement vector to flag up if computations says 0 displacement at any point.

4.3.1 Solving the problem

After several studies and attempts to solve the problem, a successful solution was identified. A method to move the mesh on the bottom bed in a way that avoided the effects of the partition boundary lines is suggested. Although this method is not the optimum for parallelisation (it slows the simulation by about 10-15%). However, it allows all mesh nodes to move depending on the UDF file embedded into simulation. Given steps had to use to solve the problem:

1) Adapt the region by choosing zone of interest, in this study the scour region around the cylinder will be considered as the zone of interest (i.e. zone 1 in Figure 4.2(a)).
2) Separate the domain to two zones (Zone 1, and Zone 2 in Figure 4.2(a)). Each zone has different IDs.
3) Partition the domain depending on the number of processors to be used (i.e. 64 partitions in Figure 4.2(a)).
4) Choose the zone of interest (zone 1) with registered partition ID=0 (this step makes the zone of interest work as one body without any partition as shown in the Figures 4.2.

5) Deactivate the load and adapt balance to avoid rearrangement of the partitions inside the zone of interest after several time steps.

6) In the UDF file write the ID of the zone of interest to specify the dynamic mesh inside it.

As shown in Figure 4.2 (b and c) there is no effect on the partition lines on the moving mesh in the Y-axis, and the scour shape around the cylinder is more reliable compared with that in Figure 4.1(b).

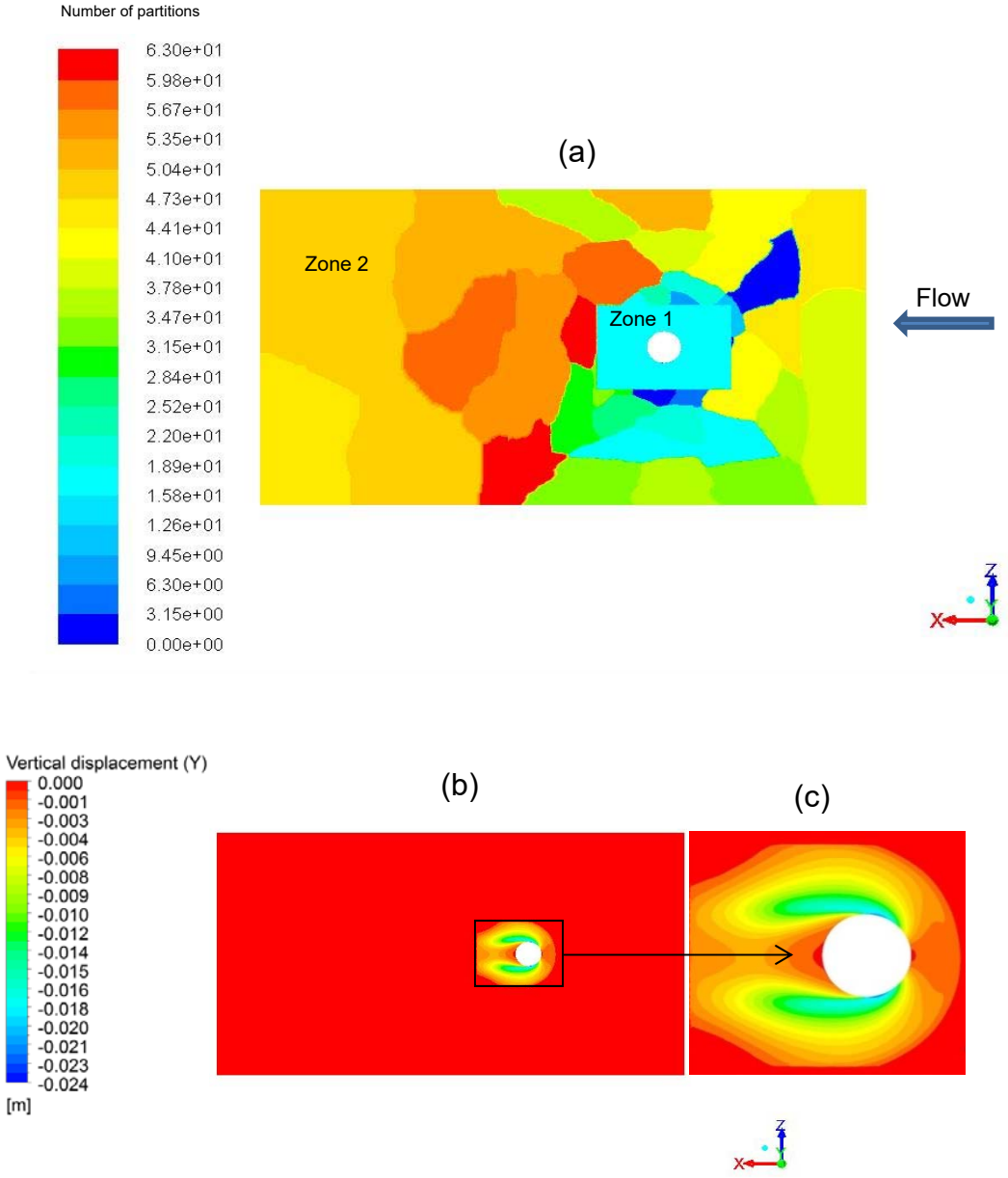

Figure 4.2: The dynamic mesh problem after solving the issue (a) Top view to the domain that divided to 64 partitions using METIS method, (b) Moving mesh in the Y-axis, (c) Zoom for the region of interest.

4.4 Simulation of scour

The dynamic mesh technique described in this study combined with an accurate simulation of the river hydrodynamic such as the LES constitutes an accurate and flexible approach to predict the scour shape around bridge pier. In this section the results of the simulation of the flow and initial scour around the cylindrical pier are presented. The simulation starts from the flatbed condition with a statistically converged flow field solution obtained as discussed in Chapter 3. The results of the simulation are compared with the experimental observations of Dargahi (1990) for flow with the same Reynolds number ($R_{e\mathrm{D}}$= 3.9×10^4) and numerical studies from (Kirkil et al., 2008, Escauriaza and Sotiropoulos, 2011). The experimental investigation of Dargahi (1990) provides a good description of the initial stages of scour process related to the unsteady coherent vortices of the horseshoe system around the cylinder for the first 735 seconds. Kirkil et al. (2008) studied the coherent structures in the flow field around a circular cylinder using large eddy simulation at an equilibrium scour hole. The main difference in this study against previous work done by Kirkil et al. (2008) are that Kirkil et al. (2008) investigated the scour process for lower Reynolds number ($R_{e\mathrm{D}}$=1.62×10^4), and also with different sediment grid size (d_{50}=0.68 mm). Whereas in this study the $R_{e\mathrm{D}}$=3.9×10^4, and d_{50}=0.365 mm. Due to these difference, some variance in the results is expected to be found. Also, the flow in the scour hole at equilibrium conditions was investigated by Kirkil, Constantinescu et al. (2008), whereas in this study the flow was investigated at the initial stage scour evoluation.

In this section the grid size for the LES is equal to 12x10^6 cells. This is because that the time needed to solve LES with 24x10^6 cells is about 2.5 times

that needed with LES using $12x10^6$ cells. Beside that the combination of the LES model with the dynamic mesh technique increases the time needed to converge the solution at the same grid size. Table 4.1 shows the approximated time needed in hours to complete 1 second of real flow using LES for both grid sizes ($12x10^6$, and $24x10^6$) with and without dynamic mesh technique. These values were dependent on Fluent solver using HPC in parallel mode, with 64 processors. Table 4.1 shows that when the grid size increased to the double, the time needed to simulate 1 second of flow around bridge pier during scour process is increased up to 163%. In addition to that, the percentage of increment in the time needed to simulate one second of real flow using LES with erodible bed around bridge pier is about 33% in case of the LES with $12x10^6$ grid size and about 40% in case of the LES with $24x10^6$ grid size. Which is more than, when compared with simulating 1 second of flow around a cylinder mounted on flatbed using LES with the same grid size.

Table 4.1: The averaged time needed in hours to complete one second of real flow.

	without dynamic mesh technique	with dynamic mesh technique	% increase in time between LES with and without dynamic mesh technique for the same grid size ($12x10^6$, and $24x10^6$)
LES ($12x10^6$)	12 hrs.	16 hrs.	→ 33%
LES ($24x10^6$)	30 hrs.	42 hrs.	→ 40%
% increase in time between the two grid sizes ($12x10^6$, $24x10^6$)	↓ 150%	↓ 163%	

Figure 4.3 shows the predicted maximum scour depth for the first 100 seconds from scour initiation using LES with $12x10^6$, $24x10^6$ cells. The

percentage of difference between these two maximum scour depths at 100 seconds is about 10%, which is still considered acceptable compared to the time consumed in case of LES with 24x10^6 cell compared to LES with 12x10^6 cells.

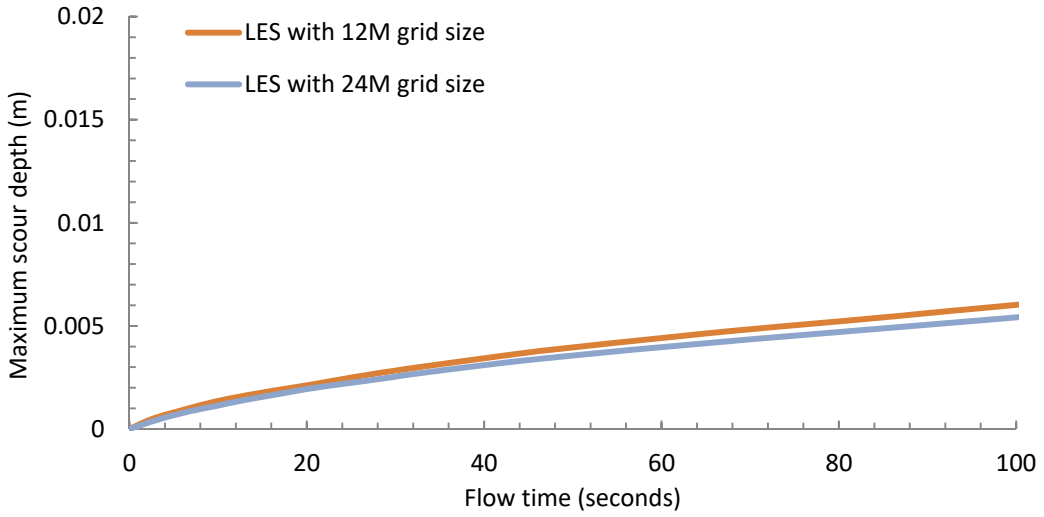

Figure 4.3: The maximum scour for the first 100 seconds of scour initiation using LES for both 12x10^6, and 24x10^6 grid size.

4.4.1 Erosion development

The moving-bed numerical simulation starts at t=0 seconds from the flatbed condition. The simulated inlet condition is that of the fully developed turbulent flow field obtained from the flat rigid-bed simulation described in Chapter 3. Due to the magnitude of the shear stresses resulting in the turbulent flow at the bed, the erodible bed (scour) commences immediately as a result of the effect of the horseshoe vortex system fluctuations upstream of the cylinder. Figure 4.4 shows the time averaged bed shear stress for the first 40 seconds. It is clear from the figure that the time averaged bed shear stress in some regions around the cylinder (which ranged from -0.28Pa to 0.78Pa) is greater than the critical shear stress of the sediment movement ($\tau_{b.cr}$=0.2Pa) from Equation 4.1.

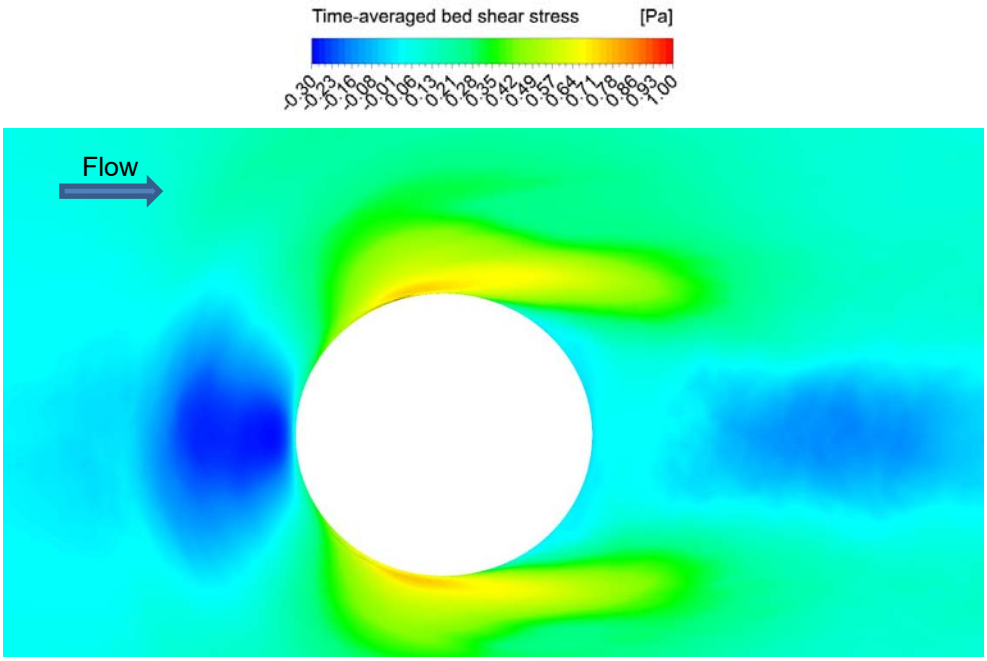

Figure 4.4: Time-averaged bed shear stress for period between (0-40 seconds).

Figure 4.5 shows the maximum development depth in the initial stage of the scouring process (i.e. first 735 seconds) around a circular cylinder. The maximum scour depth location agrees well with Dargahi (1990) observations, as it happens almost at the sides of the pier at about $\pm 45^{\circ}$ from the symmetry plane, which is also equivalent to the region of largest magnitude of shear stress as shown in Figure 4.4. Although the rate of scour produced in this study compared with the experimental measurement, is slower, it still predicts a very good estimation when compared with previous CFD studies by Escauriaza and Sotiropoulos (2011) as shown in Figure 4.5. In their study, they used DES together with an unsteady bed-load transport model based on the momentum equation of the sediment in an Eulerian framework to compute the maximum scour depth at 735 seconds for the same features and R_e as reported in Dargahi (1990). The maximum scour depth found by Escauriaza and Sotiropoulos (2011) was very small (0.9 cm) compared with this study (2.4 cm)

and to that of reported in the experimental study by Dargahi (1990) which was (3.0 cm).

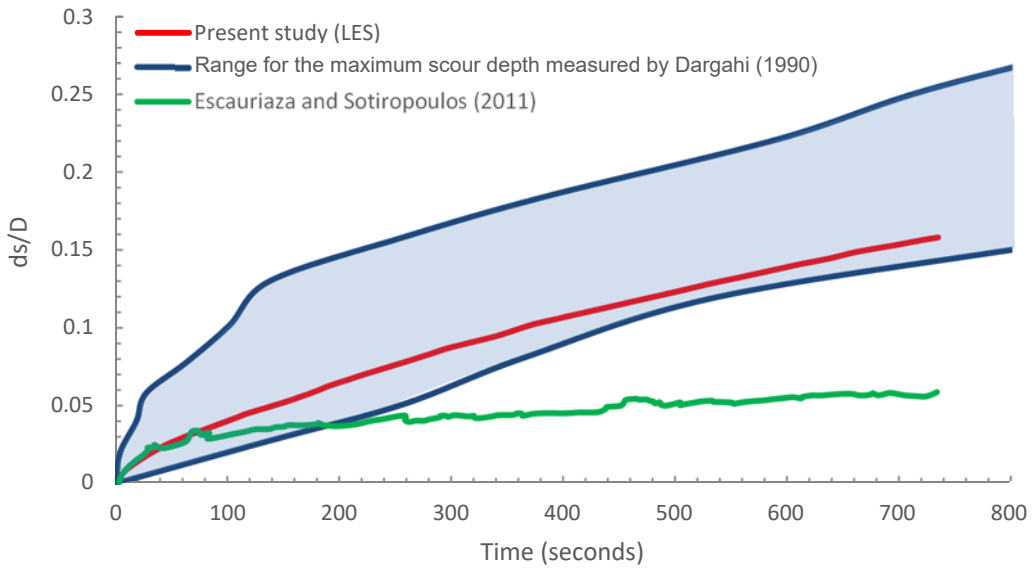

Figure 4.5: The development of maximum erosion on the bed for the first 735 seconds.

4.4.2 Scour development

Figure 4.6 shows the instantaneous bed contours around the cylinder. The range of contours changes as scour progresses to give additional details of the instantaneous bed features near the circular pier. In Figure 4.6(a) the bed deformation is just initiated near the base of the pier and near the symmetry plane upstream of the pier. Figures 4.6(b-e) show the progress of scour with time. With the development of the bed deformation and the maximum scour occurring at approximately $\pm 45^{\circ}$ from the symmetry plane upstream of the cylinder. Figure 4.6(f) shows further development of the scour hole around the cylinder. It can be clearly noticed that no further scour occurs after X=D upstream of the cylinder, where X is the distance from the edge of the scour hole to the front edge of the cylinder. This is because the effect of the down-flow on the riverbed after this point (X>D) is neglected, which is investigated in

detail in Section 5.3.1.1. Furthermore by studying the transient behaviour for the scour process around bridge pier it can be seen that the scour rate upstream of the cylinder in the initial stage of the scour evolution is slower than the scour rate at the both sides of the pier in the initial stage of the scour process(from 0 second to 735 second).

Another significant parameter is the bed shear stress distribution around the cylinder during scour process which shown in Figure 4.7. It can be seen from the snapshots that the instantaneous shear stress distribution changes with scour development. At 5 seconds of scour initiation as shown in Figure 4.7 (a), the bed shear distribution has the same behaviour in case of flow around cylinder mounted on flatbed (the scour effects not included). In Figures 4.7 (b-f) when the scour process develops from 40-735 seconds the bed shear stress distribution around the cylinder changes by reducing its magnitude upstream of the cylinder and producing a significant change on the both sides of the cylinder.

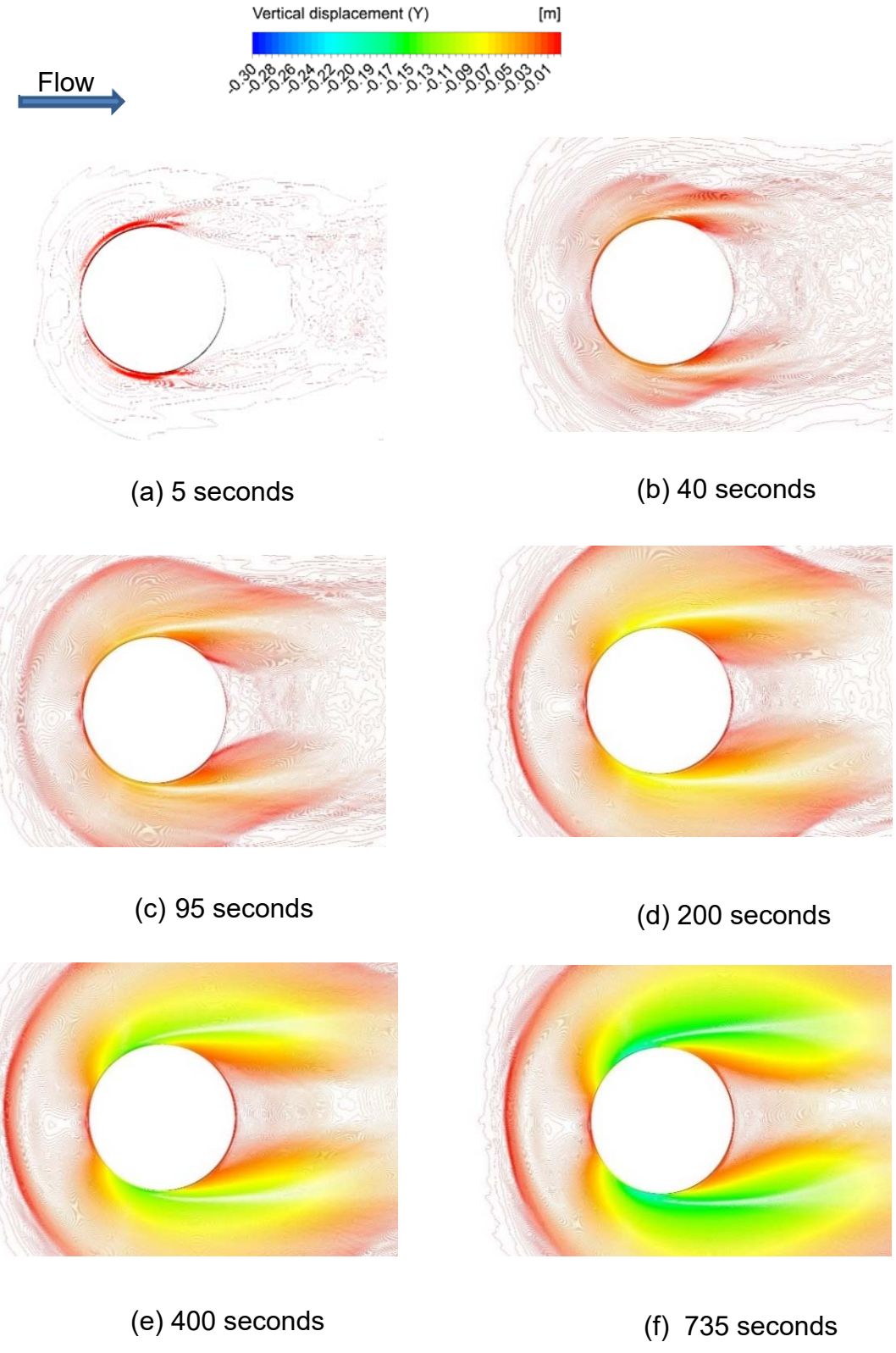

Figure 4.6: Contours of bed elevation at six instants in time, ranging from 5 to 735 seconds.

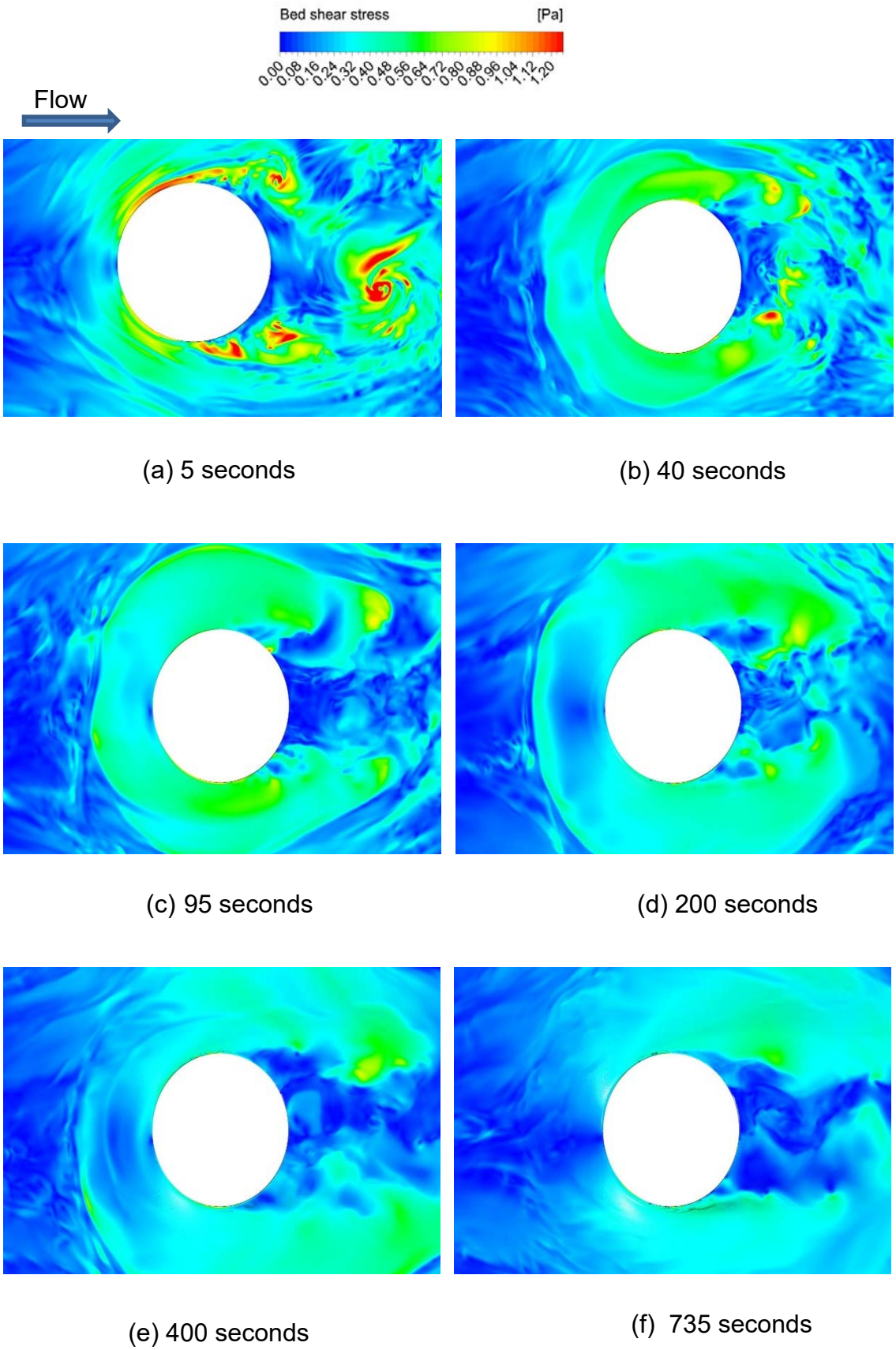

Figure 4.7: Instantaneous shear stress distribution at the bed during scour development.

4.5 Flow structure in the horseshoe region and dynamics of necklace vortices

Figure 4.8 shows the structure of the horseshoe vortex system in an instantaneous flow field. The streamlines of instantaneous velocity distribution at a symmetry plane are shown in Figure 4.9. For both Figures (4.8 and 4.9) the simulation was run for 45 seconds and the pictures were captured every 5 seconds of flow, started at flow time equal to 80 seconds and ended when the flow time equal to 125 seconds. It can be observed that V2, the main vortex, is the most stable one. This vortex is ‘trapped’ in the scour region and can be seen on almost all snapshots. There is another small vortex observed close to the cylinder, V1. From the animation analysis of this vortex, it appears less stable than V2. Upstream of vortex V2, more vortices can be identified. These vortices behave in an irregular way (not stable).

Figure 4.10 shows the time averaged flow field. Here two vortices can be clearly distinguished. These can be identified as V1 and V2. These two vortices have counter rotating effect. V2 rotates such that the flow near the bed is towards the upstream whereas the flow near to the bed below V1 is towards the downstream. The counter rotating of these two vortices (V1 and V2) has a significant effect on the scour developments upstream of the cylinder.

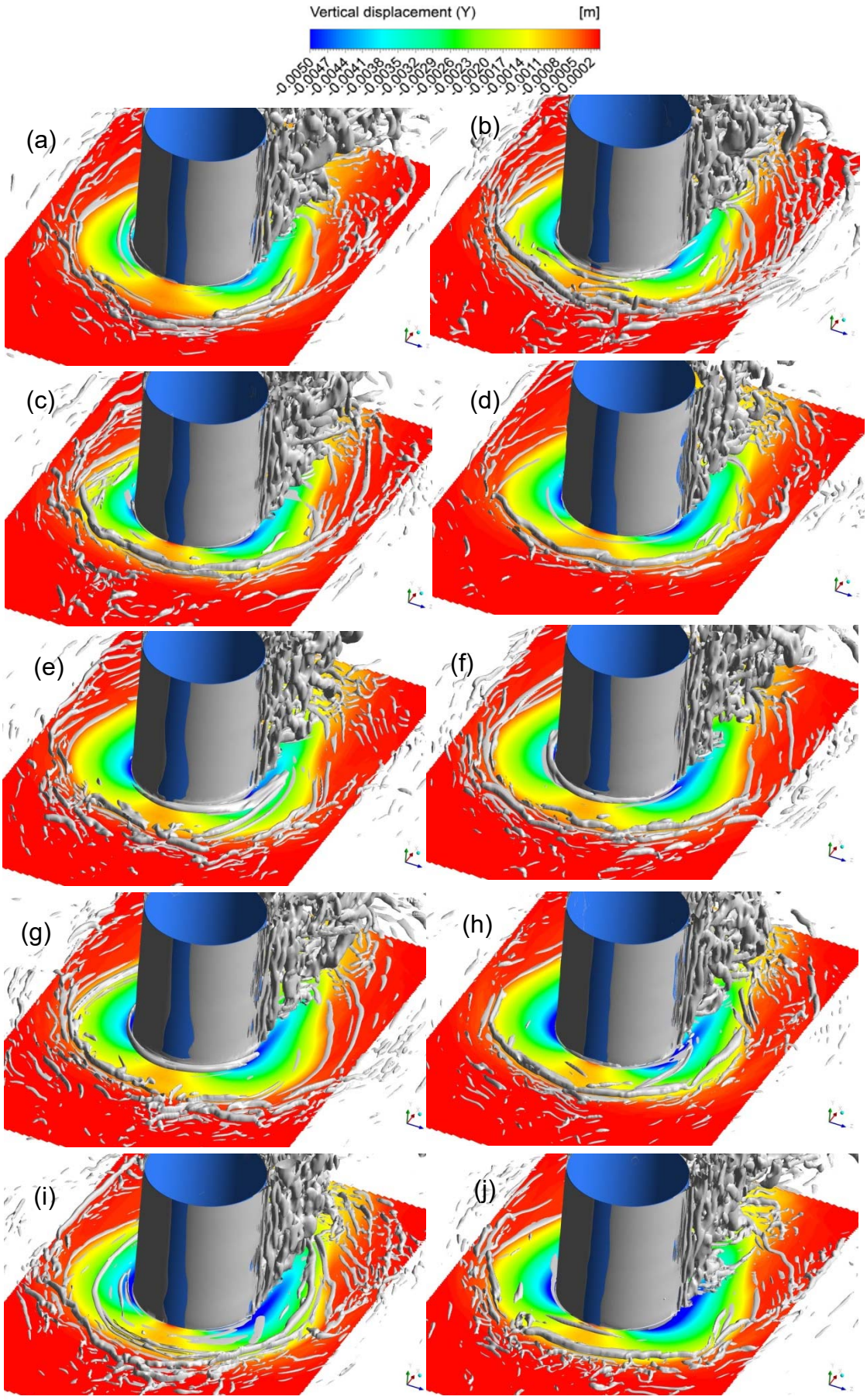

Figure 4.8: Large scale coherent structures in an instantaneous flow field every 5 seconds visualised using the Q criterion.

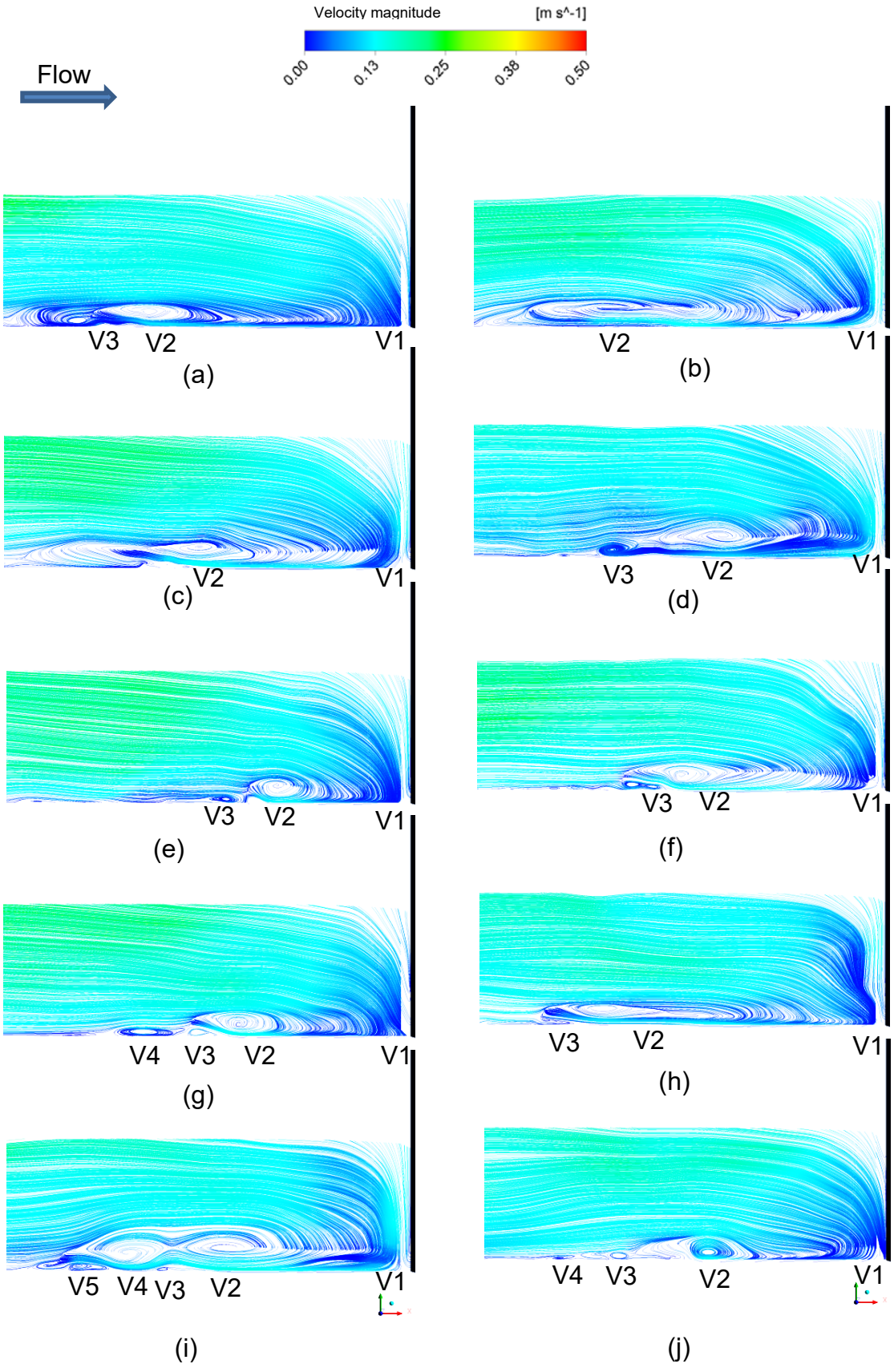

Figure 4.9: Visualisation of the horseshoe vortex system overtime for the 45 seconds of flow, the pictures captured at every 5 seconds.

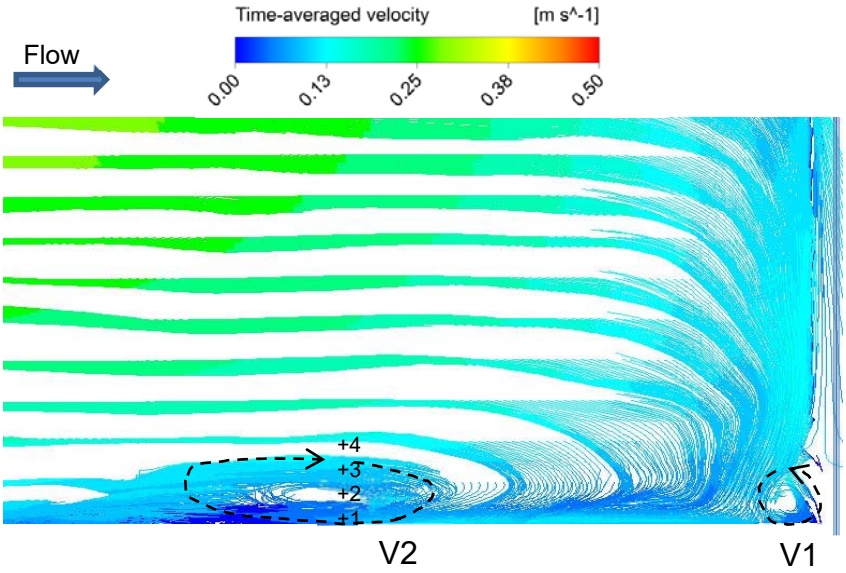

Figure 4.10: Time-averaged velocity stream lines at symmetry line upstream of the cylinder.

4.5.1 Bimodal oscillations

Figures 4.8, 4.9 in previous section show that the position and size of the V2 vortex is subject to sizeable transient variation. As the analysis below will highlight, and consistent with results of previous investigations of junction flows where a turbulent horseshoe vortex system forms, the V2 structure was found to be subject to large-scale aperiodic bimodal oscillations. The oscillations take place between a zero-flow mode, where V2 is situated close to the cylinder and the shape of its core is close to circular and a back-flow mode, where V2 is situated away from the cylinder, the size of its core is larger and the shape of its core is close to an ellipsoid. The visualisation in Figure 4.11 illustrates the transition of V2 from the zero-flow mode to the back-flow mode in the symmetry plane of the cylinder. The snapshots was taken every 5 seconds of flow between 90-105 seconds.

The average distance between the separation line and the cylinder's face in the symmetry plane is 0.55D when V2 is in the back-flow mode and 0.3D when V2 is in the zero-flow mode.

Once in the back-flow mode, a large but not very coherent necklace vortex system gets stretched around the cylinder and its cross section gets smaller. As a result, V2 moves closer to the cylinder (transition to the zero-flow mode).

Figure 4.12 shows histograms of Probability Density Function (PDF) of the radial velocity along a vertical line crossing the horseshoe vortex region in the symmetry plane. The two-peak shape of the streamwise velocity histogram in Figure 4.12 gives confirmation that the horseshoe vortex upstream of the obstacles undergoes bimodal oscillations. Four points were located at x/D= 1.0 and different elevations from the bed. From Figure 4.12 it can be clearly seen, at points inside the vortex V2 (i.e. 1, 2and 3) the PDF histogram has two peaks; this confirms the bimodal nature of these oscillations. Whereas at Point 4, which is located outside the vortex V2 boundary, a single peak in the probability density function histogram was observed. Kirkil (2007) showed that the URANS models cannot capture the bimodal oscillations. This support the advantage of large eddy simulation (LES) in catching the unsteady dynamics of the horseshoe vortex system observed in experimental study by Devenport and Simpson (1990). The phenomenon of moving the horseshoe vortex forward and backward from the base of the bridge pier increases the ability of these vortices to entrain sediment.

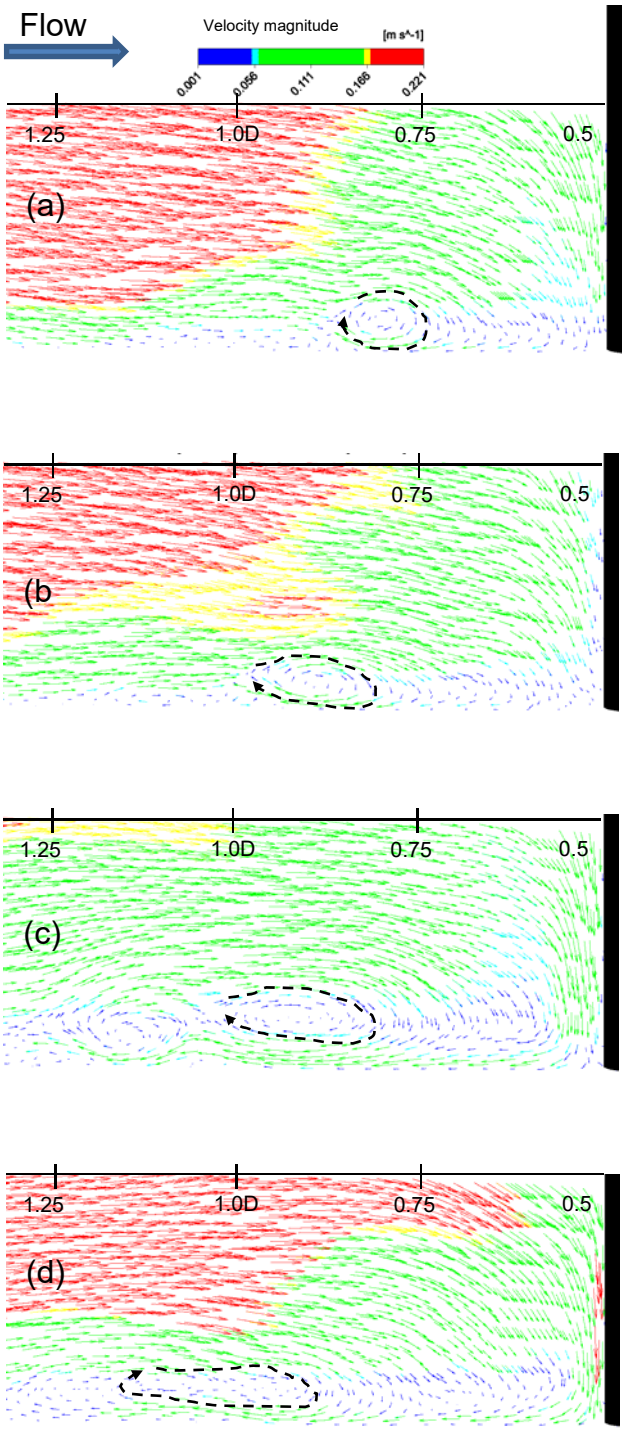

Figure 4.11: Visualisation of the horseshoe vortex system transitioning from the zero-flow mode to the back-flow mode at the symmetry plane upstream of the cylinder.

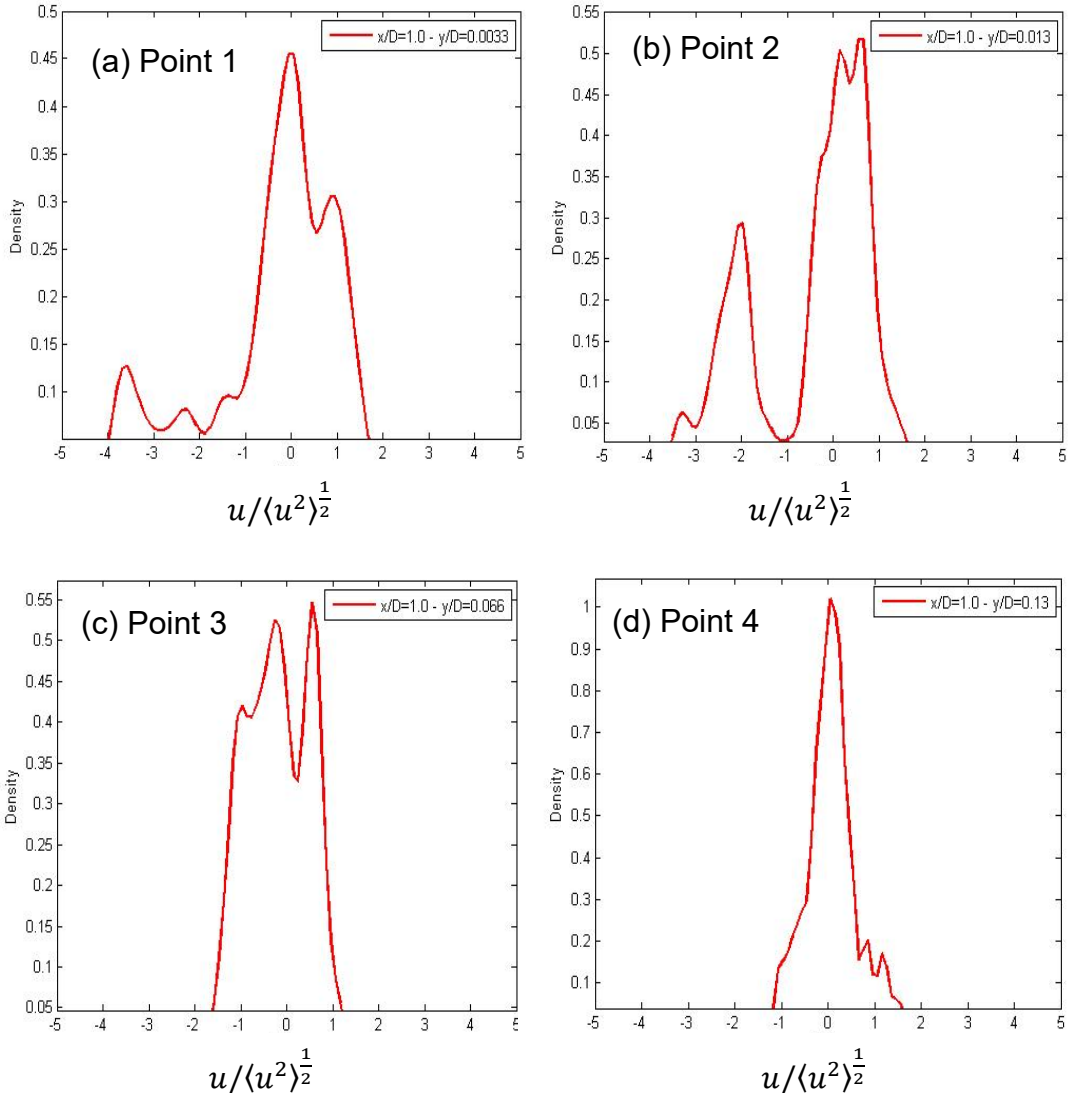

Figure 4.12: Histograms of probability density function of radial velocity showing normalised frequency vs. radial velocity along a vertical line cutting the horseshoe vortex region in the symmetry plane (see Figure 4.10) at (a) point 1; (b) point 2; (c) point 3; (d) point 4.

4.6 Summary and findings

A coupling methodology of the large eddy simulation with dynamic mesh technique is proposed in this chapter. This method can numerically study complicated 3D turbulent flow around bridge pier during entrainments of the bed sediment. It provides more details of how the coherent structures around a bridge pier behave as scour process develops. In general, this methodology

considered to be more efficient for numerical computations to predict the turbulent coherent structures around bridge pier during scour evolution and comparing it with other numerical investigations from the literature.

In this case, the results of the simulation show the 3D development of the bed topography because of the flow past around the circular cylinder. The simulation induces most the features reported by Dargahi (1990) during the initial stage of the scour around the cylinder such as:

- The maximum scour depth: Although the maximum scour depth produced in this study (2.4 cm) compared with the experimental measurement (3 cm) after 735 second from scour initiation, is slightly lower. It still predicts a very good estimation compared with the maximum scour depth for the same flow and pier characteristics from previous CFD study by Escauriaza and Sotiropoulos (2011) (0.9 cm at 735 seconds from scour starts).
- The maximum scour location from the symmetry plane: The maximum scour occurring at approximately $\pm 45^{\circ}$ from the symmetry plane upstream of the cylinder.
- The scour pattern: No further scour occurs after X=D upstream of the cylinder, where X is the distance from the edge of the scour hole to the front edge of the cylinder. This is because the effect of the downflow on the riverbed after this point (X>D) is neglected.

The flow field behaviour around bridge pier during scour evolution is also investigated as follow:

- When the scour process develop, the bed shear stress distribution around the cylinder changes by reducing its magnitude upstream of the cylinder and producing a significant change on the both sides of the cylinder.
- During scouring, the horseshoe vortex system characteristics have no considerable change. i.e.,
    - The main vortex V2 which is trapped inside the scour region and the small vortex which observed close to the cylinder V1 are the most stable vortices around bridge pier. Upstream of vortex V2 more vortices can be identified. These vortices behave in an irregular way (not stable).
    - The main vortex V2 rotates such that the flow near the bed is towards the upstream whereas the flow near to the bed below V1 is towards the downstream. The counter rotating of these two vortices (V1, and V2) has a significant effect on the scour developments upstream of the cylinder.
    - The main horseshoe vortex V2 has the bimodal oscillation phenomenon which is captured using LES. This phenomenon of moving the main horseshoe vortex forward and backward from the base of the bridge pier increases the ability of these vortices to entrain sediment.

All the predicted results presented in this chapter show that the combination of the LES with the dynamic mesh technique can capture the most relevant physics of the flow mechanisms during scour evolution. Therefore, it gives good

understanding for the complex relation between the coherent turbulent structures of the flow around the cylinder, and the sediment transport. This methodology can be easily adapted to model more complex problems such as the effect of the pier shape and the angle of attack of the approaching flow on the scour pattern around the bridge pier, as described in the next chapter. To the best of my knowledge, the present methodology is the first to successfully simulate the dynamics of the coherent structures in the initial stages of scour using LES technique.

Chapter 5

Effect of Pier Shape and Angle of Attack of the Approaching Flow on the Scour Process

Local scour around bridge piers is mainly caused by large scale coherent flow structures. These structures are strongly correlated to bed shear stress and have a significant effect on the bed erosion around bridge piers (Chang et al., 2011). This chapter concentrates on studying the influence of the pier shape and the angle of attack of the approaching flow on the character and strength of these large scale coherent structures around the pier in the initial stage of the scouring process. The resulting impact on the maximum scour depth is predicted using LES together with the dynamic mesh technique.

Simulations are undertaken at four angles of attack (α = 0°, 30°, 45° and 60°) having a R_{e_D}=3.9×10^4. An oblong pier shape is considered in this study. Few prior studies have reported on the local scour and coherent structures around this kind of pier. In addition to the circular and square shapes, this is the most commonly used, in bridge pier design (Debnath and Chaudhuri, 2012).

The outlines of this chapter are as follows: Section 5.1 reports the numerical simulation parameters and the domain geometry setup. The boundary conditions and the grids used in the simulation are also presented in this section. In Section 5.2 the predicted results are discussed. Which is divided into two parts; the first is based on the pier shape (circular, or oblong) by

comparing the predicted results for the different bridge pier shapes. The effects of the time-averaged velocities and the mean bed shear stress distribution on the maximum scour rate around bridge pier are also considered. The behaviour of the flow field in the initial stage of the scour process is also studied. The second part investigates the effects of the angle of attack of the approaching flow on the maximum scour depth. A discussion on the effect of the predicted results (such as mean bed shear stress, the vortices in the wake region, and the horseshoe vortex system upstream of the cylinder) on the scour pattern and maximum scour depth have been studied. Finally, in Section 5.3 the summary and findings of this chapter are presented.

5.1 Flow solver and computational grid

LES setup with parameters and the boundary conditions used to simulate the turbulent flow around the oblong bridge pier are the same, as used simulating the flow around the circular pier in Chapter 3.

Figure 5.1 shows the computational domain used to simulate the flow in the case of the oblong cylinder. The domain width is 10D where D is the width of the pier. To eliminate the effect of pier width on the maximum scour depth, the width of the oblong bridge pier has been taken equal to the diameter of the circular pier that was studied in previous chapter (D=0.15m). The computational domain extends 6D upstream of the centroid of the pier, and 12D downstream of the centroid of the pier; the length of the pier is equal to 3D. All flow properties (including the mean flow velocity and the approaching flow depth) were taken as same as in the case of circular cylinder studied in detail in Chapter 3 (see Table 3.1).

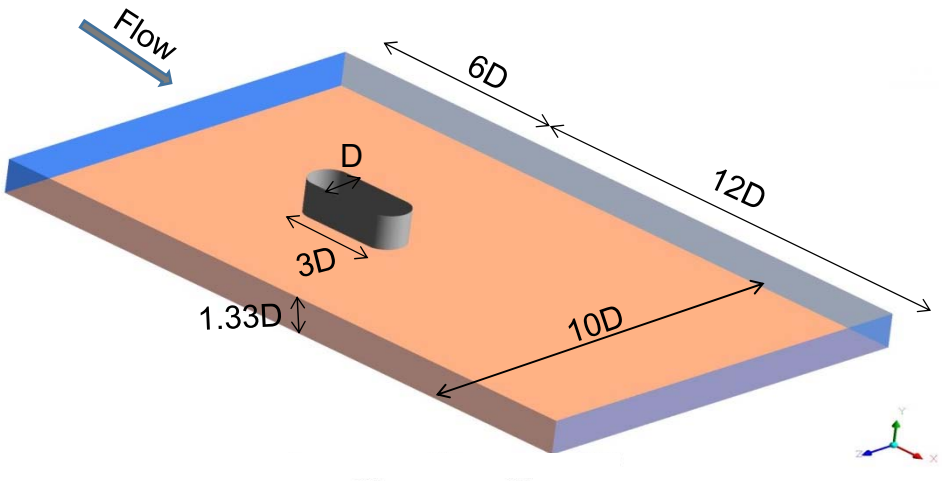

Figure 5.1: The geometric setup for the oblong bridge pier simulation.

The hexahedral mesh distribution presented in Figure 5.2 is designed to make sure the grids within the computational domain are more concentrated in the regions close to the bridge pier. This is due to the flow pattern in this region being more complex, and being an important region to resolve accurately. The grid size for all simulations is approximately 12×10^6 cells. The time step is equal to 0.001 seconds which ensures the maximum CFL ≤ 1 for the R_e used.

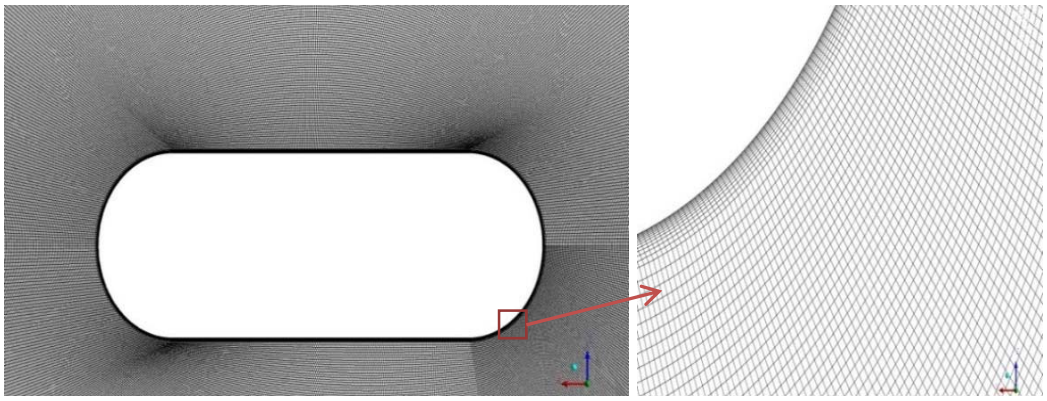

(a) (b)

Figure 5.2: Computational grid for the oblong bridge pier simulation (a) top view, (b) mesh close to the pier.

The scour development for the case of flow around oblong bridge pier (subjected to different angles of attack) has been simulated using the same dynamic mesh technique which has been discussed in Chapter 4.

5.2 Discussion of flow physics and simulations

5.2.1 Pier shape effect on the scour development

The significant parameters that affect the scour development are those concerning the down-flow and therefore the character and size of the horseshoe vortex and the resulting bed shear stress close to the cylinder. In this section, a comparison is made with the circular bridge pier to study the effects of the pier shape (an oblong pier was considered in this study) on the velocity distribution close to the riverbed, the bed shear stress and the associated scour evolution around the bridge pier. The turbulent flow field behaviour in the scour region has been also investigated.

5.2.1.1 Predicted velocity distribution

Figure 5.3 shows the contours of the mean velocity distribution at a distance equal to y/H= 0.0025 above the riverbed, just upstream of the point of the start of the scour region. This plane of study is located inside the thin zone between the stagnation point and the riverbed as discussed in Figure 5.5. The maximum mean velocity magnitude is located close to the cylinder. In the two configurations shown in Figure 5.3, it has been observed that the maximum velocity magnitude in the case of circular cylinder (U_{max}=0.296 m/s) is greater than the maximum velocity around the oblong cylinder (U_{max}=0.275 m/s) which is a fall of approximately 7%. This fall in the velocity magnitude close to the oblong cylinder compared with the velocity magnitude in case of circular

cylinder is due to the reduction in the streamwise velocity and the approaching vertical velocity in the three co-ordinate directions (longitudinal, vertical, and transverse) as shown later.

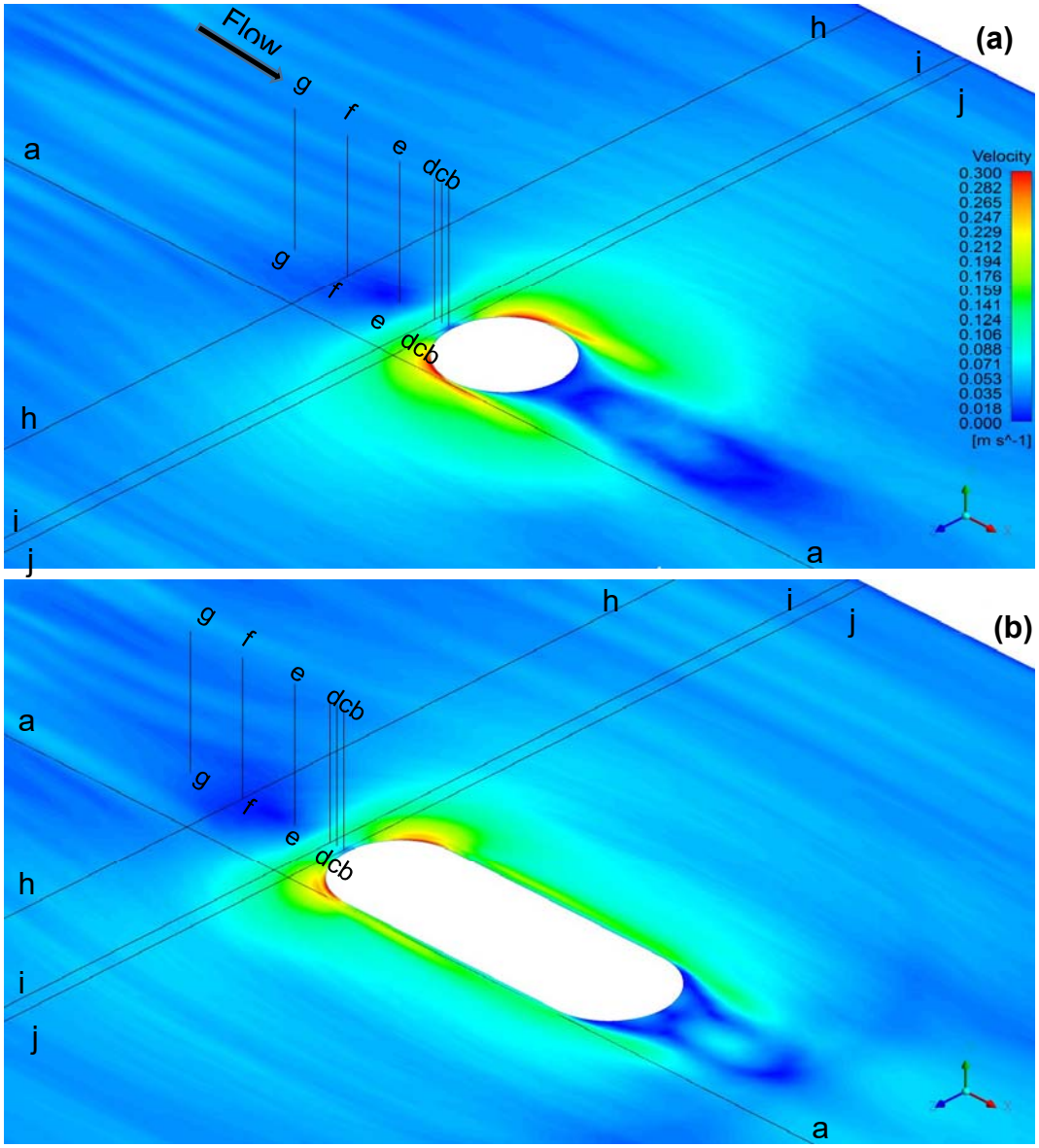

Figure 5.3: Velocity magnitude distributions at a distance y/H=0.0025 above the bed around (a) circular pier and (b) oblong pier. Sections a-a to j-j indicate where comparisons are made.

Figure 5.4 shows the streamwise and vertical velocity components along the channel length at a distance equal to D/30 from the right side of the cylinder (oblong and circular) relative to the incoming flow direction (see Figure 5.3 (a-

a)). Streamwise and vertical velocity changes were considered at a height of y/H = 0.0025 above the riverbed. As can be seen, the streamwise flow velocity increases for both geometries on reaching the pier. This is due to the reduction in cross-sectional area caused by the pier. Furthermore, because of the downward flow in front of the pier, the vertical velocity increases in the downflow direction. The comparison between the oblong and circular piers

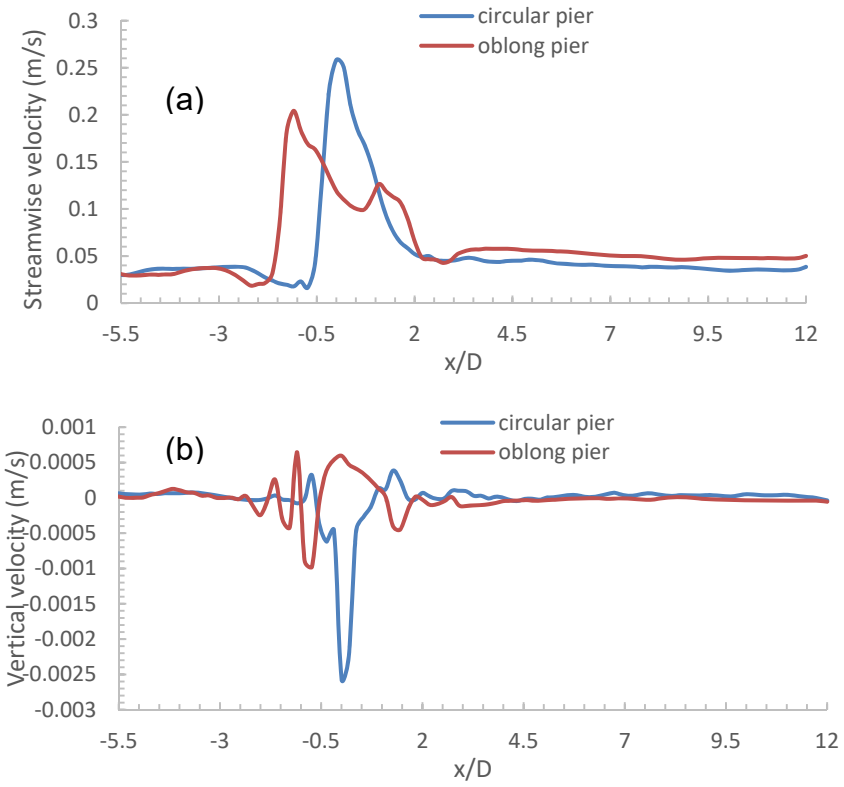

Figure 5.4: (a) Streamwise velocity and (b) vertical velocity changes in the channel at a distance = D/30 from the right side of oblong and circular piers, and at a height y/H=0.0025 above the riverbed (Section a-a in Figure 5.3).

shows that there are lower streamwise and vertical velocities around the oblong pier compared to the circular one. This indicates, it's likely that a lower scour depth will result around this type of pier compared to circular pier.

Figure 5.5 shows the mean vertical velocity profiles located at six different distances in the symmetry plane upstream of the pier, starting close to the pier

with X=width of the pier (D) divided by 30, and moving a way, upstream, to X=1.5 times width of the pier (D) (see Figure 5.3, Sections b-b to g-g). It shows that the maximum mean downward velocity magnitude increases when the approaching flow becomes closer to the cylinder. From the two configurations it is observed that at up to X=D from the pier, the vertical component of velocity is null and from X=D/2 toward the pier, the vertical velocity is strongly deflected in the vertical direction which is similar to the horseshoe vortex (Unger and Hager, 2007).

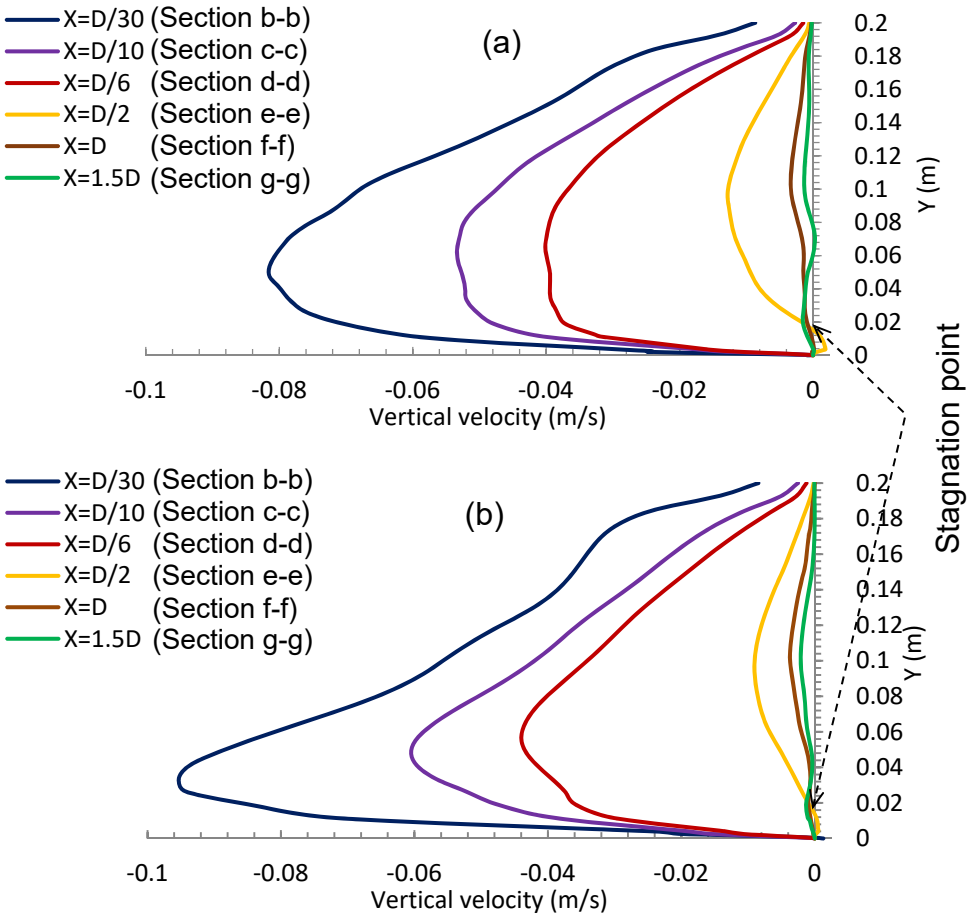

Figure 5.5: Mean vertical velocity profiles at different distances from the front face of the pier (Sections b-b to g-g in Figure 5.3) of 30,000 time steps (30 seconds) (a) circular cylinder (b) oblong cylinder.

In Figure 5.6 the vertical velocity profile is examined closely at two different distances away from the pier (X=D/6, and X=D/10, see Figure 5.3, Sections c-c and d-d). In Figure 5.5, the stagnation point in the two configurations is approximately similar at y=0.015m from the bed and at a distance equal to D/2 (see the yellow line in Figure 5.5) from the pier. This thin zone thin zone of water confined between the riverbed and the stagnation point appears to be important. Figure 5.6 shows the vertical velocity up to a distance y=0.015m from the riverbed. This layer has a slightly higher vertical velocity in the case of the circular pier than the oblong pier. Additional evidence on the effect of the pier shape on the downflow in front of the pier is shown in Figure 5.7.

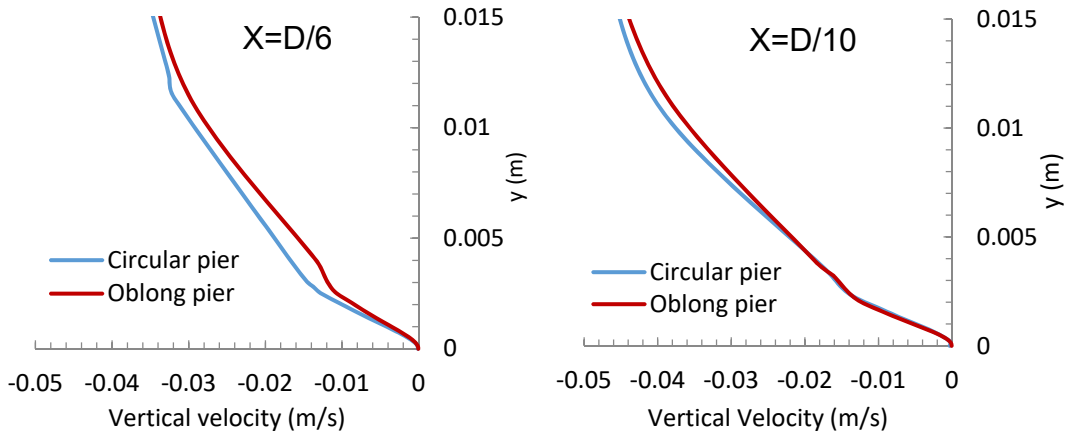

Figure 5.6: Mean vertical velocity profiles at X=D/6 and X=D/10 (see Sections c-c and d-d in Figure 5.3).

Figure 5.7 shows the vertical velocity distributions along the transverse line near the bed ($y/H = 0.0025$) at three different distances from the front face of the pier at X=D, X=D/6, and X=D/30 (see Figure 5.3, Sections h-h, i-i and j-j). As identified before in Figures 5.5 and 5.6, the maximum down-flow magnitude rises when the approaching flow gets closer to the cylinder. In these three configurations (Figure 5.7 a, b and c) at a distance X=D from the pier, the vertical component of velocity is negligibly close to zero (as mentioned before),

and at X=D/6 toward the pier at a distance X=D/30, the vertical velocity magnitude increases gradually. Figure 5.7(b and c) shows that the downward velocity near the riverbed is higher in the case of the circular pier than the oblong pier, and this difference increases as the flow comes closer to the pier.

The differences in the down-flow close to the cylinder are seen when studying the approaching vertical velocity in the three co-ordinate directions (longitudinal, vertical, and transverse). The result is a stronger horseshoe vortex system and thus a higher bed shear stress. Therefore, a higher risk of scour in the case of circular bridge pier compared with the oblong pier (for cases having the same width).

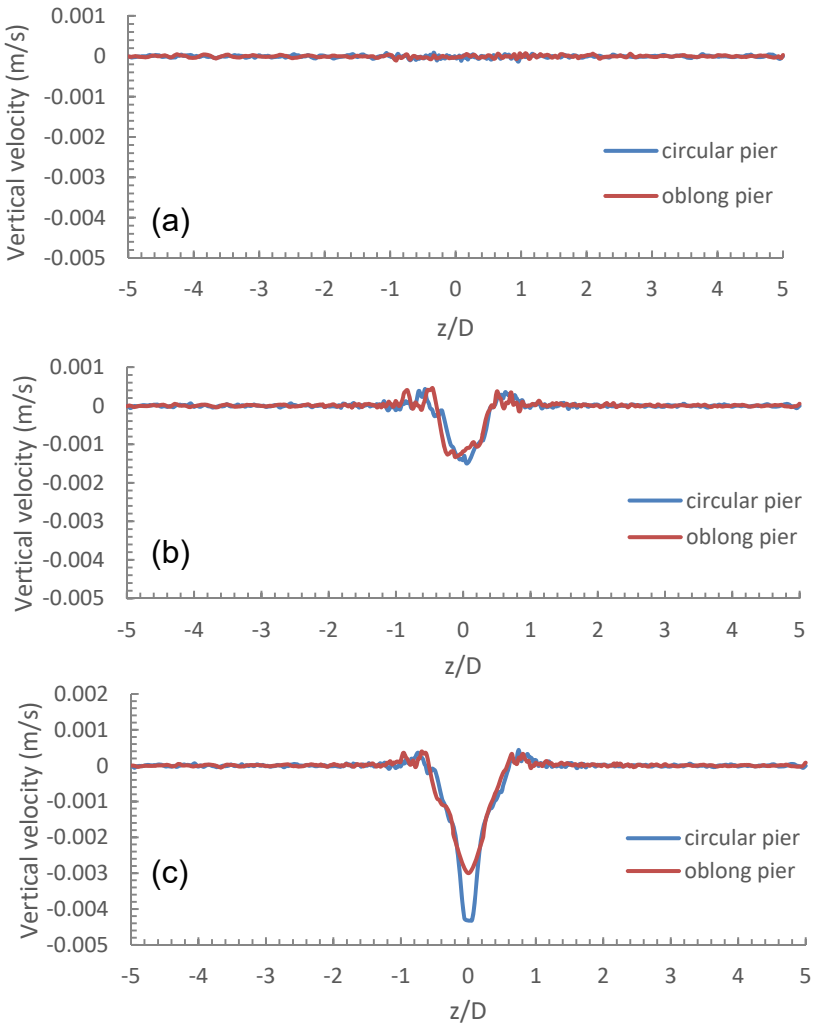

Figure 5.7: Vertical velocity distributions along the transverse line close to the bed at distances in front of the pier (a)X=D (Section h-h), (b) X=D/6 (Section i-i), and (c) X=D/30 (Section j-j).

5.2.1.2 Maximum shear stress

The results of the mean bed shear stress in the streamwise direction is examined and discussed with the objective of understanding the influence of the pier shapes on the bed shear stress and the consequence on the scour depth around the pier. It's important since the bed shear stress is considered as a key parameter to control the scour depth and pattern around the pier.

Figure 5.8 shows the overall mean streamwise bed shear stress for both circular and oblong bridge piers. The maximum bed shear stress around the circular pier (0.96 Pa) is greater than maximum around the oblong pier (0.75 Pa) i.e. a fall of approximately 21% between these two shapes. This difference in the mean shear stress can be demonstrated by the higher vertical velocity observed close to the bed in the case of circular pier.

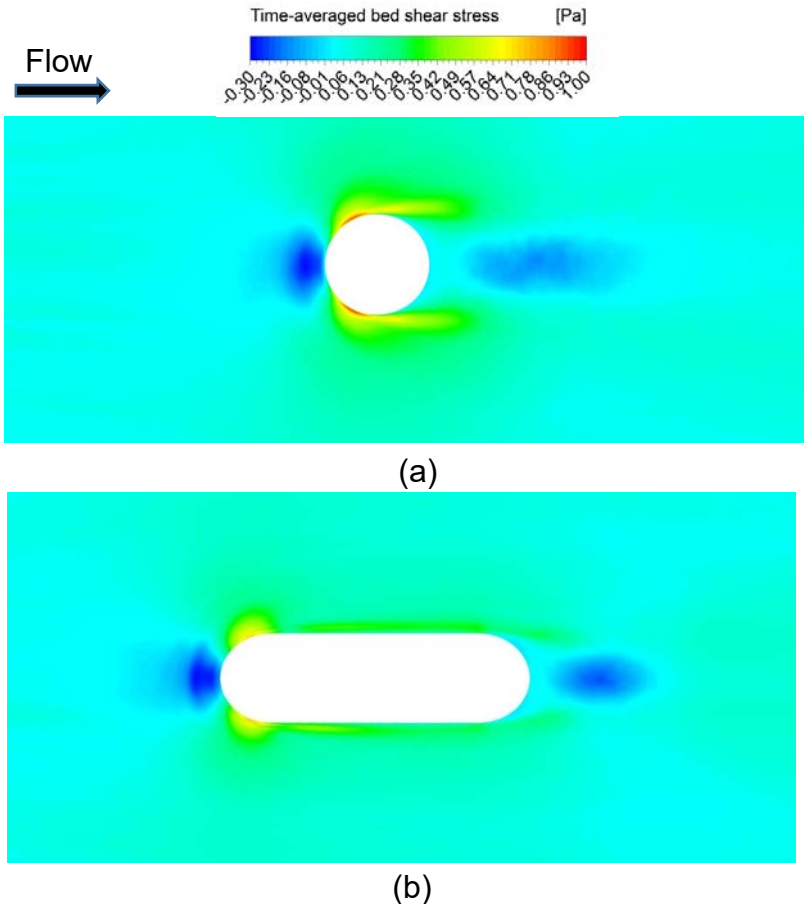

Figure 5.8: Mean bed shear stress, after 30,000 time steps (30 seconds) for (a) circular cylinder and (b) oblong cylinder.

The resulting velocity distributions and bed shear stress around different shapes of bridge pier (circular and oblong) from the numerical solutions indicate that these parameters vary depending on the bridge pier shape. The parametric study identifies that; with a constant bridge pier width (the shape of the oblong bridge pier studied in this chapter) there is a reduction in the shear stress around the bridge pier compared to the circular bridge pier.

5.2.1.3 Effect of the pier shape on the maximum scour depth and sediment transport rate

In this section, the scour parameters, (the magnitude and the rate of the maximum scour depth, the volume and the rate of the sediment removed from the scour hole around the circular and the oblong piers) are investigated. These parameters are considered significant towards understanding the behaviour of the scour pattern around the bridge pier. Therefore understanding the measures is necessary to protect the pier against scour failure. After 200 seconds, the value of the maximum scour depth (d_s) in the case of a circular cylinder (0.96 cm) is greater than the maximum scour depth in the case of an oblong pier (0.75 cm). This is an increase of about 24% as shown in Figure 5.9a. Figure 5.9b shows the rate of the maximum scour depth around the circular and oblong bridge piers. The results show that the maximum scour rate in the case of the circular shape is higher when compared with the maximum scour rate in the case of oblong cylinder. The difference in scour rate between them appears to become constant after a certain time (150 seconds in this study). This study investigates the characteristics of the scour rate and the sediment removed from the scour hole in the very initial stage of the scour evolution (200 seconds). When the scour depth approaches the equilibrium

scour depth, the scour rate and the sediment removal reduced until they become equal to zero. This final stage of the scour has not been seen in the Figure 5.9 since it needs to a vast CPU time with LES simulation.

Figure 5.9c shows a comparison in the quantity of the sediment removed from the scour hole (Vs) between the circular and oblong cylinder for the first 200 seconds of flow. The total sediment removed from the scour hole in the case of a circular cylinder (191 cm^3) is about two times the volume of sediment removed in the case of an oblong cylinder (103 cm^3). Figure 5.10 shows the 3D bed elevation around the circular and oblong cylinder after 200 seconds from scour initiation. The blue colour in the figure represents the scour hole around the cylinder. The figure provides an overview of shape of the scour hole that develops due to the coherent structures around the cylinder. The rates of the sediment transport for both circular and oblong shape are investigated in Figure 5.9d. It can be clearly observed that after a certain time of flow (about 150 seconds in this study) the rates of the sediment transport become approximately constant for both pier shapes. The rate of sediment transport in the case of circular cylinder (1.60 cm/s) is about twice the rate of sediment transport in the case of circular cylinder (0.85 cm/s).

All the predicted results related to the characteristics of scour evolution around bridge piers (such as the maximum scour depth, and the volume of sediment removed from the scour hole) indicate that in design the bridge piers in a straight river, the oblong shape is likely to be less risky for scour failure as compared to circular shape (for cases having the same width).

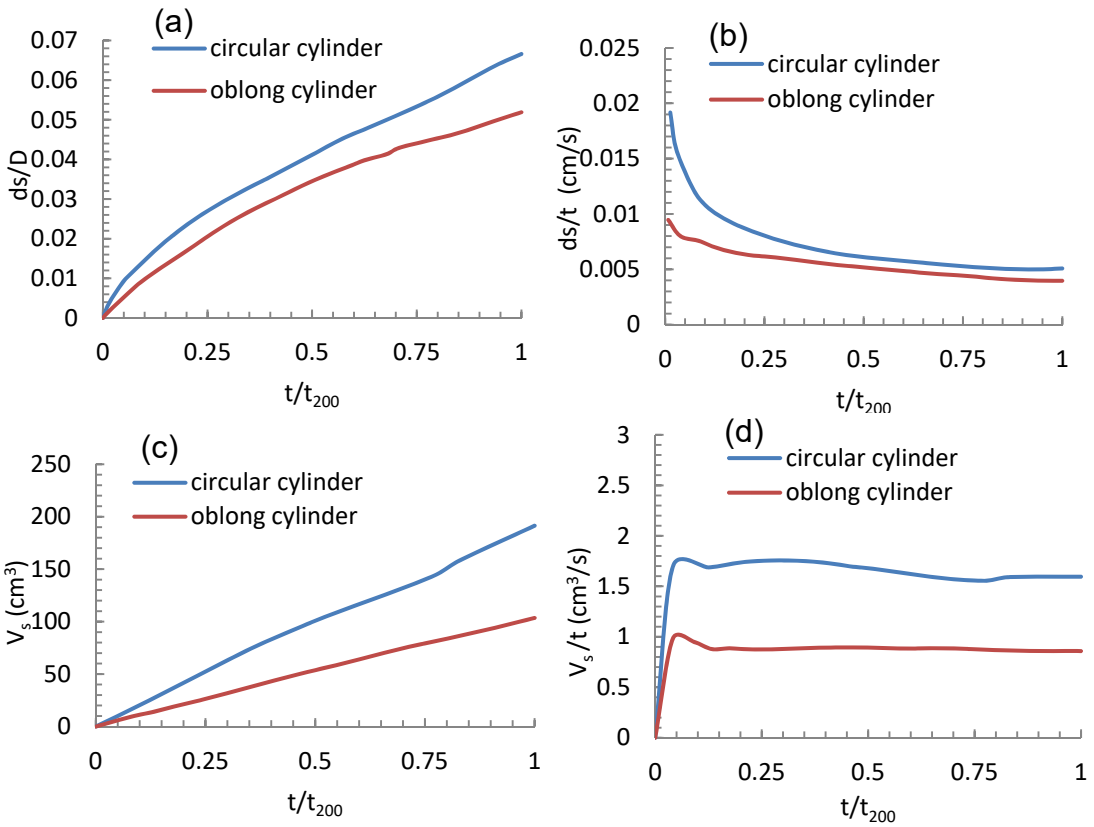

Figure 5.9: Scour measurements around a circular pier and an oblong bridge pier: (a and b) value and rate of the maximum scour depth, (c, and d) volume and rate of the removed sediment from scour hole.

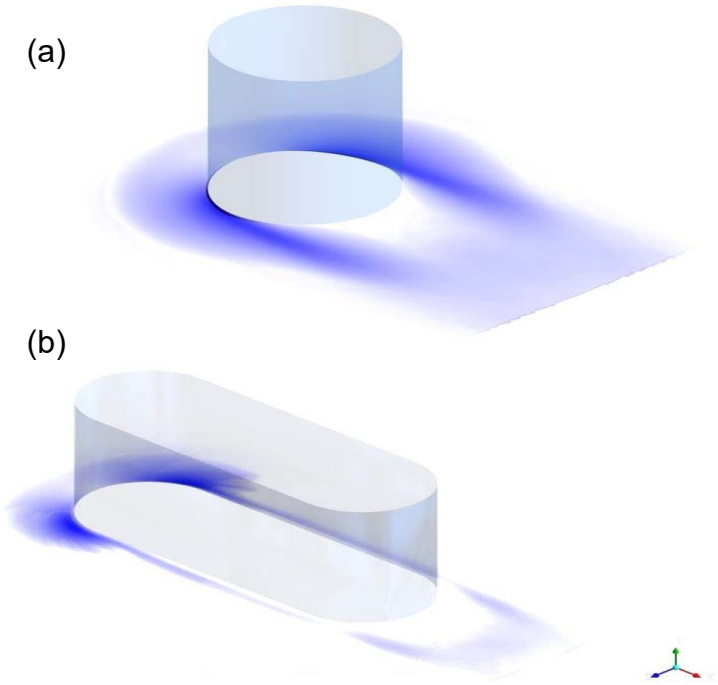

Figure 5.10: Three-dimensional scour shape around (a) circular cylinder, (b) oblong cylinder, after 200 seconds of flow.

5.2.1.4 Turbulent flow-field in the scour region

The effect of the bed shear stress distribution by the scour hole development around the oblong bridge pier is described in this section (for the case of the circular cylinder see Section 4.4.2). Figure 5.11 shows the bed shear stress distribution during the scour hole evolution for the case of the oblong pier which has the same behaviour of the bed shear stress distribution in case of circular pier (see Figure 4.7 for case of circular pier). Figure 5.11a shows the bed shear stress after 10 seconds from scour initiation. The bed shear distribution at this stage has not been influenced by the scour hole. As the scour evolves, the shear stress magnitude decreases in the front of the cylinder, inducing a significant change in the both sides of the cylinder as shown in Figure 5.11 b for case of 200 seconds of scour.

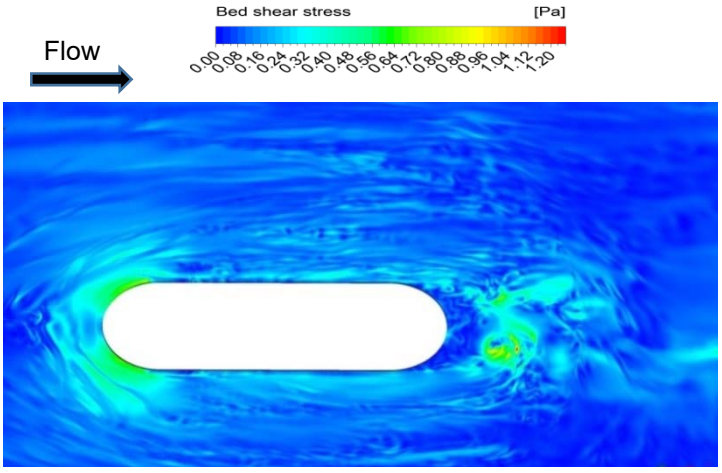

(a) t=10 seconds

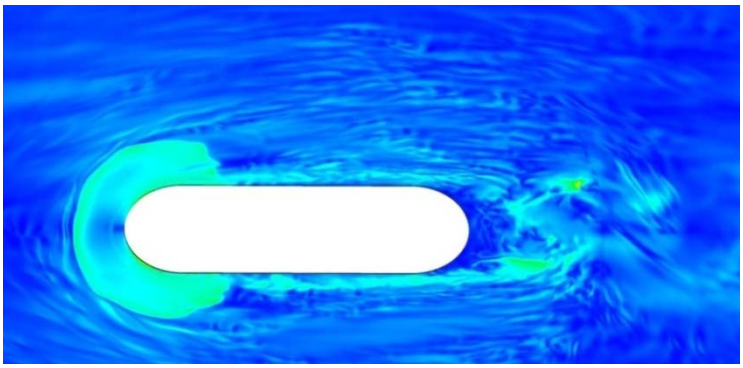

(b) t=200 seconds

Figure 5.11: The instantaneous bed shear stress around oblong cylinder after two different times (a) 10 seconds and (b) 200 seconds from the scour initiation.

Although the flow field around the cylinder changes as scour develops, depending on the cylinder shape, the characteristics of the horseshoe vortex system remain the same with few appreciable changes during the scour process. This phenomenon has also been reported by Dargahi (1990). Figure 5.12 shows the Q-criterion of the coherent structures around oblong cylinder after 10 and 200 seconds of the scour initiation. As scour develops, the main vortices V1 and V2 remain stable and many vortices are observed behind V2 that have less stability when compared with V1 and V2.

Examining the transient behaviour between the two flow times (10 and 200 seconds), the main vortex (V2) moves inside the scour hole forward and backward from the base of the cylinder. This movement induces a bimodal oscillation that is responsible to entrain the sediment around the bridge pier (as discussed in detail in Section 4.5 for the case of circular pier).

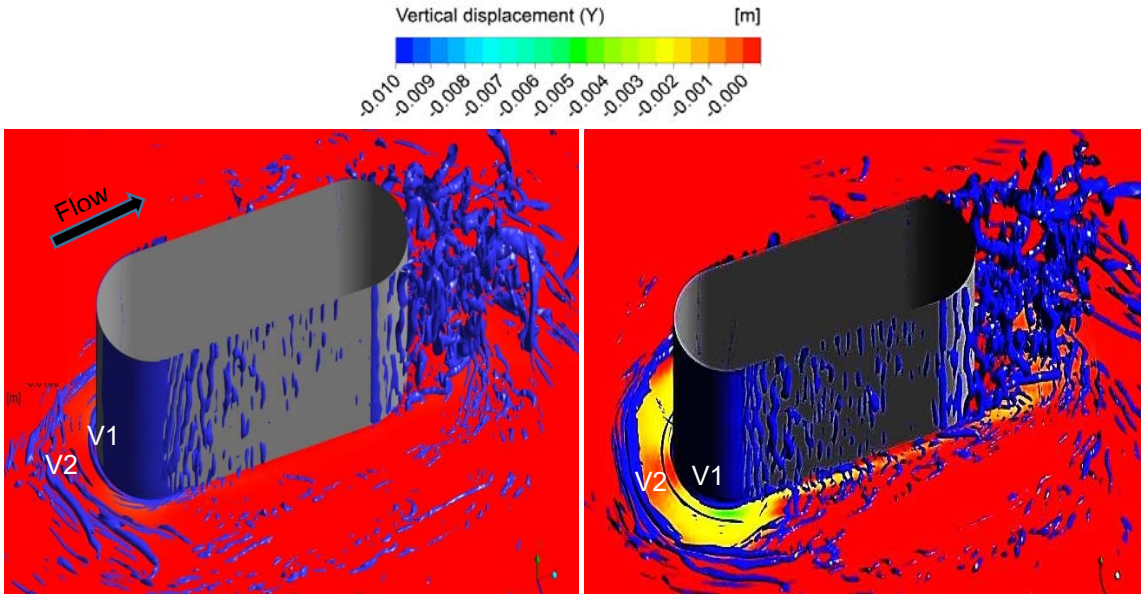

(a) t=10 seconds (b) t=200 seconds

Figure 5.12: The Q-criterion of the coherent structures around oblong pier after (a) 10 seconds, (b) 200 seconds from the scour initiation.

5.2.2 Angle of attack effect on maximum scour depth

For the case where a bridge pier is in a river bend, the approaching flow direction and the long direction of the oblong bridge pier will not align. The angle between the two is referred to as the angle of attack (α). The angle of attack is broadly considered to have significant impact on the flow pattern around bridge piers and therefore on the scour evolution. To obtain an understanding of impact of only the angle of attack variation on the maximum scour depth a series of simulation was undertaken in which all other parameters which effect scour depth such as the pier shape, the width of the pier, the velocity magnitude and water depth of the approaching flow (mean velocity equal to 0.26 m/s, and water depth equal to 0.2m) have been kept constant and equal to those already presented in this study.

5.2.2.1 Maximum shear stress

The effect of the angle of attack on the maximum streamwise shear stress τ_{max}, which is created on the riverbed around the pier just before scour initiation is described. Figure 5.13 shows the bed shear stress for different angles of attack (30°,$45^{\circ}$and 60°), it can be seen, by noting the increased red and yellow region, the maximum shear stress increases with an increase in the angle of attack $\tau_{max} \approx 1.18, 1.36,$ and 1.62 Pa for $\alpha = 30^{\circ},\ 45^{\circ},\ 60^{\circ}$ respectively. A difference of approximately 36%, 45% and 54% in the mean bed shear stress around oblong pier in case of $\alpha = 30^{\circ}$, 45° and 60°respectively with respect to $\alpha = 0^{\circ}$. This observation gives a strong indication of the effect of increasing the angle of attack on the bed shear stress distribution and on the maximum scour depth around bridge pier.

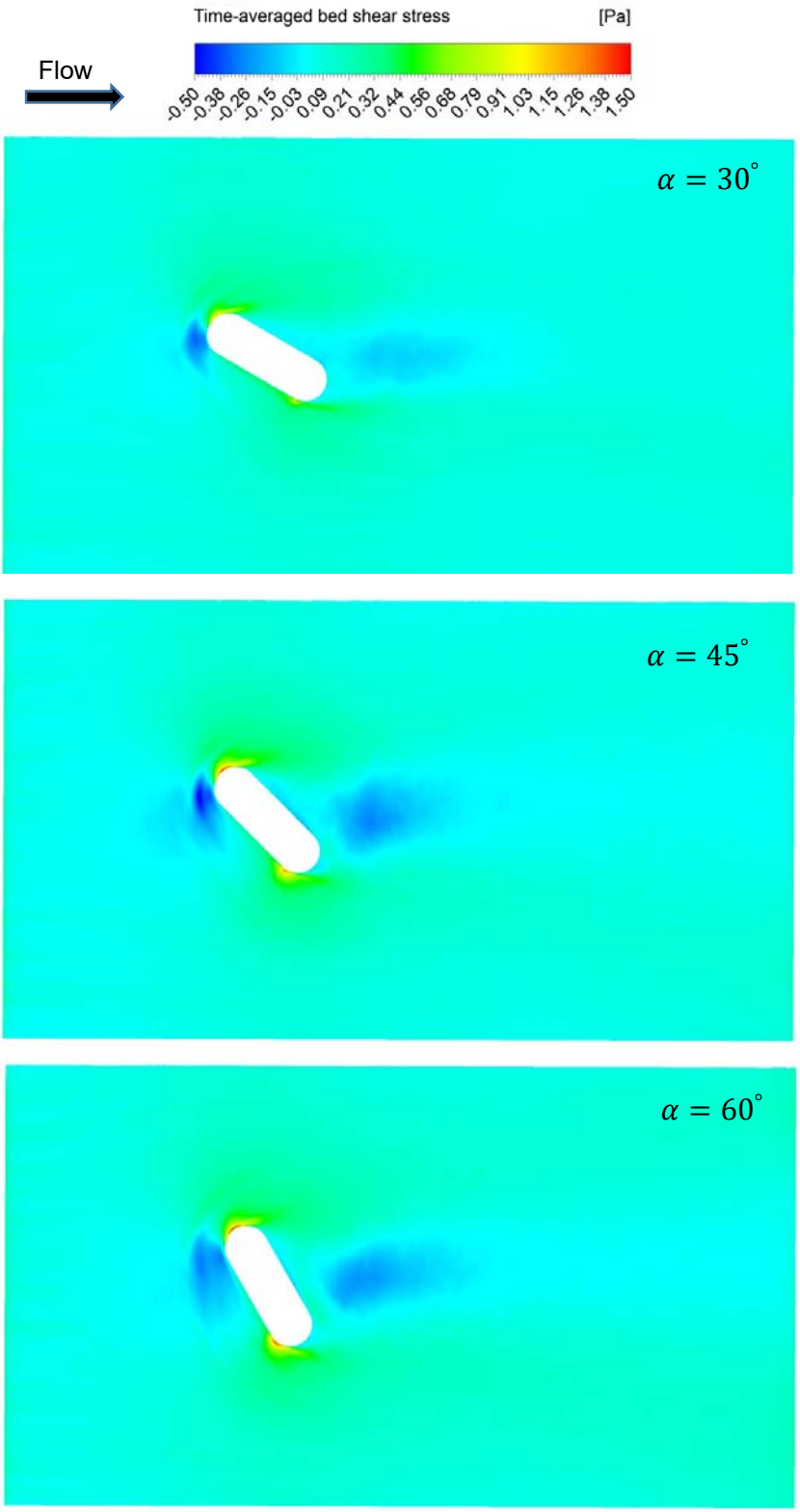

Figure 5.13: Time-averaged bed shear stress around the oblong pier subjected to different angles of attack.

5.2.2.2 Near-bed vortical content and wake flow

The recirculation region and the separated shear layer close to the bed level ($y/H = 0.0025$) and near to the cylinder are shown in the time-averaged velocity contour lines in Figure 5.14. For the case with a zero angle of attack (Figure 5.14a) the approaching flow reaches to the upstream face of the cylinder and reattaches to the lateral faces and forms two small vortices. Two small vortices are then generated behind the downstream face of the cylinder, as the boundary layers on the two lateral faces separate. For flow with angles of attack shown in Figures 5.14 b, c and d, the approaching flow is deflected by the upstream edge of the cylinder and the flow remains attached over the whole length of the right side (relative to the approaching flow direction) of the cylinder. This is predicted, as the attached boundary layer on the right side of the cylinder occurs in pressure gradients whose magnitude increases with α as shown in Figure 5.15. Meanwhile, the flow transported on the lateral face (left side of the cylinder) separates and generates vortices that extend over the whole left lateral face of the cylinder and travels some distance downstream of the cylinder.

The mean pressure distribution around the cylinder at a constant distance from the riverbed ($y/H = 0.0025$) is strongly dependent on α. The maximum pressure difference between the stagnation point and the minimum pressure within the recirculation region can be expressed non-dimensionally and increases with α as 3.7, 4.4, 5.5 and 6.2 for $\alpha = 0^{\circ}, 30^{\circ}, 45^{\circ}$ and 60° respectively as shown in Figure 5.15. The same behaviour of the mean pressure coefficient in the case of a rectangular cylinder with high aspect ratio subjected to low and

moderate angles of attack (α = 0°, $15^{\circ}$and 30°), was observed by Chang et al. (2011).

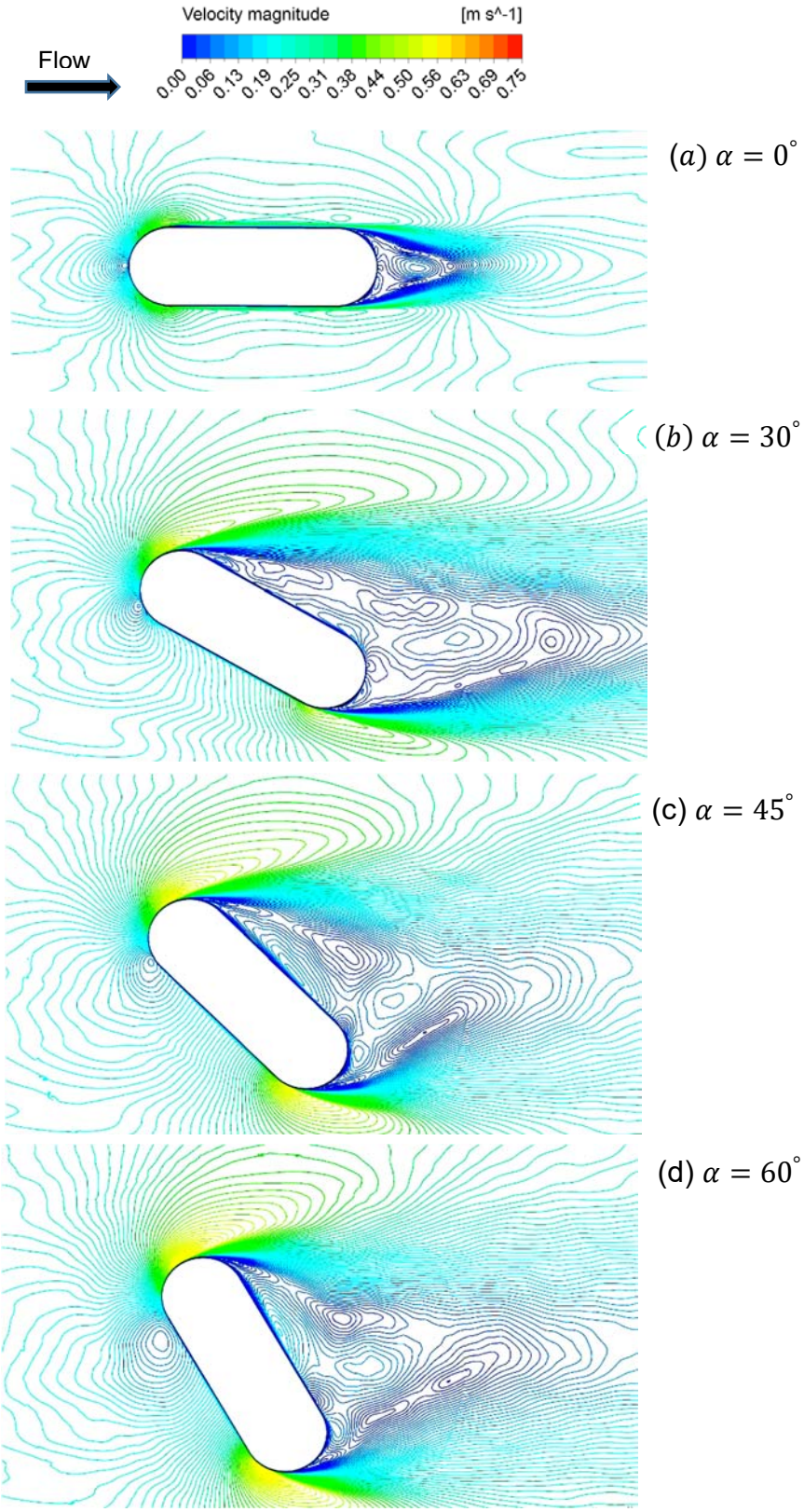

Figure 5.14: Time-averaged velocity distribution around oblong pier for different angles of attack and at a distance equal to y/H=0.0025 above the riverbed.

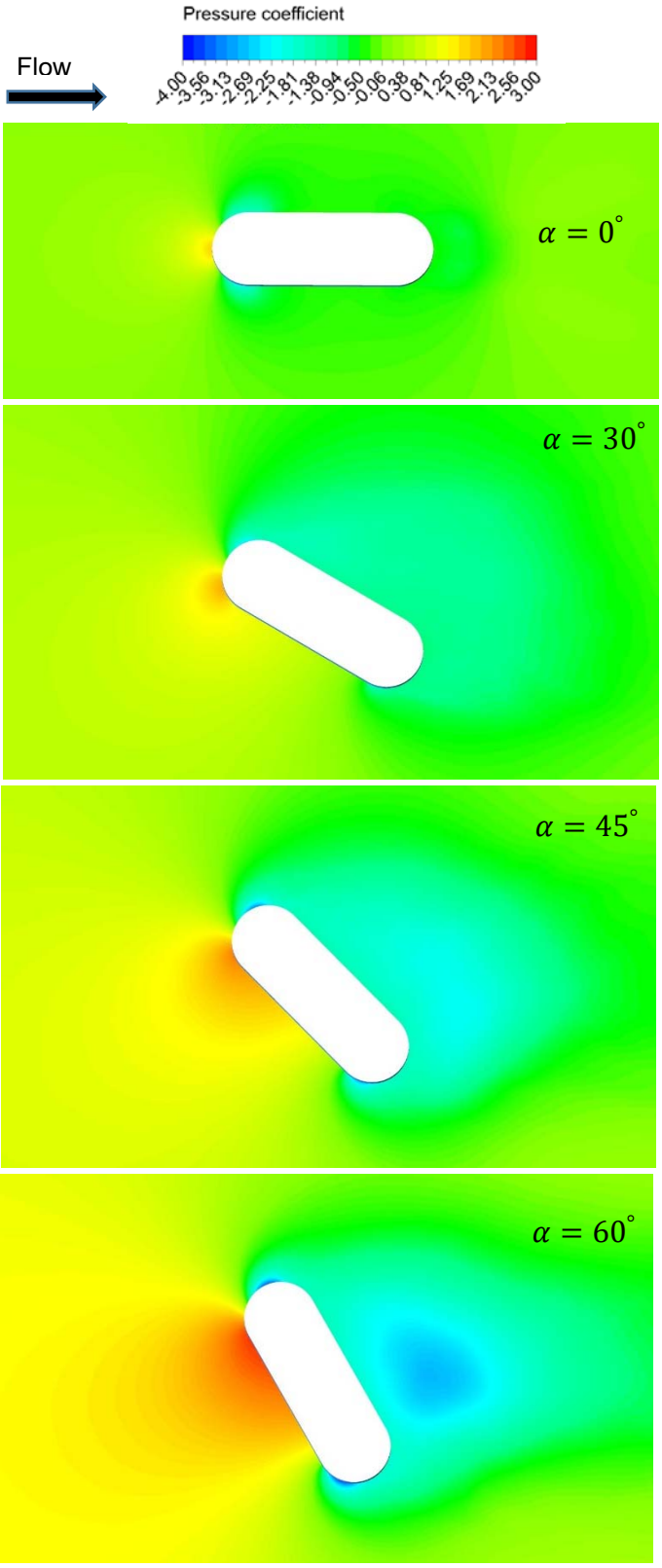

Figure 5.15: Mean pressure coefficient (C_p) around oblong pier subjected to different angles of attack and at a distance equal to y/H=0.0025 above the riverbed.

Figure 5.16 provides more detail of the structure and vortices in the near wake of the instantaneous flow fields. It shows the vertical vorticity behind the cylinder and located at two different levels from the riverbed (y/H=0.2 and 0.9). It can be observed that for all angles of attack, the near wake region is populated by roller vortices. The dynamics of the rollers have a significant effect on the bed shear stress and on the sediment transport behind the cylinder (Chang et al., 2013).

The density of these vortices behind the cylinder increases with angle of attack. This means, the capacity of vortices is relatively small in the case of $\alpha = 0^{\circ}$ compared to other angles of attack. From Figure 5.16, it can be observed, the coherent strength of these vortices decreases significantly close to the bed, which leads to reduced capacity to move the sediment beneath these vortices.

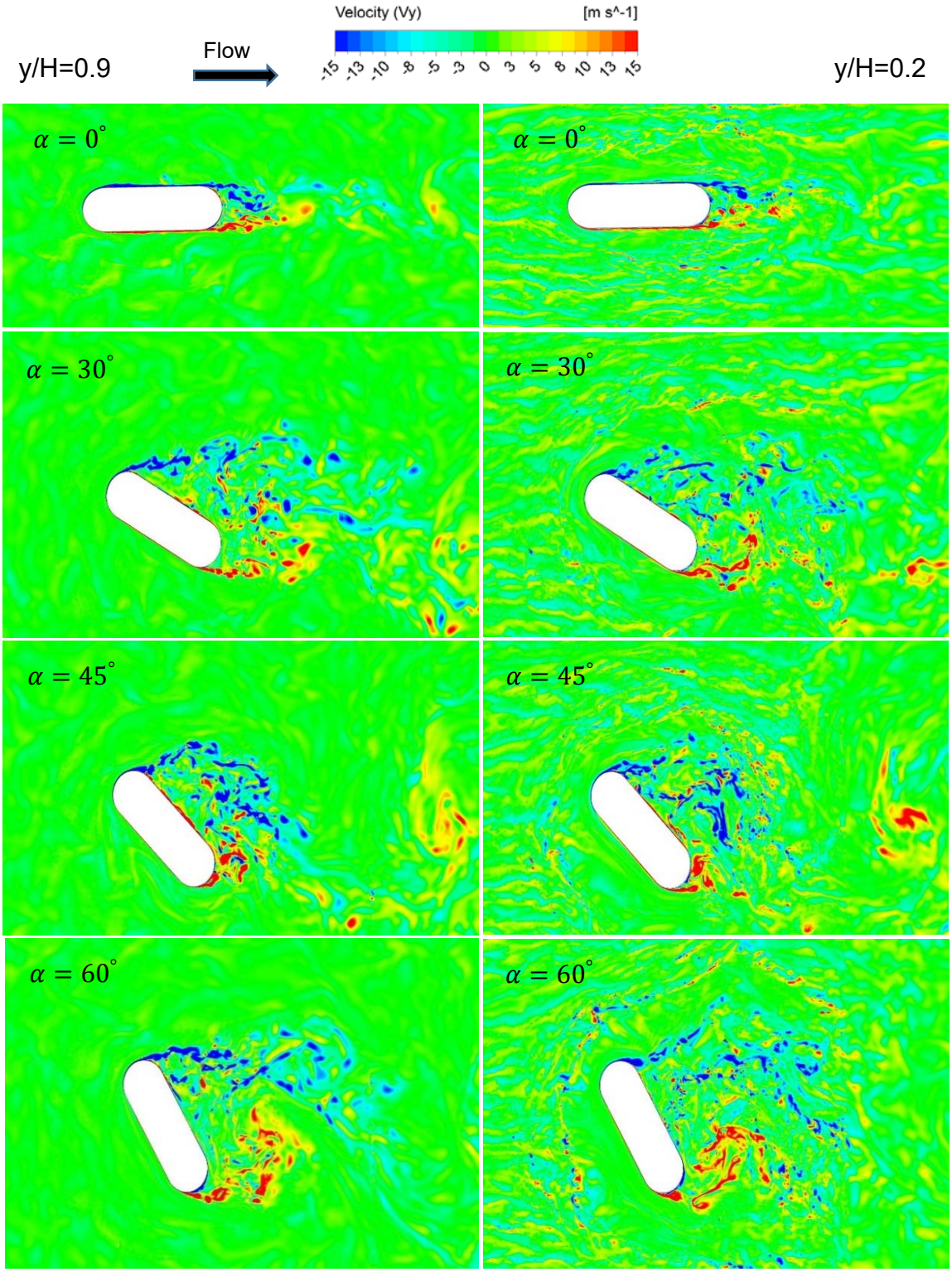

Figure 5.16: Plan-view of the instantaneous vertical vorticity around the oblong pier just before scour starts and subjected to different angles of attack and located at two different levels (y/H=0.2 and 0.9) from the bed of the channel.

5.2.2.3 Vortex shedding and Strouhal number

The vortex shedding in the wake region of the oblong cylinder is also investigated using LES. At angles of attack (α = 0°, 30°, 45° and 60°) periodic vortex shedding is predicted. Table 5.1 shows a summary of the calculated drag coefficient, C_d, and the vortex shedding parameters (shedding frequency, f_s, and Strouhal number, St) downstream of the oblong cylinder with respect to different angles of attack ranging from 0° to 60°. The vortex shedding frequency is computed using two different methods, the FFT and visualisation method. Figure 5.17 shows the power spectral analysis of the lift coefficient applied on the oblong pier in the Z-direction and at the free surface of the channel (y/H= 1.0) for different angles of attack. The velocity magnitude contour plots of Figure 5.18 illustrate the vortex structure over time for oblong cylinder located in a straight flow (α = 0°). It can be observed from this figure that the total simulation time corresponds to approximately one vortex cycle of flow pass around oblong pier and subject to angle of attack $\alpha = 0^{\circ}$ is 2.5 seconds (f_s=1/2.5=0.4Hz). The results for cases α = 30°, 45° and 60° were not included in this chapter because they are qualitatively like those for case $\alpha = 0^{\circ}$. The physical length scale that affects the shedding behind bridge piers is the projected width, W, along the direction normal to the approaching flow. Table 5.1 shows the predict values of Strouhal number for both methods with respect to the projected width. Also, the values of Strouhal number ($St = f_s W/U$) are increasing with the angle of attack. The fact that the Strouhal number of flow around oblong cylinder is strongly dependent on α provides further evidence to the complexity of the flow. The Strouhal number behind the oblong cylinder with

respect to the angle of attack of the incoming flow gives the same behaviour of the Strouhal number behind the rectangular cylinder (Chang et al., 2011).

As reported in Table 5.1, the FFT calculated frequencies show a small under-estimation of predicted shedding frequency compared with the visualisation method. The range of difference in these two methods gives values between 5 to18% (with the visualisation method always marginally larger). This may be due to the decay in the energy away from the peak using the FFT method being not very sharp, as shown in Figure 5.17.

Table 5.1: Summary of predicted drag coefficient, C_d, and downstream vortex shedding parameters for oblong cylinder using FFT method and visualisation method.

α	C_d	FFT method		Visualisation method		Difference between two methods
		f_s (HZ)	St	f_s (HZ)	St	
0°	0.615	0.335	0.193	0.400	0.230	16%
30°	1.269	0.180	0.243	0.220	0.296	18%
45°	1.896	0.165	0.270	0.182	0.298	9%
60°	2.047	0.165	0.294	0.174	0.310	5%

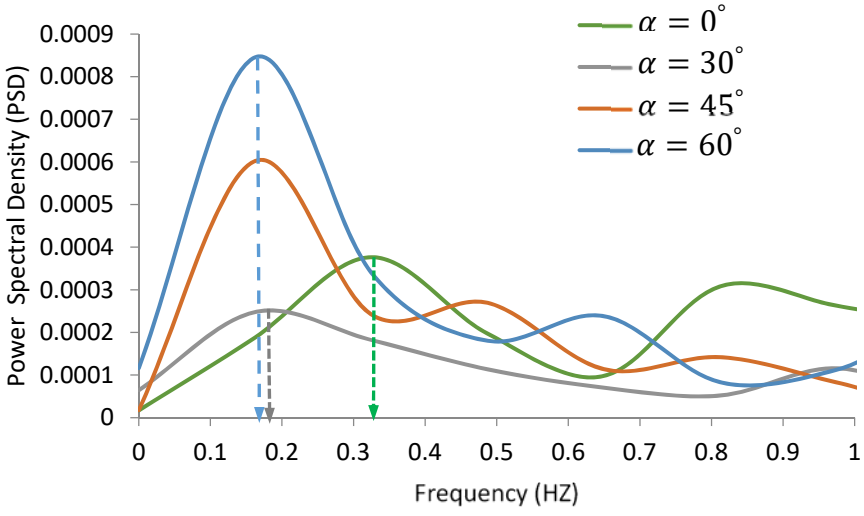

Figure 5.17: Spectral analysis of lift coefficient of oblong cylinder.

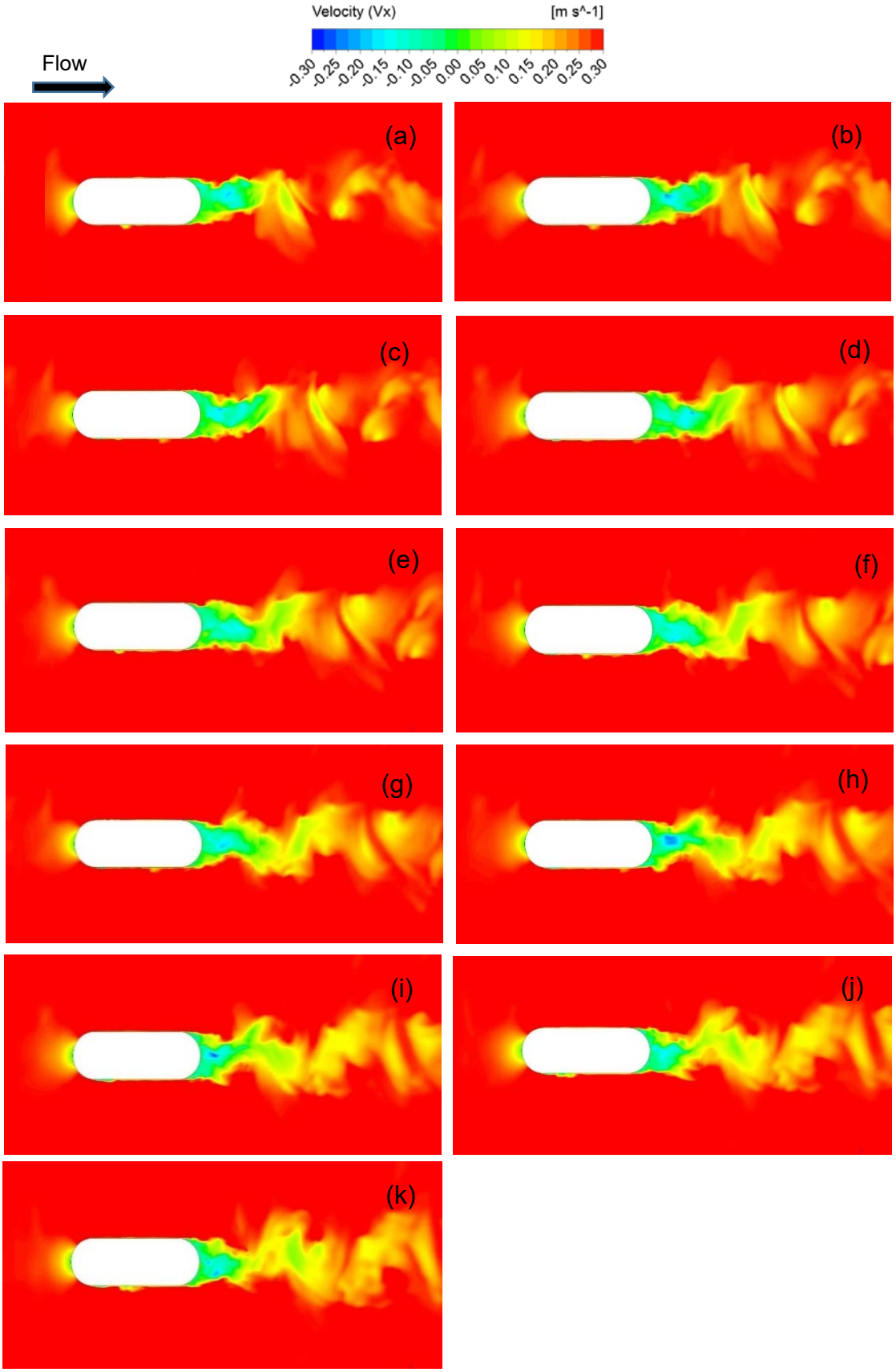

Figure 5.18: Velocity magnitude downstream of the oblong cylinder for angle of attack α = 0° at every 0.25 seconds.

5.2.2.4 Three-dimensional dynamics of the wake vortices

The Q-Criterion in Figure 5.19 is used to visualise the main coherent structures around the cylinder subjected to various angles of attack from approaching flow (α = 0°, 30°, 45° and 60°). It can be observed that (for all angles of attack) the region behind the cylinder is populated with wake vortices, and the density of these vortices increases with increase in the angle of attack. It is interesting to note that with LES analysis there are many vortices having an inclined axis of rotation with the riverbed and when these vortices are close to the bed it can significantly affect the sediment movement.

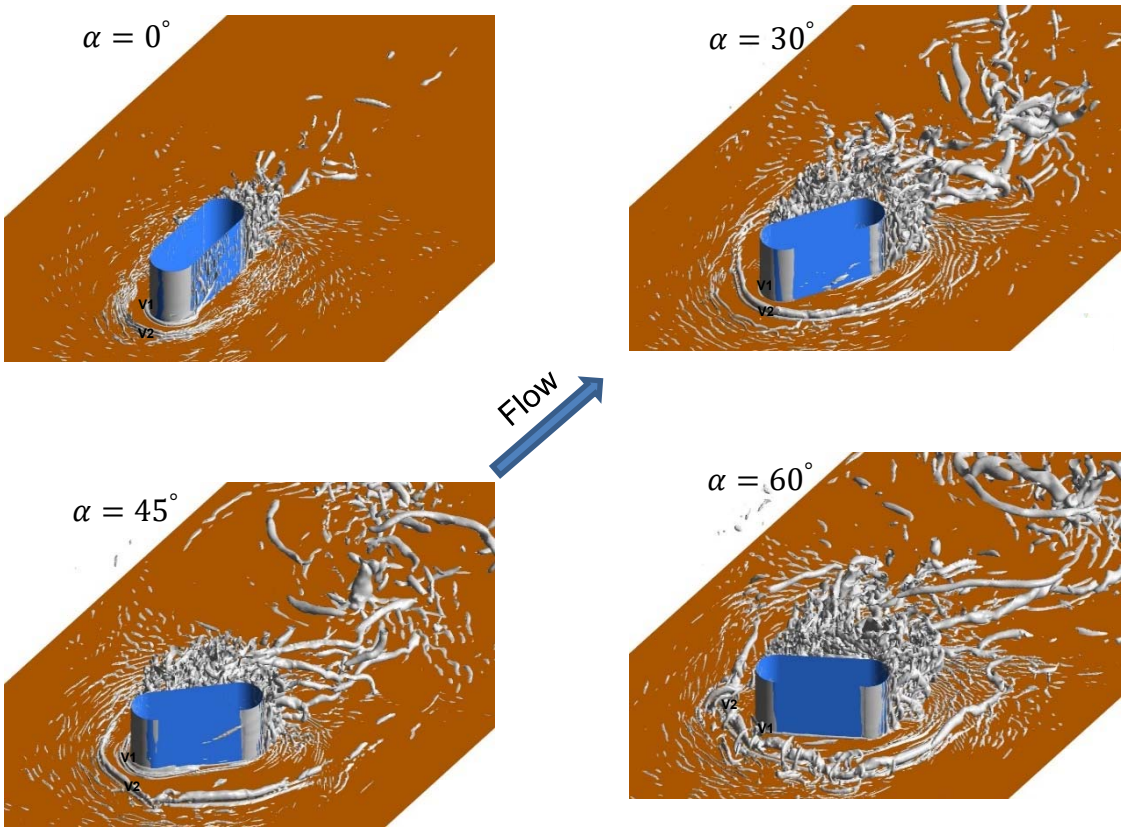

Figure 5.19: Visualisation of the main vertical structures around the oblong cylinder in the instantaneous flow for different angles of attack α = 0°, 30°, 45° and 60°.

5.2.2.5 Turbulent kinetic energy

Figure 5.20 shows the turbulent kinetic energy (TKE) in a vertical plane cutting through the cylinder and parallel to the incoming flow. It can be observed that the maximum value of the TKE in case of $\alpha = 0^{\circ}$(0.0028 m^2/s^2) is a little bit larger than that predicted in case of $\alpha = 30^{\circ}$(0.0024 m^2/s^2). These results are due to the fact that the vertical plane of study coincides with the axis of the cylinder in case of $\alpha = 0^{\circ}$. This produces a large TKE due to strong interaction of the vortices from the lift side and the right side of the cylinder as shown in Figure 5.16. As the angle of attack increases, the TKE within its core increases strongly. A comparison of the TKE distribution in Figure 5.20 shows that the region occupied by the TKE behind the cylinder increases with α, and the amplification of the maximum value of the TKE in case of $\alpha = 60^{\circ}$ (0.01 m^2/s^2) is about four times larger than the predicted value in the case of $\alpha = 30^{\circ}$.

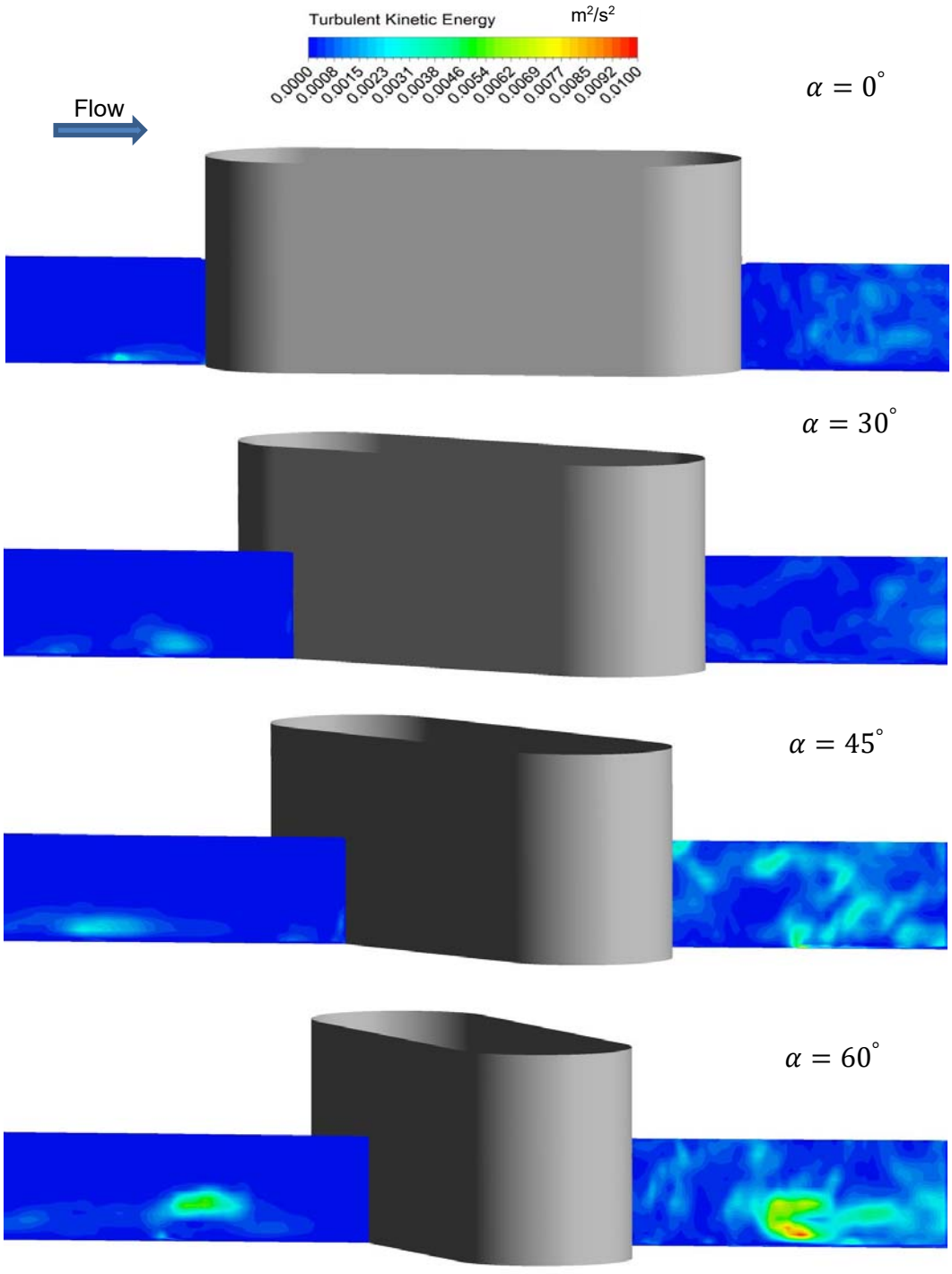

Figure 5.20: Instantaneous turbulent kinetic energy in the symmetry plane parallel to the flow.

5.2.2.6 Horseshoe vortex system

The adverse pressure gradients and the down-flow, produced due to the deceleration of the incoming flow as it approaches the cylinder, induces the formation of a system of unsteady necklace vortices at all angles of attack. These vortices are visualised in Figure 5.21 which shows the instantaneous velocity distribution in the symmetry plane upstream of the cylinder. It can be observed at most times in the flow, the main vortex (V2) and the vortex close to the cylinder edge (V1) are more stable vortices around the cylinder for all cases of α, in addition to many unstable vortices that appears behind V2.

The horseshoe vortex system upstream of the cylinder changes with respect to the angle of attack as shown in Figure 5.19. It shows that the core of the main necklace vortices and the length of their legs on both sides of the cylinder increase with the angle of attack. For example, the length of the leg of the main necklace vortices in case of $\alpha = 0^{\circ}$ (starting from the edge of the front face of the cylinder) is equal to about 0.25L (where L is the length of the pier in the streamwise direction). This distance increase to about 1L in case of $\alpha = 30^{\circ}$, to about 1.3L in case of $\alpha = 45^{\circ}$, and to about 1.6L in case of $\alpha = 60^{\circ}$. Thus, when $\alpha = 60^{\circ}$, the length of the main necklace vortex increases to about six times that for $\alpha = 0^{\circ}$. Therefore, with increasing angle of attack, the main necklace vortices may have a significant role not only on the maximum scour depth, but also on the scour hole on both sides of the cylinder. Figure 5.20 shows the TKE in the symmetry plane upstream of the cylinder. The area of the TKE region increases with angle of attack. The peak value of the TKE in case $\alpha = 0^{\circ}$ (0.004 m^2/s^2) is twice as large compared with the predicted peak vale of

TKE in case $\alpha = 30^{\circ}$ (0.002 m^2/s^2). This is because the plane of study (which passes through the symmetric axis of the cylinder) in the case of $\alpha = 0^{\circ}$ induce a very strong downflow in front of the cylinder and thus the higher TKE. A comparison of the amplification factor of the peak value of the TKE with the angle of attack found that in case of $\alpha = 60^{\circ}$ the maximum value of the TKE (0.006 m^2/s^2) is greater by three times when compared with the case of $\alpha = 30^{\circ}$, and about 2 times when compared with the case of $\alpha = 45^{\circ}$(0.003 m^2/s^2).

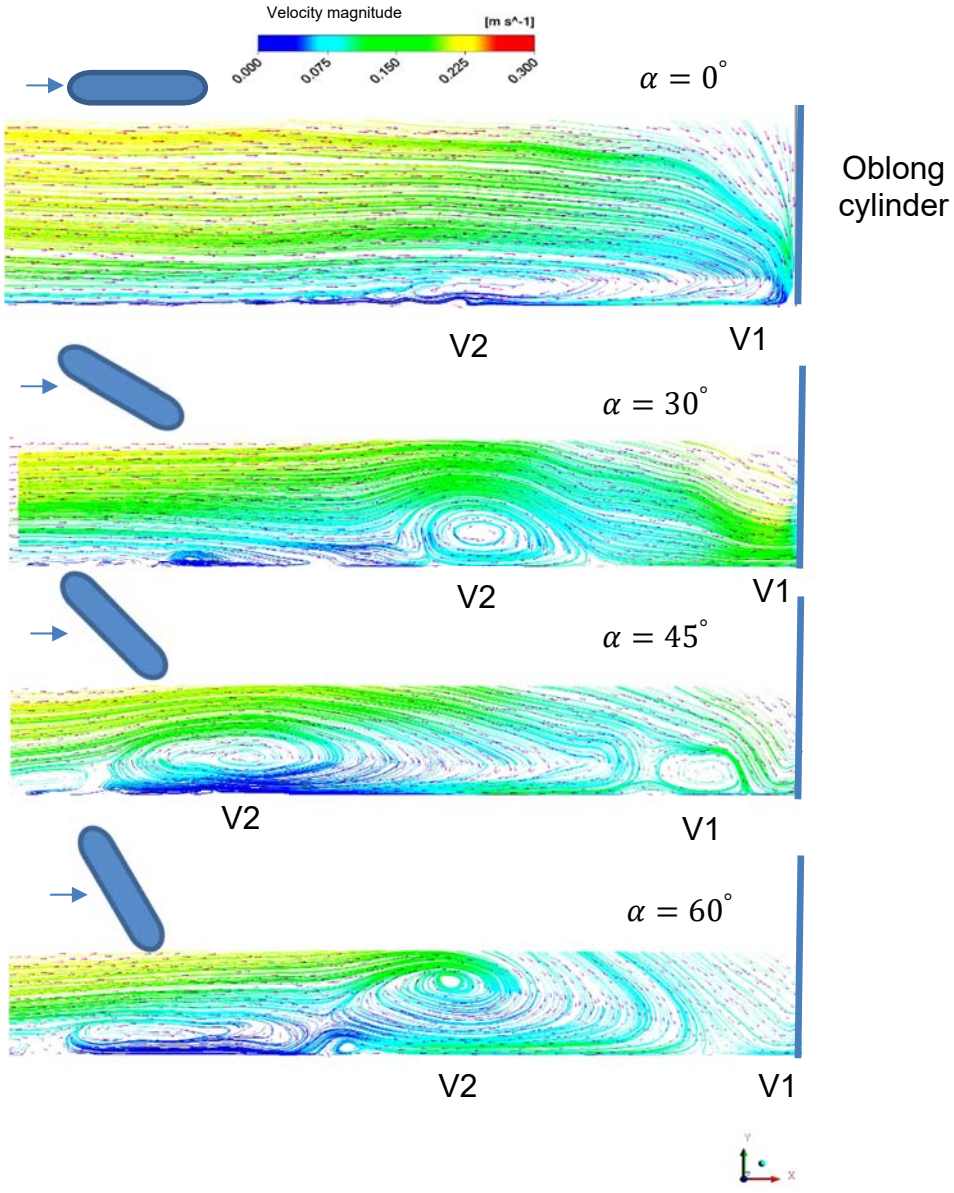

Figure 5.21: Streamlines of instantaneous velocity distribution upstream of the cylinder with different angles of attack.

5.2.2.7 Bed friction coefficient

Bed friction coefficient (C_f) is a non-dimensional parameter defined as the ratio of the wall shear stress to the reference dynamic pressure. It's given as:

$$C_f = \frac{\tau_\omega}{0.5\rho\, U^2} \quad 5.1$$

where τ_ω the wall shear stress, and ρ, U are the reference density and reference velocity respectively.

In the following discussion, the scoured area will be defined as the $C_f > C_{f\,critical}$, where $C_{f\,critical}$ is the critical bed friction coefficient equal to 0.006. $C_{f\,critical}$ is computed by applying the critical shear stress (0.2 N/mm^2) for sediment with mean diameter d_{50}=0.365 mm into the above equation.

It can be seen from Figure 5.21 that the area around the cylinder for all angles of attack and greater than 0.006 is subject to the sediment erosion. Figure 5.22 shows the maximum mean bed friction coefficient $C_{f\,max.}$ increases with angle of attack, $C_{f\,max.}$ = 0.027, 0.037, 0.04 and 0.046 for $\alpha = 0^\circ$, 30°, 45° and 60° respectively, these predicted results suggests to the maximum scour depth increase with the angle of attack.

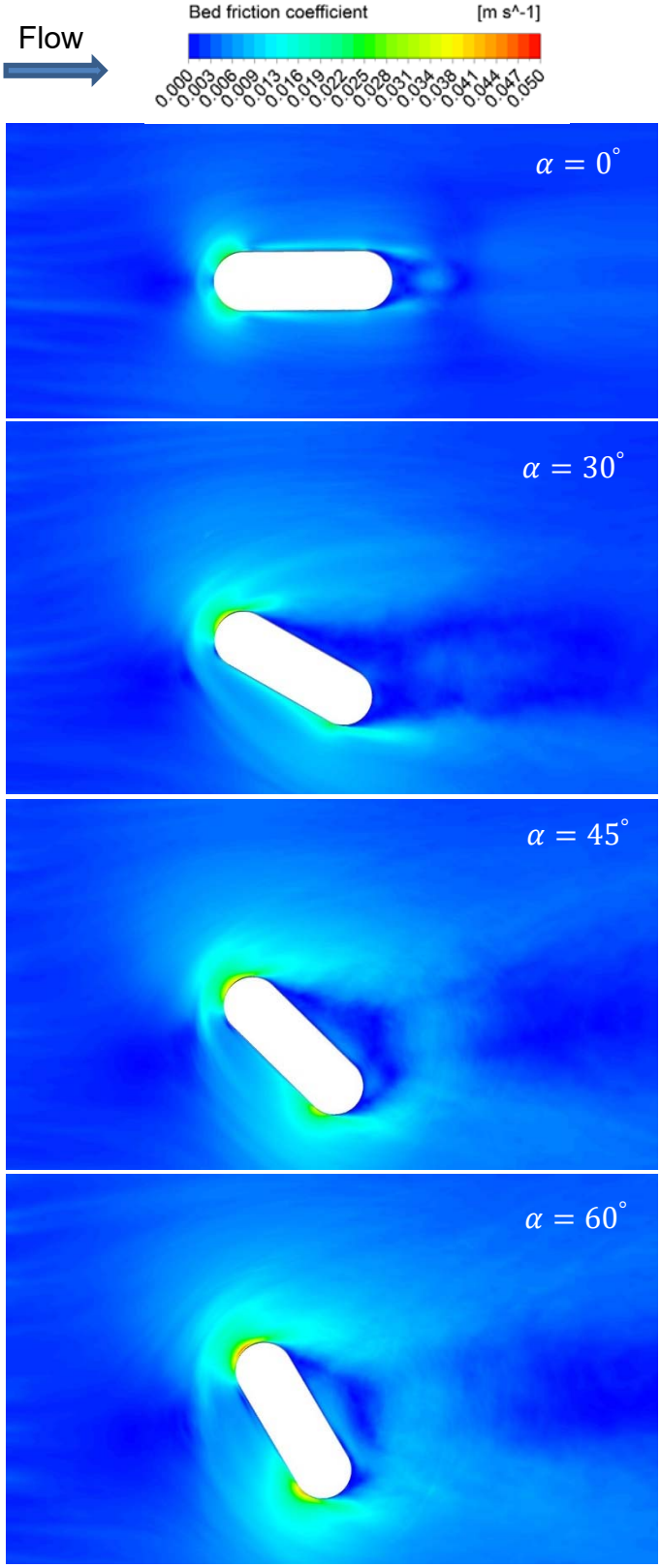

Figure 5.22: Mean bed friction coefficient around oblong pier with different angles of attack.

5.2.2.8 Effect of the angle of attack on the maximum scour depth and sediment transport rate

Figure 5.23 shows the simulated topographic contours for the local scour around the oblong bridge pier, which is subject to different angles of attacks, after 200 seconds of flow. This figure provides additional information about the location of the maximum scour depth and the scour shape around the oblong pier.

Figure 5.24 shows the scour parameters (i.e., the maximum scour depth, and the amount of the sediment transport from the scour hole) around the oblong cylinder which is subjected to different angles of attack ($\alpha = 30^{\circ}, 45^{\circ}$and 60°). Figures 5.24a and 5.24b demonstrates the angle of attack has a significant effect on the value and the rate of maximum scour depth around the oblong bridge pier.

Although the maximum scour depth in the case of circular cylinder is greater than that when compared with the maximum scour depth in the case of oblong cylinder which is subjected to a direct flow ($\alpha = 0^{\circ}$) as shown in Figure 5.9. The maximum scour depth in the case of oblong cylinder becomes greater than in case of circular cylinder when the approaching flow is inclined such as in the river bend. From Figure 5.24a, the maximum scour depth around the bridge pier increases to about three times when the angle of attack increases to 60°. The volume of sediment removed from scour hole is a further indicator that the angle of attack has a significant effect on the scour shape around the bridge pier as well as the sediment erosion rate.

A comparison for sediment removed from scour hole around the oblong pier has been undertaken for different angles of attack. As expected it is found that

the volume of removed sediment from the scour hole increases with angle of attack as shown in Figure 5.24c. After 150 seconds, the volume of the sediment removed from the scour hole appears to be constant for all angles of attack, and their values are about 5, 9, and 15 times in case of $\alpha = 30^{\circ}, 45^{\circ} \text{ and } 60^{\circ}$ respectively, when compared with the volume of sediment removed from the scour hole around the oblong cylinder with $\alpha = 0^{\circ}$ as shown in Figure 5.24d.

Comparing the amplification of the predicted maximum scour depth with respect to the angle of attack after 200 seconds, shows the maximum scour rate is 3.2 time for the case of $\alpha = 60^{\circ}$, 2.8 times for the case of $\alpha = 45^{\circ}$, and 2.4 times for the case of $\alpha = 30^{\circ}$ with respect to the predicted maximum scour depth in the case of $\alpha = 0^{\circ}$ as shown in Figure 5.24b. These predicted results can be compared with the angle of attack correction factor equations, which are proposed from previous numerical studies and discussed in Chapter 2, as shown in Figure 5.25. In which the predicted effect of the angle of attack of the approaching flow on the maximum scour depth around the oblong bridge pier with an aspect ratio equal to three, is compared with Equations 2.7 and 2.8.

Equation 2.7, which was proposed by Briaud et al. (2004), whose results are based on the collected experimental data and numerical simulation for rectangular cylinder. And Tao and Yu (2014) who proposed Equation 2.8 based the research using a URANS model with *k*-*ω* turbulence model for the flow around a rounded nose cylinder mounted on a flatbed with aspect ratios of 2.0 and 4.0.

The angle of attack amplification factors which are predicted in this study are slightly larger than the resulting amplification factors which are predicted from Equation 2.8 (increase ranging from 9-13%). The difference may be because of the bimodal oscillation phenomena of the horseshoe vortex system on the scour evolution, which is clearly captured when the LES is used to simulate the flow around an obstacle. In contrast to the URANS model which has been unable to capture this phenomenon. Therefore, it is proposed that to ensure a more accurate expression for calculating the angle of attack correction factor, a justification is made for the exponent index in Equation 2.8 (which is equal to 0.9 in Tao and Yu (2014) study) can be adapted (updated) based on findings in this investigation.

To obtain an appropriate exponent which fits best for the exponent index Equation 2.8 using the LES results is found to be 1.015 for aspect ratio $L/b = 3.0$ as shown below:

$$K_\alpha = \left(\frac{L}{b} sin\,\alpha + cos\,\alpha\right)^{1.015} \quad 5.2$$

The hypothesis suggested in this study was based on LES, for calculating the angle of attack correction factor for oblong bridge $L/b = 3.0$. It's more accurate than the previous equation, which is depended on the URANS model, but to make this hypothesis more general and applicable in the engineering application its need to be tested against a range of L/b.

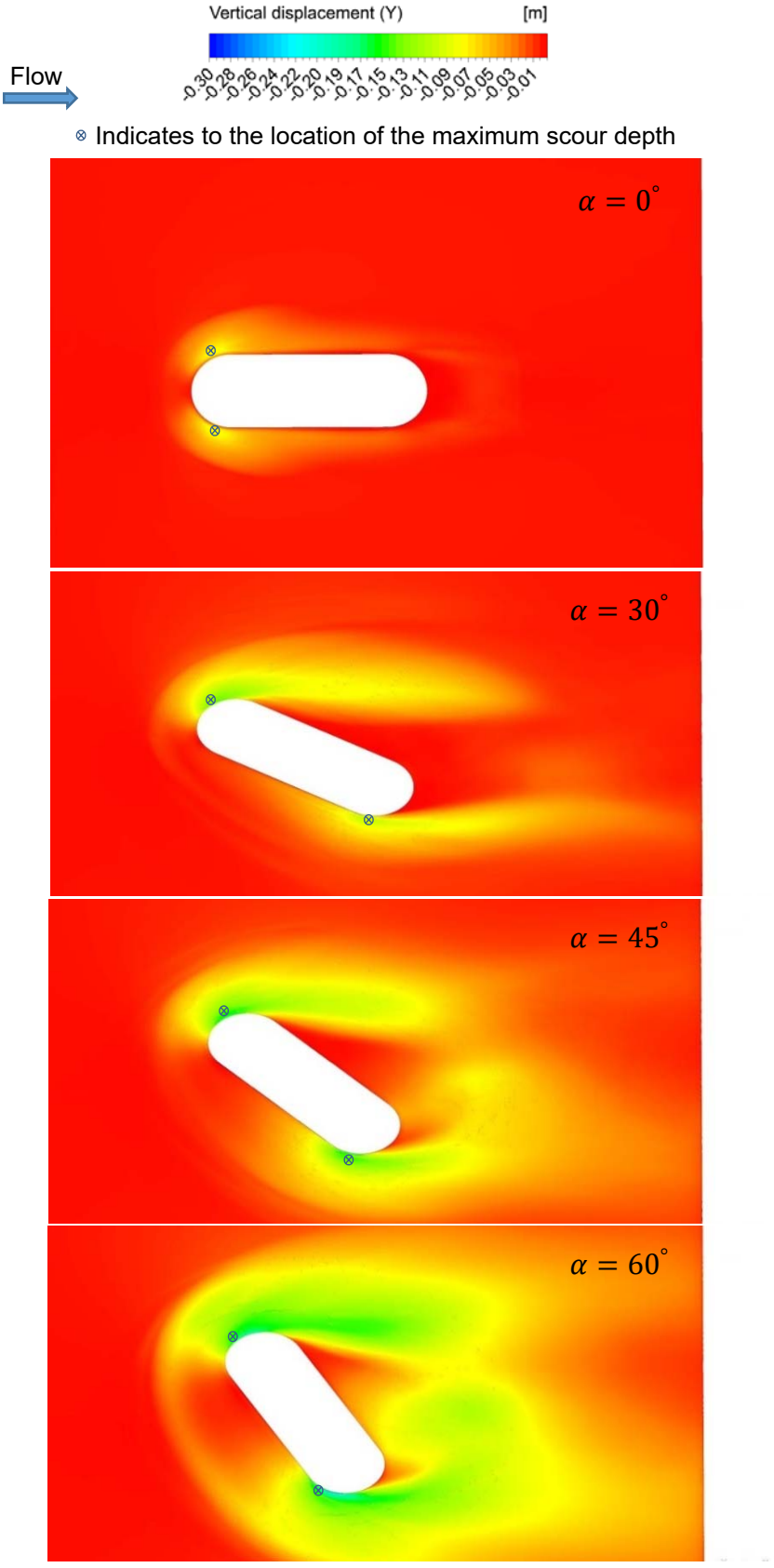

Figure 5.23: Maximum scour depth and scour pattern around an oblong bridge pier with different angles of attack after 200 seconds of flow

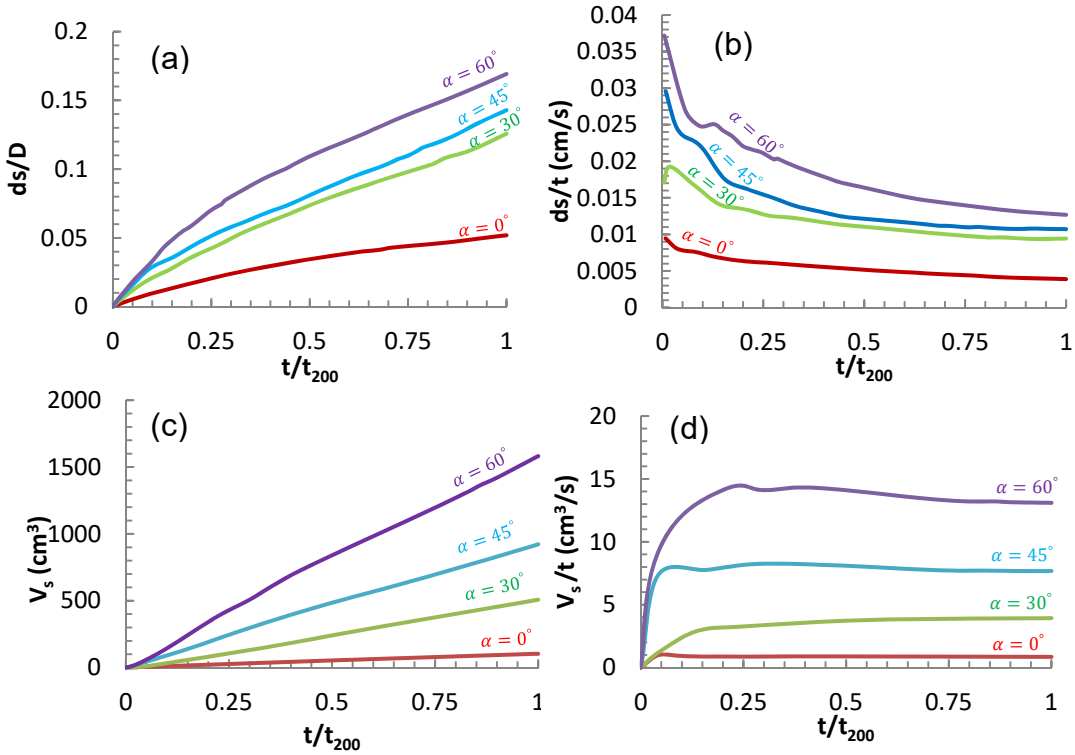

Figure 5.24: Scour measurements around an oblong bridge pier subjected to different angles of attack: (a and b) value and rate of the maximum scour depth, (c and d) amount and rate of the removed sediment from scour hole.

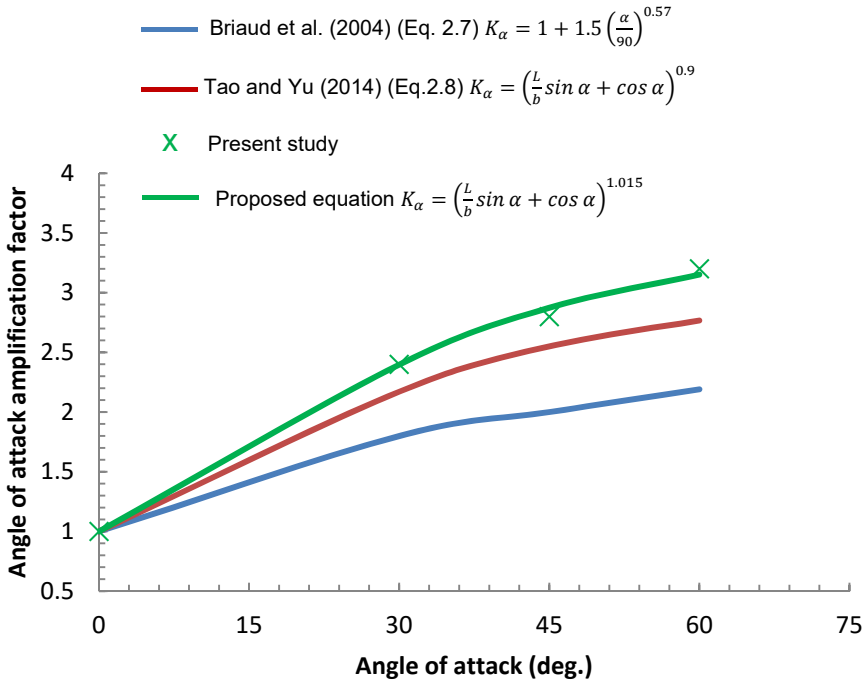

Figure 5.25: The amplification factor for different angles of attack and corresponding fitting curves.

5.3 Summary and findings

This chapter provided a description of the main characteristics of the flow field and turbulent coherent structures around an oblong bridge pier at different angles of attack (0° to 60°). A study on the effect of these coherent structures on the sediment erosion around bridge pier in the initial stage of the scour process (200 seconds) using LES simulation and dynamic mesh technique had been conducted. In general, the predictions of the study show that the pier shape and the angle of attack of the approaching flow have a very significant effect on the scour pattern and maximum scour depth around the bridge pier.

From the results presented in this chapter a modified equation is proposed to compute the angle of attack correction factor in case of oblong bridge piers. This equation adapts previous work and considers the results from LES predictions that have shown to be more reliable in predicting the complex flow behaviour to determine the scour rates. It is recommended that this adopted model is used by engineers when designing oblong shape piers. Since this equation depends on a high resolving technique (LES) which has the capability to capture most flow features around the bridge pier during scour evolution, in contrast with the URANS model (k-ω) which was used to predict the previous equation proposed by Tao and Yu (2014) .

The conclusions from this work are divided into two parts; the first is based on the comparison between the oblong and the circular bridge pier. The predicted results demonstrated that the down-flow in the upstream face of the circular pier is greater as compared to the case of oblong pier. These differences in the down-flow close to the cylinder are seen when studying the

approaching vertical velocity in the three co-ordinate directions (longitudinal, vertical, and transverse). The result is a higher bed shear stress and a higher risk of scour. The scour parameters investigated in this study shows that:

- The increase in the maximum scour depth in case of circular pier is about 24% larger than when compared with the maximum scour depth oblong pier shape.
- The total sediment removed from the scour hole is about twice in the case of circular bridge pier when compared with the oblong pier (for cases having the same width).
- The rate of the sediment transported from the scour hole for both cylinder shapes (the circular and the oblong cylinder) seems to be constant after a certain time (in this study is about 150 seconds).

As noted in the literature, it is the circular shape of the bridge pier that had higher risk of scouring than the oblong shape, when they both located in a river with direct flow(Guemou et al., 2016).

The second part is related to the effect of the angle of attack of the approaching flow on the flow field and scour pattern around the oblong bridge pier. The predicted results for the mean bed shear stress show an increase in the τ_{max} in case of $\alpha = 60^{\circ}$ is double when compared with τ_{max} in the case of $\alpha = 0^{\circ}$. In addition to the mean bed shear stress, the effect of the scour hole on the flow field around the bridge pier is also discussed. In the case of turbulent coherent structures around oblong bridge pier there are many differences observed with increase of angle of attack, for example:

- The density of the vortices behind the cylinder increases with the angle of attack,
- The length of the leg of the main vortex on the both sides of the cylinder increases up to 6 times in case of $\alpha = 60^{\circ}$ when compared with the length of the leg of the main vortex in case of $\alpha = 0^{\circ}$.
- In the case of vortex shedding parameters, the drag force and the Strouhal number are also observed to increase with the angle of attack.
- The TKE is also observed to increase with angle of attack by up to 4 times and 3 times downstream and upstream of the cylinder respectively in case of $\alpha = 60^{\circ}$ when compared with the TKE in the case of $\alpha = 30^{\circ}$.

Therefore, scour shape and the maximum rate of erosion around cylinder is said to be significantly affected by the angle of attack. Specifically, if:

- The maximum scour depth increases to about 3 times for the case of $\alpha = 60^{\circ}$ with respect to the predicted maximum scour depth in case of $\alpha = 0^{\circ}$.
- The volume of the sediment which transported from the scour hole around the bridge pier in case of $\alpha = 60^{\circ}$ (1580 cm^3) is about 15 times larger than the volume of sediment which removed from the scour hole in the case $\alpha = 0^{\circ}$(103 cm^3).
- The rate of the sediment transported from the scour hole for the oblong cylinder appears to be constant for all angles of attack after a certain time of flow (about 150 seconds).

Chapter 6

Conclusions and Further Work

6.1 Conclusions

This chapter presents an overview of the main conclusions of the research and highlights the significance of the study. Furthermore, this chapter summaries the findings of the previous chapters and relates them back to the aims and objectives set out at the start of the study. In the final part of this chapter, a scope of subjects that could be considered as future work, or additions of this study, is presented.

The scour processes and sediment transport around hydraulic structures are significantly influenced by the large scale coherent structures that produce the system of horseshoe vortices upstream of the pier, and wake vortices downstream of the pier. Therefore, several issues regarding the transport of sediment by coherent structures in turbulent flows have been addressed in this study. Particularly, the effects of the turbulent horseshoe vortex system on sediment transport and clear-water scour near hydraulic structures have been studied.

The methodology used in this research allowed a better understanding of the structure of the horseshoe vortex system than previous works, and predicted results such as the bed shear stress inside the scour region with good comparisons with the experimental studies. The novel approach in this

thesis is the use of large eddy simulation (LES), together with a dynamic mesh technique, to simulate the coherent structures around bridge piers and the effect on scour evolution. This has improved the understanding with higher accuracy and details.

6.1.1 Key conclusion

The novel contribution of this research is a modified equation to compute the angle of attack correction factor in the case of oblong bridge piers. This equation adopts previous investigations and considers the results from the LES predictions that has shown to reliably predict the complex flow behaviours which are important in determining scour rates. This equation depends on the high resolving LES technique which has the capability to capture most flow features around the bridge pier during scour evolution, in contrast with the URANS model (k-ω) which was used to in previous version of the equation proposed by Tao and Yu (2014).

The main conclusions established from the findings given in the chapters above, are as follows:

6.1.2 Circular cylinder mounted in flatbed

A simulation with the experimental configuration of Dargahi (1989) for turbulent channel flow past a circular cylinder mounted in a flatbed has been undertaken using LES approach. The predicted results which were compared with those obtained from URANS models (i.e., k-ε standard and k-ω SST) with the experimental data. It verified the reliability and feasibility of the LES to simulate the turbulent flow around obstacles mounted on a flatbed river channel.

The following was concluded:

- The LES model can capture the full set of horseshoe vortices upstream of the cylinder that were observed in the Dargahi (1989) experimental study. In contrasts with the URANS models which only show a single vortex upstream of the cylinder.
- In the case of comparing the time-averaged predicted results around the circular cylinder (the velocity distribution profile downstream of the cylinder, the bed pressure coefficient and the bed shear stress), the results from URANS and LES models are in a reasonable agreement with the experiments. However, the LES predictions are in closer agreement with the experiments.
- The LES model (with grids of $24x10^6$ and $12x10^6$ cells) gives close agreement to the measured experimental values (the Strouhal number and the drag coefficient values) for the flow passing around the circular cylinder.

6.1.3 Circular cylinder in erodible bed

The coupling between LES and the dynamic mesh technique has been undertaken to study the coherent structures around a circular bridge pier in the initial stage of scour evolution. The approach produces good predictions for qualitative and quantitative characteristics observed by Dargahi (1990); including:

- The maximum scour depth and its location from the symmetry plane.
- The scour pattern around the circular cylinder.

Furthermore, the LES combined with an updating dynamic mesh technique provides good estimations for the behaviour of the coherent structures around a bridge pier during scour development. By studying the transient behaviour for the horseshoe vortex system upstream of the cylinder during the scour process evolution using LES, it is concluded that the main vortex has the bimodal oscillation phenomenon which increases the ability of these vortices to remove sediment around the cylinder.

6.1.4 Oblong bridge pier located in a river bend

After the validation of the methodology proposed in the study for experimental and numerical studies from the literatures; the effects of the pier shape, the angle of attack on the relevant time-averaged and turbulence statistics of the flow (and therefore on the scour pattern around bridge pier) were investigated. The predicted results, shows a significant effect of the angle of attack, on both the complexity of the flow as well as on the scour pattern and maximum scour depth around the bridge pier.

This study is relevant in understanding the erosion mechanisms around oblong bridge piers constructed on a river bend. The current investigations consider the most relevant range of angles of attack ($\alpha = 0^{\circ}\text{to}\,60^{\circ}$) on the design of the oblong pier which is one of the most common shapes of piers used to support bridges.

Depending on the comparison between the oblong and circular bridge piers the predicted results show:

- There is a reduction in the maximum scour depth of about 24% in the case of oblong bridge piers as compared to circular piers (both having the same width).
- There is a reduction in the quantity of the sediment removed from the scour hole around oblong piers of about the half of the quantity of the sediment removed from the scour hole in the case of circular piers (of the same width).

The scour shape and the maximum rate of erosion around the oblong cylinder are significantly affected by the angle of attack, as shown:

- The maximum scour depth increases to about 3 times when the angle of attack α increases from 0° to 60°.
- The quantity of the sediment which is transported from the scour hole around the bridge increases about 15 times as the angle of attack α increases from 0° to 60°.

These predicted results can be used to determine the regions where strengthening with riprap is required, which depends on the expected maximum angle of attack and on the location of the bridge pier in the river bend.

6.2 Further Work

The undertaken research was designed and based on the techniques according to the time at hand. Nevertheless, certain parts of the research would benefit by applying additional and/or alternative techniques.

For example, simulations modelling of the scour around bridge piers by coupling eddy-resolving methods, especially LES, with advanced sediment transport models (two-phase flow models which treat the sediment as a

separate phase), would be something interesting to look at. Such models that simultaneously couple the fluid and particle phases are the future trend in the scour process simulation and its applications. However, due to high demand on computational resources, LES application is limited to the early stages of scour around piers in flow with a medium R_e (e.g. 3.9×10^4). In future, it's expected to see more research on scour at various stages of scour and in flow with higher R_e which are closer to real life river conditions.

Further studies should be carried out on the effect of geometry on bridge piers. For example, flow and scour patterns around a group of piers with different configurations, such as the distance between the piers. Due to very limited experimental studies at a laboratory scale, advanced numerical simulations are expected to provide more details on the mechanism of scour around complex structures and thus help to improve the design of bridge foundations and scour counter measures.

References

Adhikary, B., Majumdar, P. & Kostic, M. CFD simulation of open channel flooding flows and scouring around bridge structures. Proceedings of the 6th WSEAS International Conference on FLUID MECHANICS (FLUIDS'09), 2009.

Ahmed, F. & Rajaratnam, N. 1998. Flow around bridge piers. *Journal of Hydraulic Engineering,* 124**,** 288-300.

Akilli, H., Akar, A. & Karakus, C. 2004. Flow characteristics of circular cylinders arranged side-by-side in shallow water. *Flow measurement and instrumentation,* 15**,** 187-197.

Aksoy, A. O., Bombar, G., Arkis, T. & Guney, M. S. 2017. Study of the time-dependent clear water scour around circular bridge piers. *Journal of Hydrology and Hydromechanics,* 65**,** 26-34.

Ali, K. H. & Karim, O. 2002. Simulation of flow around piers. *Journal of Hydraulic Research,* 40**,** 161-174.

Apsildis, N., Khosronejad, A., Sotiropoulos, F., Dancey, C. L. & Diplas, P 2012. Physical and numerical modeling of the turbulent flow field *ICSE6. Paris*.

Baranya, S., Olsen, N. R. B., Stoesser, T. & Sturm, T. W. 2014. A nested grid based computational fluid dynamics model to predict bridge pier scour. *Proceedings of the Institution of Civil Engineers,* 167**,** 259.

Batchelor, G. 1967. An Introduction to Fluid Dynamics Cambridge Univ. Press.

Bennetts, T. A. 2002. *Local scour around bridge piers under steady and unsteady flow conditions.* University of Herfordshire.

Breusers, H., Nicollet, G. & Shen, H. 1977. Local scour around cylindrical piers. *Journal of Hydraulic Research,* 15**,** 211-252.

Briaud, J.-L., Chen, H.-C., Li, Y. & Nurtjahyo, P. 2004. SRICOS-EFA method for complex piers in fine-grained soils. *Journal of Geotechnical and Geoenvironmental Engineering,* 130**,** 1180-1191.

Briaud, J.-L., Gardoni, P. & Yao, C. 2013. Statistical, risk, and reliability analyses of bridge scour. *Journal of Geotechnical and Geoenvironmental Engineering,* 140**,** 04013011.

Briaud, J.-L., Ting, F., Chen, H., Gudavalli, R., Kwak, K., Philogene, B., Han, S.-W., Perugu, S., Wei, G. & Nurtjahyo, P. 1999. SRICOS: Prediction of scour rate at bridge piers. *Texas Transportation Institute, The Texas A&M University, College Station, Texas, USA. Report***,** 2937-1.

Chabert, J. & Engeldinger, P. 1956. Study of scour around bridge piers. *Rep. Prepared for the Laboratoire National d'Hydraulique*.

Chang, W.-Y., Constantinescu, G., Lien, H.-C., Tsai, W.-F., Lai, J.-S. & Loh, C.-H. 2013. Flow structure around bridge piers of varying geometrical complexity. *Journal of Hydraulic Engineering,* 139**,** 812-826.

Chang, W., Constantinescu, G., Tsai, W. & Lien, H. 2011. Coherent structure dynamics and sediment erosion mechanisms around an in-stream rectangular cylinder at low and moderate angles of attack. *Water Resources Research,* 47.

Chien, N. 1999. *Mechanics of sediment transport.* Institute of Water Resources and Hydro-Power Research Translated under the guidance of John S. McNown Late Engineering College Dean, University of Kansas.

Choi, G., Ahn, C., Kim, K. & Ahn, S. The effect of approaching flow angles on the local scour at semi-circular piers. Stream Stability and Scour at Highway Bridges: Compendium of Stream Stability and Scour Papers Presented at Conferences Sponsored by the Water Resources Engineering (Hydraulics) Division of the American Society of Civil Engineers, 1995. ASCE, 173-173.

Choi, S. & Yang, W. Numerical simulations of 3-D flows around bridge piers. First International Conference on Scour of Foundations, 2002.

Dargahi, B. 1987. Flow field and local scouring around a pier. *Bulletin No. TRITA-VBI,* 137.

Dargahi, B. 1989. The turbulent flow field around a circular cylinder. *Experiments in Fluids,* 8**,** 1-12.

Dargahi, B. 1990. Controlling mechanism of local scouring. *Journal of Hydraulic Engineering,* 116**,** 1197-1214.

Das, S., Das, R. & Mazumdar, A. 2013. Circulation characteristics of horseshoe vortex in scour region around circular piers. *Water Science and Engineering,* 6**,** 59-77.

Debnath, K. & Chaudhuri, S. 2012. Local scour around non-circular piers in clay–sand mixed cohesive sediment beds. *Engineering Geology,* 151**,** 1-14.

Devenport, W. J. & Simpson, R. L. 1990. Time-dependent and time-averaged turbulence structure near the nose of a wing-body junction. *Journal of Fluid Mechanics,* 210**,** 23-55.

Engelund, F. & Fredsøe, J. 1976. A sediment transport model for straight alluvial channels. *Hydrology Research,* 7**,** 293-306.

Escauriaza, C. 2008. *Three-dimensional unsteady modeling of clear-water scour in the vicinity of hydraulic structures: Lagrangian and Eulerian perspectives*, ProQuest.

Escauriaza, C. & Sotiropoulos, F. 2011. Initial stages of erosion and bed form development in a turbulent flow around a cylindrical pier. *Journal of Geophysical Research: Earth Surface,* 116.

Ettema, R., Kirkil, G. & Muste, M. 2006. Similitude of large-scale turbulence in experiments on local scour at cylinders. *Journal of Hydraulic Engineering,* 132**,** 33-40.

Fael, C., Lança, R. & Cardoso, A. 2016. Effect of pier shape and pier alignment on the equilibrium scour depth at single piers. *International Journal of Sediment Research,* 31**,** 244-250.

Fluent, A. 2009. 12.0 UDF manual. *Ansys Inc*.

Geography.unt.edu. 2017. *Stream Erosion* [Online]. Available: http://geography.unt.edu/~williams/geog_3350/examreviews/stream_erosion.htm [Accessed 31-01-2017.

Geol.umd.edu. 2017. *"GEOL342 - Sedimentation And Stratigraphy"* [Online]. Available: https://www.geol.umd.edu/~jmerck/geol342/lectures/04.html [Accessed 31 Jan. 2017.

Germano, M., Piomelli, U., Moin, P. & Cabot, W. H. 1991. A dynamic subgrid-scale eddy viscosity model. *Physics of Fluids A: Fluid Dynamics (1989-1993),* 3**,** 1760-1765.

Graf, W. & Istiarto, I. 2002. Flow pattern in the scour hole around a cylinder. *Journal of Hydraulic Research,* 40**,** 13-20.

Guemou, B., Seddini, A. & Ghenim, A. N. 2016. Numerical investigations of the round-nosed bridge pier length effects on the bed shear stress. *Progress in Computational Fluid Dynamics, An International Journal,* 16**,** 313-321.

Hafez, Y. I. 2016. Mathematical Modeling of Local Scour at Slender and Wide Bridge Piers. *Journal of Fluids,* 2016**,** 19.

Hickin, E. J. 1995. *River Geomorphology*, Wiley.

Hinze, J. 1975. Turbulence McGraw-Hill. *New York,* 218.

Huang, W., Yang, Q. & Xiao, H. 2009. CFD modeling of scale effects on turbulence flow and scour around bridge piers. *Computers & Fluids,* 38**,** 1050-1058.

Hunt, B. E. 2009. *Monitoring scour critical bridges*, Transportation Research Board.

Jørgensen, N. G. & Nilsson, H. 2012. Implementation of a turbulent inflow boundary condition for LES based on a vortex method. *A course at Chalmers University of Technology*.

Kardan, N., Hassanzadeh, Y. & Hakimzadeh, H. 2012. Comparison of dynamic bed shear stress distribution around a bridge pier using various turbulence models. *ICSE6. Paris*.

Keshavarzi, A., Melville, B. & Ball, J. 2014. Three-dimensional analysis of coherent turbulent flow structure around a single circular bridge pier. *Environmental Fluid Mechanics,* 14**,** 821-847.

Khosronejad, A., Kang, S. & Sotiropoulos, F. 2012. Experimental and computational investigation of local scour around bridge piers. *Advances in Water Resources,* 37**,** 73-85.

Kim, H. S., Nabi, M., Kimura, I. & Shimizu, Y. 2014. Numerical investigation of local scour at two adjacent cylinders. *Advances in Water Resources,* 70**,** 131-147.

Kirkil, G. 2007. *Numerical investigation of flow and sediment transport processes at cylindrical bridge piers at different stages of the scour process.* Ph.D Thesis, The University of Iowa.

Kirkil, G. & Constantinescu, G. 2009. Nature of flow and turbulence structure around an in-stream vertical plate in a shallow channel and the implications for sediment erosion. *Water Resources Research,* 45.

Kirkil, G. & Constantinescu, G. 2010. Flow and turbulence structure around an in-stream rectangular cylinder with scour hole. *Water Resources Research,* 46.

Kirkil, G., Constantinescu, G. & Ettema, R. The horseshoe vortex system around a circular bridge pier on equilibrium scoured bed. World Water and Environmental Resources Congress, Alaska, 2005.

Kirkil, G., Constantinescu, G. & Ettema, R. 2009. Detached eddy simulation investigation of turbulence at a circular pier with scour hole. *Journal of Hydraulic Engineering,* 135**,** 888-901.

Kirkil, G., Constantinescu, S. & Ettema, R. 2008. Coherent structures in the flow field around a circular cylinder with scour hole. *Journal of Hydraulic Engineering,* 134**,** 572-587.

Laursen, E. M. & Toch, A. 1956. *Scour around bridge piers and abutments*, Iowa Highway Research Board Ames, IA, USA.

Lilly, D. K. 1992. A proposed modification of the Germano subgrid-scale closure method. *Physics of Fluids A: Fluid Dynamics,* 4**,** 633-635.

Link, O., Gobert, C., Manhart, M. & Zanke, U. Effect of the horseshoe vortex system on the geometry of a developing scour hole at a cylinder. 4th International Conference on Scour and Erosion, Tokyo, 2008. 162-168.

Mathey, F., Cokljat, D., Bertoglio, J. P. & Sergent, E. 2006. Assessment of the vortex method for large eddy simulation inlet conditions. *Progress in Computational Fluid Dynamics, An International Journal,* 6**,** 58-67.

Melville, B., Ettema, R. & Jain, S. Measurement of bridge scour. Proceedings of the Bridge Scour Symposium, 1989. 183-194.

Melville, B. W. 1997. Pier and abutment scour: integrated approach. *Journal of Hydraulic Engineering,* 123**,** 125-136.

Melville, B. W. & Chiew, Y.-M. 1999. Time scale for local scour at bridge piers. *Journal of Hydraulic Engineering,* 125**,** 59-65.

Melville, B. W. & Raudkivi, A. J. 1977. Flow characteristics in local scour at bridge piers. *Journal of Hydraulic Research,* 15**,** 373-380.

Menter, F. 2012. Best practice: scale-resolving simulations in ANSYS CFD. *ANSYS Germany GmbH***,** 1-70.

Meyer-Peter, E. & Müller, R. Formulas for bed-load transport. 1948. IAHR.

Mostafa, E., Yassin, A., Ettema, R. & Melville, B. Local Scour at Skewed Bridge Piers. Hydraulic Engineering:, 1993. ASCE, 1037-1042.

Nieto, F., Hargreaves, D., Owen, J. S. & Hernández, S. 2015. On the applicability of 2D URANS and SST k-ω turbulence model to the fluid-structure interaction of rectangular cylinders. *Engineering Applications of Computational Fluid Mechanics,* 9**,** 157-173.

Olsen, N. R. & Kjellesvig, H. M. 1998. Three-dimensional numerical flow modeling for estimation of maximum local scour depth. *Journal of Hydraulic Research,* 36**,** 579-590.

Olsen, N. R. & Melaaen, M. C. 1993. Three-dimensional calculation of scour around cylinders. *Journal of Hydraulic Engineering,* 119**,** 1048-1054.

Paice, C. & Hey, R. The control and monitoring of local scour at bridge piers. Hydraulic Engineering:, 1993. ASCE, 1061-1066.

Paik, J., Escauriaza, C. & Sotiropoulos, F. 2007. On the bimodal dynamics of the turbulent horseshoe vortex system in a wing-body junction. *Physics of Fluids (1994-present),* 19**,** 045107.

Paik, J., Ge, L. & Sotiropoulos, F. 2004. Toward the simulation of complex 3D shear flows using unsteady statistical turbulence models. *International Journal of Heat and Fluid Flow,* 25**,** 513-527.

Palau-Salvador, G., Stoesser, T. & Rodi, W. 2008. LES of the flow around two cylinders in tandem. *Journal of Fluids and Structures,* 24**,** 1304-1312.

Parker, G. 1990. Surface-based bedload transport relation for gravel rivers. *Journal of hydraulic research,* 28**,** 417-436.

Pasiok, R. & Stilger-Szydło, E. 2010. Sediment particles and turbulent flow simulation around bridge piers. *Archives of Civil and Mechanical Engineering,* 10**,** 67-79.

Patel, Y. 2010. *Numerical investigation of flow past a circular cylinder and in a staggered tube bundle using various turbulence models.* LAPPEENRANTA UNIVERSITY OF TECHNOLOGY.

Ramos, P., Maia, R., Schindfessel, L., De Mulder, T. & Pêgo, J. 2016. Large Eddy Simulation of the water flow around a cylindrical pier mounted in a flat and fixed bed.

Richardson, E. & Davis, S. 2001. Evaluating scour at bridges: Federal Highway Administration Hydraulic Engineering Circular No. 18. *Publication FHWA NHI***,** 01-001.

Richardson, J. E. & Panchang, V. G. 1998. Three-dimensional simulation of scour-inducing flow at bridge piers. *Journal of Hydraulic Engineering,* 124**,** 530-540.

Rodi, W., Constantinescu, G. & Stoesser, T. 2013. *Large-eddy simulation in hydraulics*, Crc Press.

Roulund, A., Sumer, B. M., Fredsøe, J. & Michelsen, J. 2005. Numerical and experimental investigation of flow and scour around a circular pile. *Journal of Fluid Mechanics,* 534**,** 351-401.

Salaheldin, T. M., Imran, J. & Chaudhry, M. H. 2004. Numerical modeling of three-dimensional flow field around circular piers. *Journal of Hydraulic Engineering,* 130**,** 91-100.

Sarker, M. A. 1998. Flow measurement around scoured bridge piers using Acoustic-Doppler Velocimeter (ADV). *Flow Measurement and Instrumentation,* 9**,** 217-227.

Shao, W.-y., Zhang, Y.-p., Zhu, D. Z. & Zhang, T.-q. 2013. Drag force on a free surface-piercing yawed circular cylinder in steady flow. *Journal of Fluids and Structures,* 43**,** 145-163.

Shen, H. W., Schneider, V. R. & Karaki, S. 1969. Local scour around bridge piers. *Journal of the Hydraulics Division*.

Sheppard, D. M., Odeh, M. & Glasser, T. 2004. Large scale clear-water local pier scour experiments. *Journal of Hydraulic Engineering,* 130**,** 957-963.

Shields, A. 1936. Anwendung der Aehnlichkeitsmechanik und der Turbulenzforschung auf die Geschiebebewegung. Preussischen Versuchsanstalt für Wasserbau.

Simões, F. J. 2014. Shear velocity criterion for incipient motion of sediment. *Water Science and Engineering,* 7**,** 183-193.

Smagorinsky, J. 1963. General circulation experiments with the primitive equations: I. The basic experiment. *Monthly Weather Review,* 91**,** 99-164.

Swenson, D. V. & Ingraffea, A. R. 1991. The collapse of the Schoharie Creek Bridge: a case study in concrete fracture mechanics. *International Journal of Fracture,* 51**,** 73-92.

Tao, J. 2013. *Fusion of numerical modeling and innovative sensing to advance bridge scour research and practice.* Case Western Reserve University.

Tao, J. & Yu, X. B. Flow and scour patterns around bridge piers with different configurations: insights from CFD simulations. Geo-Congress 2014 Technical Papers@ sGeo-characterization and Modeling for Sustainability, 2014. ASCE, 2655-2664.

Tison, L. Erosion autour de piles de ponts en riviere. Annales des Travaux publics de Belgique, 1940. 813-817.

Tseng, M. H., Yen, C. L. & Song, C. 2000. Computation of three-dimensional flow around square and circular piers. *International Journal for Numerical Methods in Fluids,* 34**,** 207-227.

Unger, J. & Hager, W. H. 2007. Down-flow and horseshoe vortex characteristics of sediment embedded bridge piers. *Experiments in Fluids,* 42**,** 1-19.

Van Rijn, L. C. 1984. Sediment transport, part I: bed load transport. *Journal of Hydraulic Engineering,* 110**,** 1431-1456.

Van Rijn, L. C. 1986. Applications of sediment pick-up function. *Journal of Hydraulic Engineering,* 112**,** 867-874.

Van Rijn, L. C. 2016. Initiation of motion and suspension; critical bed-shear stress for sand-mud mixtures. *Journal of Hydraulic Engineering*.

Versteeg, H. K. & Malalasekera, W. 2007. *An introduction to computational fluid dynamics: the finite volume method*, Pearson Education.

Wang, J. 2004. *The SRICOS-EFA method for complex pier and contraction scour.* Texas A&M University.

Wei, Z. & Huhe, A. 2006. Large-eddy simulation of three-dimensional turbulent flow around a circular pier. *Journal of Hydrodynamics, Ser. B,* 18**,** 765-772.

Werner, H. & Wengle, H. 1993. Large-eddy simulation of turbulent flow over and around a cube in a plate channel. *Turbulent Shear Flows 8.* Springer.

Wilcock, P. R. & Crowe, J. C. 2003. Surface-based transport model for mixed-size sediment. *Journal of Hydraulic Engineering,* 129**,** 120-128.

Wilcox, D. 2006. Turbulence Modeling for CFD, La Canada, CA, USA: DCW Industries. Inc.

Xiong, W., Cai, C., Kong, B. & Kong, X. 2014. CFD Simulations and analyses for bridge-scour development using a dynamic-mesh updating technique. *Journal of Computing in Civil Engineering,* 30**,** 04014121.

Xiong, W., Tang, P., Kong, B. & Cai, C. 2016. Reliable bridge scour simulation using Eulerian two-phase flow theory. *Journal of Computing in Civil Engineering,* 30**,** 04016009.

Yanmaz, A. M. & Altinbilek, H. D. g. a. 1991. Study of time-depenbent local scour around bridge piers. *Journal of Hydraulic Engineering,* 117**,** 1247-1268.

Younis, B. & Abrishamchi, A. 2014. Three-dimensional turbulent vortex shedding from a surface-mounted square cylinder: Predictions with large-eddy simulations and URANS. *Journal of Fluids Engineering,* 136**,** 060907.

Zhao, M., Cheng, L. & Zang, Z. 2010. Experimental and numerical investigation of local scour around a submerged vertical circular cylinder in steady currents. *Coastal Engineering,* 57**,** 709-721.

Appendix A

UDF Codes Used in This Study

A.1 Overview

A user-defined function, UDF, is a function allows the user to enhance additional features by embedded the written code with the Fluent solver. UDFs are written in C^{++}. In this study, the UDF permits the mesh cells to move dynamically depending on the wall shear stress strategy, by compute and use wall shear stresses. The UDF loops over all the faces of the wall boundary on which the wall shear stress has to be obtained. The wall shear stress is stored inside a user defined memory UDM at the cell next to the wall. The storage wall shear stress compared with the critical shear stress at each time step. If the wall shears stress greater than the critical shear stress the mesh will be move depending on the sediment transport equation suggested by Van Rijn (1986). In this appendix, a brief description of the macros and commands which are required to write UDF for moving mesh depending on the wall shear stress. Every UDF contains the udf.h file inclusion directive (#include "udf.h") at the beginning of the source code file, which allows definitions for DEFINE macros and other Fluent-provided macros and functions to be included during the compilation process.

A.2 Defining UDF Using DEFINE Macros

UDFs are defined using Fluent-supplied function statements. These function statements are implemented in the code as macros, and are referred to in this document as DEFINE macros. Definitions for DEFINE macros are contained in the udf.h header file. In this study, the following two DEFINE macros are used to write the UDF, the first one is **DEFINE_EXECUTE_AT_END (name),** this macros can be used to calculate the wall shear stress at the end of a time step and save the date in the user defined memory, and the second is **DEFINE_GRID_MOTION (name, dt, time, dtime),** that be used to define the dynamic mesh in the domain. Header file (#include "dynamesh_tools.h”) should be included in order to access this DFINE macros. Instead of **name** in both macros should be replacement for a proper name related to what the UDF dealing with. In this study the **name** changed to shear_stress, and moving_bed for the first and second DEFINE macros respectively.

A.3 Data Types in Fluent

In addition to standard C language data types such as real, int, etc. that can be used to define data in the UDF programme, there are Fluent-specific data types that are associated with solver data. These data types represent the computational units for a grid as shown in Figure A.1

Variables that are defined using these data types are typically supplied as arguments to DEFINE macros as well as to other special functions that access Fluent solver data. Some of the more commonly-used Fluent data types are:

cell t is the data type for a cell ID. It is an integer index that identifies a particular cell within a given thread.

face t is the data type for a face ID. It is an integer index that identifies a particular face within a given thread.

The **Thread** data type is a structure that acts as a container for data that is common to the group of cells or faces that it represents.

The **Node** data type is a structure that acts as a container for data associated with the corner of a cell or face.

The **Domain** data type is a structure that acts as a container for data associated with a collection of node, face, and cell threads in a mesh.

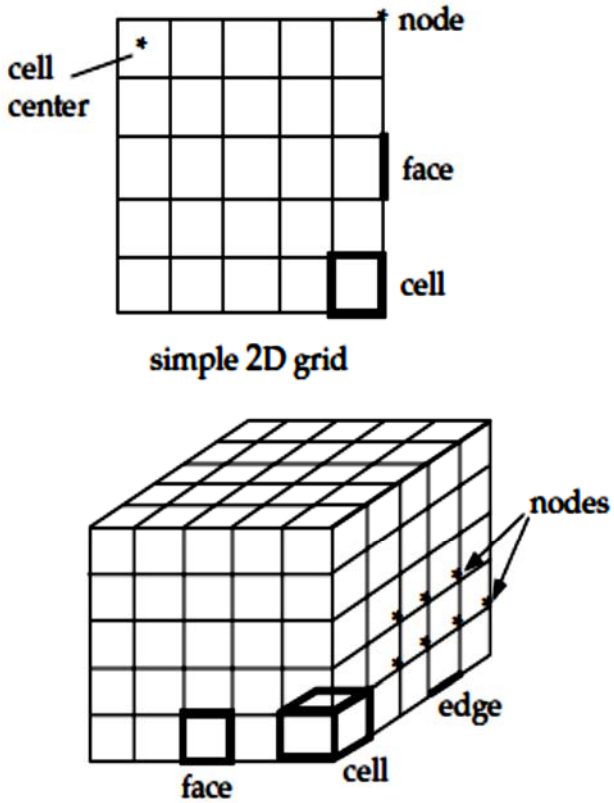

Figure A. 1: Grid components (Fluent, 2009)

A.4 Parallelizing the serial UDF

Fluent's serial solver contains Cortex and only a single Fluent process. The parallel solver, on the other hand, contains three types of executable: Cortex, host, and compute node. When Fluent runs in parallel, an instance of Cortex starts, followed by one host and n compute nodes, thereby giving a total of n+2 running processes. By adding special macros for the parallel solver, direct the compiler to include only portions of the function that apply to a particular process, and ignore the rest. Below some macros which are used to run Fluent in parallel solver:

#if !RP_HOST: Code written inside this will be performed ONLY by serial or node.

#if RP_NODE: Code written inside this will be performed ONLY by node process.

#if PARALLEL: Only if the Fluent is opened in PARALLEL mode.

if PRINCIPAL_FACE_P(f,tf), face is on the principal compute node, this macros used when a partition boundary face will get counted twice in a face loop.

if (I_AM_NODE_ZERO_P): Performing the file open to write operation ONLY on the FIRST node process to AVOID multiple file writing operations on each of the nodes

PRF GRSUM1(x): Computes the global sum of a real variable x across all compute nodes.

A.5 Compiled UDFs

The compilation process for compiled UDFs consists of two steps: build and load. The process involves accessing to the compiled UDFs panel to build a shared library from one or more source files, and then loading the shared library (e.g., libudf) into Fluent. Once a shared library is loaded, it can be written with any case file so that it will be automatically loaded whenever that case file is subsequently read. This saves having to reload the compiled library every time you want to run a simulation. Once loaded, all of the compiled UDFs that are contained within the shared library will become visible and selectable in graphical user interface panel(s) in Fluent.

A.6 User-Defined Memory Storage

This function can be used to store values computed by applied UDF in memory so that they can be retrieved later, either by a UDF or for post processing within Fluent. Specify the Number of User-Defined Memory Locations are needed in the User-Defined Memory panel. The macro C UDMI can be used in this UDF to access a particular user-defined memory location in a cell. Field values that have been stored in user-defined memory will be saved to the data file. These fields will appear in the User Defined Memory category in the drop-down lists in Fluent's post-processing panels. They will be named udm-0, udm-1, etc., based on the memory location index. The total number of memory locations is limited to 500. In this study just one UDM is needed.

A.7 Hooking Dynamic Mesh UDFs to Fluent

The hook function is the next step comes after the UDF have been compiled to Fluent using a graphical user interface panel. For this particular UDF, there is two types of hooks have been applied.

A.7.1 Hooking an Execute-at-End UDF to Fluent

After the UDF that have defined using DEFINE EXECUTE AT END is compiled, the Edit icon that correspond to the Execute at End will become active, and the name that had specified in the DEFINE macro argument will become visible in the User-Defined Function Hooks panel in Fluent.

A.7.2 Hooking a DEFINE GRID MOTION to Fluent

After the UDF that have defined using DEFINE GRID MOTION is compiled, the name that had specified in the DEFINE macro argument will become visible in the Dynamic Mesh Zones panel in Fluent.

A.8 The UDF codes

A.8.1 Moving mesh in the bottom wall

This UDF is imbedded to the Fluent software to find the accumulative vertical movement of the grid cells in the bottom wall after a certain time of period, and depending on the bed shear stress that computed using LES.

The first part of this UDF shows a strategy to compute and use wall shear stresses. It loops over all the faces of the wall boundary on which the wall shear stress has to be obtained. The wall shear stress is stored inside a UDM at the cell next to the wall.

```
#include "udf.h"
#include "dynamesh_tools.h"
#if RP_NODE
DEFINE_EXECUTE_AT_END(shear_stress)
{
 Domain *d;
 real shear; /*shear=τb */
 face_t f;
 real wallshear[ND_ND];
 real A[ND_ND];
 cell_t c, c0;
 Thread *t,*t0, *c_thread;
 int Zone_ID=13; /* Zone ID of the wall on which shear stress has to be calculated */
 /* It can be obtained from the boundary condition panel.*/
 d=Get_Domain(1);
 /* Initialize the UDM value to zero in complete domain */
 thread_loop_c(c_thread,d)
 {
 begin_c_loop(c, c_thread)
 {
 C_UDMI(c,c_thread,0)= 0;
 }
 end_c_loop(c, c_thread)
 }
 /* Calculate wall shear stress and store them in UDM */
 t=Lookup_Thread(d,Zone_ID);
 begin_f_loop(f,t)
if PRINCIPAL_FACE_P(f,t)
 {
 F_AREA(A,f,t);
shear=NV_MAG(F_STORAGE_R_N3V(f,t,SV_WALL_SHEAR)/NV_MAG(A);
```

```
 c0 = F_C0(f,t);
 t0 = THREAD_T0(t);
 C_UDMI(c0,t0,0)= shear;
 }
 end_f_loop(f,t)
#endif
}
```

The second part of this UDF shows a strategy to compute the scour depth around the bridge pier depending on the wall shear stress stored in the UDM.

DEFINE_GRID_MOTION (moving_bed,domain,dt,time,dtime):

```
{
#if RP_NODE
Thread *t = DT_THREAD(dt);
face_t f;
cell_t c0;
Thread *t0;
Node *v;
real vel, shear, g, d, T_cr, ds, tc, p, u,ps, e, nn, os;
/* vel=dh/dt, d=d50, T_cr=T, ds=D*, tc=τb.cr, p=ρ, u=ϑ, ps=ρs, e=Δ,
nn=n */
real NV_VEC(dz);
int n;
g= 9.81;
d=0.00036;
tc = 0.2;
p = 998.2;
u = 0.00000103;
ps=2650;
nn=0.4;
e=(ps -p)/p;
ds =d*pow(((e*g)/(u*u)),1/3);
```

```
/* Set/activate the deforming flag on adjacent cell zone,
which means that the cells adjacent to the deforming wall
will also deformed, in order to avoid skewness.*/

SET_DEFORMING_THREAD_FLAG(THREAD_T0(t));


/* Loop over the deforming boundary zone's faces; inner
loop loops over all nodes of a given face; Thus, since one
node can belong to several faces, one must guard against
operating on a given node more than once:*/

NV_S(dz,=,0);

begin_f_loop(f,t)

if PRINCIPAL_FACE_P(f,t)

{

f_node_loop(f,t,n)

{

v = F_NODE(f,t,n);


/* Update the current node only if it has not been
previously visited:*/
if  (NODE_POS_NEED_UPDATE(v))


/* Set flag to indicate that the current node's position
has been updated, so that it will not be updated during a
future pass through the loop*/
NODE_POS_UPDATED (v);

c0=F_C0(f,t);

t0=THREAD_T0(t);

shear = C_UDMI(c0,t0,0);

if (shear > tc)

{

T_cr = ((shear/tc)-1);

vel=((0.00033*pow(e*g*d,0.5)*pow(ds,0.3))/(1-nn))*(pow

(T_cr,1.5);

dz[1]=vel;

NV_S(dz,*=,dtime);

NV_V(NODE_COORD(v), -=,dz);
```

```
}
}
}
end_f_loop(f,tf);
#endif
}
```

A.8.2 Compute the time- averaged variables

This UDF is used to find the time averaged variables such as mean velocities and mean turbulent kinetic energy for a specific point in the domain from LES simulation, and as shown below:

```
#include "udf.h"
DEFINE_EXECUTE_AT_END(calc_means)
{
int Zone_ID = 15;
#if !RP_HOST
cell_t c;
Thread *t;
int counter;
real x[ND_ND];
real u_mean, v_mean, w_mean, k_mean, u, v, w, u_dash,
v_dash, w_dash, k_dash, k_total;
Domain *d = Get_Domain(1);
FILE *pf;
#if PARALLEL
if (I_AM_NODE_ZERO_P)
#endif
if(NULL == (pf = fopen("Ux.txt","a")))
{
Error("Could not open file!\n");
}
u = 0.25; v = 0.0; w = 0.0;
```

```
u_mean = 0.0; v_mean = 0.0; w_mean = 0.0; k_mean = 0.0;
u_dash = 0.0; v_dash = 0.0; w_dash = 0.0; k_dash = 0.0;
k_total = 0.0;
counter = 0;
thread_loop_c(t,d)
{
Thread *t = Lookup_Thread(d, Zone_ID);
begin_c_loop(c,t)
{
/*
C_CENTROID(x,c,t);
*/
u_mean = u_mean + C_U(c,t);
v_mean = v_mean + C_V(c,t);
w_mean = w_mean + C_W(c,t);
counter++;
}
end_c_loop(c,t)
}
u_mean = u_mean / (real)counter;
v_mean = v_mean / (real)counter;
w_mean = w_mean / (real)counter;
k_mean=0.5*((u_mean*u_mean)+(v_mean*v_mean)+(w_mean*w_mean
));
#if RP_NODE /* code written inside this will be performed
ONLY by NODE process */
u_mean = PRF_GRSUM1(u_mean);
v_mean = PRF_GRSUM1(v_mean);
w_mean = PRF_GRSUM1(w_mean);
k_mean = PRF_GRSUM1(k_mean);
#endif /* RP_NODE */
u_mean = u_mean/C_NNODES(c,t);
v_mean = v_mean/C_NNODES(c,t);
w_mean = w_mean/C_NNODES(c,t);
```

```
k_mean =  k_mean/C_NNODES(c,t);
u_dash = u_dash + (u - u_mean);
v_dash = v_dash + (v - v_mean);
w_dash = w_dash + (w - w_mean);
k_dash=0.5*((u_dash*u_dash)+(v_dash*v_dash)+(w_dash*w_dash
));
k_total = k_mean + k_dash ;
#if PARALLEL
if (I_AM_NODE_ZERO_P)
#endif
fprintf(pf,"%e\t%e\t%e\t%e\t%e\t%e\t%e\n",CURRENT_TIME,
u_mean, v_mean, w_mean, k_dash, k_total, (real)counter);
#if PARALLEL
if (I_AM_NODE_ZERO_P)
#endif
fclose(pf);
}
#endif /* !RP_HOST */
```